Quarterly Reviews of Biophysics **35**, 3 (2002), pp. 205–286. © 2002 Cambridge University Press
DOI: 10.1017/S0033583502003785 Printed in the United Kingdom

Understanding protein folding with energy landscape theory
Part II: Quantitative aspects

Steven S. Plotkin[1,*] and José N. Onuchic[2,*]

[1] Department of Physics and Astronomy, University of British Columbia, Vancouver, Canada V6T 1Z1
[2] Department of Physics, University of California at San Diego, La Jolla 92093, USA

* Correspondence may be addressed to either author.
S. Plotkin: Tel.: 604-822-8813; Fax: 604-822-5324; E-mail: steve@physics.ubc.ca
J. Onuchic: Tel.: 858-534-7067; Fax: 858-822-4560; E-mail: jonuchic@ucsd.edu

1. Introduction

We have seen in Part I of this review that the energy landscape theory of protein folding is a statistical description of a protein's complex potential energy surface, where individual folding events are sampled from an ensemble of possible routes on the landscape. We found that the most likely global structure for the landscape of a protein can be described as that of a partially random heteropolymer with a rugged, yet funneled landscape towards the native structure. Here we develop some quantitative aspects of folding using tools from the statistical mechanics of disordered systems, polymers, and phase transitions in finite-sized systems. Throughout the text we will refer to concepts and equations developed in Part I of the review, and the reader is advised to at least survey its contents before proceeding here. Sections, figures or equations from Part I are often prefixed with I- [e.g. Section I-1.1, Fig. I-1, Eq. (I-1.1)].

2. Quantifying the notions behind the energy landscape

In this section we will go more deeply into the physical concepts behind energy landscape theory. This will allow for a quantitative description of protein folding thermodynamics and kinetics, as well as the glass transition in random heteropolymers.

2.1 Basic concepts of the Random Energy Model (REM)

As temperature is lowered, a random heteropolymer (RHP) exhibits a phase transition to a state of zero configurational entropy, characterized by the freezing of the system into one of many globally distinct, low energy configurations. A basic analysis of this can be seen by applying the random energy model (REM) (Derrida, 1981; Gross and Mézard, 1984) to configurations of the RHP (Shakhnovich & Gutin, 1989a). Inspection of the RHP Hamiltonian [cf. Eq. (6.1) of Part I]

$$\mathscr{H}_{\mathrm{RHP}}(\{s_i\}, \{r_i\}) = \sum_{i<j} \epsilon(s_i, s_j)\Delta(r_i - r_j), \tag{2.1}$$

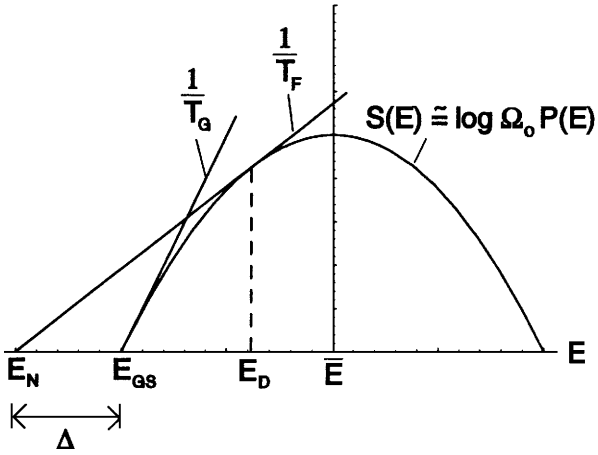

Fig. 1. Log density of states in the REM. The slope of the curve at the ground state energy (E_{GS}) gives the reciprocal of the freezing or 'glass' temperature (T_G) in the model. For designed or protein-like sequences there is a minimally frustrated native state (E_N) with considerably lower energy (Δ) than the putative RHP ground state. This state will be in thermodynamic equilibrium having equal Boltzmann weight as a manifold of unfolded states with higher average energy (E_D) at a temperature (T_F) above the REM glass temperature (T_G). (Figure adapted from Shakhnovich & Gutin, 1993.)

shows that the energy E of a state at fixed density is the sum of a large number of random terms. Thus by the central limit theorem the energies of the configurations are distributed according to a Gaussian distribution

$$P(E) = \frac{1}{(2\pi\Delta^2)^{\frac{1}{2}}} \mathrm{e}^{-(E-\bar{E})^2/2\Delta^2}, \tag{2.2}$$

where $\bar{E} = N\chi\bar{\epsilon}$ is the average energy and $\Delta^2 = \chi N b^2$ is the variance; here N is the polymer length, χ is the mean number of contacts per monomer, and b^2 is the energetic variance of the individual contacts.

Thus the average number of states in the interval $(E, E+\mathrm{d}E)$, $\bar{n}(E)\mathrm{d}E$, is given by (see Fig. 1)

$$\bar{n}(E)dE = \Omega_0 P(E)\mathrm{d}E = \exp\left(Ns_0 - \frac{(E-\bar{E})^2}{2\chi N b^2} \right) dE, \tag{2.3}$$

where $\Omega_0 = \exp(Ns_0)$ is the total number of polymer conformations at fixed contact density. Then from Eq. (2.3) (see also Fig. 1), it is clear that there exists a critical energy

$$E_{GS} = N(\chi\bar{\epsilon} - b\sqrt{2\chi s_0}) \tag{2.4}$$

such that if $E > E_{GS}$ the average number $\bar{n}(E)$ of levels is $\gg 1$, and if $E < E_{GS}$, $\bar{n}(E) \ll 1$. Because of the statistical independence of energy levels in the REM, the relative fluctuations of $n(E)$ around the mean die away as $\bar{n}(E)^{-\frac{1}{2}}$, and therefore $n(E) \cong \bar{n}(E)$ when $E > E_{GS}$. If on the other hand $E < E_{GS}$, $\bar{n}(E) \ll 1$, so for almost all sequences $n(E) = 0$ and with a very small probability which vanishes exponentially with N, $n(E) \geqslant 1$. Thus in the thermodynamic

limit, if $E > E_{GS}$ the microcanonical entropy $S(E)$ is a parabolic function, similar to the density of states of a finite-sized paramagnet or finite, random-field Ising model:

$$S(E) = \log \bar{n}(E) = Ns_0 - \frac{(E-\bar{E})^2}{2zNb^2}. \tag{2.5}$$

The REM is applicable to the freezing of a RHP to the extent that the states contributing to the thermodynamics are uncorrelated in energy. This approximation is a reasonably good one. If we were to randomly pick pairs of states from the pool of all possible configurations, most pairs of states would have little or no structural similarity, because the topological constraints consistent with a given degree of similarity dramatically reduce the number of pairs with structural overlap. Issues of polymer entropy and REM applicability are treated further in Section 2.4.

Through the definition of temperature, $1/T = \partial S/\partial E$, thermodynamic properties such as the energy, entropy, and free energy may be obtained at temperature T:

$$\frac{E(T)}{N} = z\bar{\epsilon} - \frac{zb^2}{T} \tag{2.6a}$$

$$\frac{S(T)}{N} = s_0 - \frac{zb^2}{2T^2} \tag{2.6b}$$

$$\frac{F(T)}{N} = \frac{E-TS}{N} = z\bar{\epsilon} - Ts_0 - \frac{zb^2}{2T}. \tag{2.6c}$$

Equations (2.6*a*), (2.6*b*) and (2.6*c*) are valid so long as the temperature is high enough that a macroscopic number of states are occupied, i.e. T is above T_G where $S(T_G) = 0$. From Eq. (2.6*b*), the chain conformational entropy vanishes above absolute zero at a temperature

$$T_G = b\sqrt{\frac{z}{2s_0}}. \tag{2.7}$$

At and below this temperature, the system will be frozen into one of a small number of low-energy states, whose number is sufficiently small that their entropy is insignificant. Thus below this point the entropy vanishes and remains equal to zero. The thermodynamics are then given by:

$$\frac{E(T \leqslant T_G)}{N} = \frac{E_{GS}}{N} = z\bar{\epsilon} - b\sqrt{2zs_0} \tag{2.8a}$$

$$S(T \leqslant T_G) = 0 \tag{2.8b}$$

$$F(T \leqslant T_G) = E - TS = E_{GS}. \tag{2.8c}$$

The entropy in Eqs. (2.6*b*) and (2.8*b*) vanishes continuously as $T \to T_G$, i.e. the transition is second order.

The random energy model was first used to describe the unfolded parts of a protein in Bryngelson & Wolynes (1987), and shown to be a good approximation by the replica method in Shakhnovich & Gutin (1989b). Issues related to the glass transition are treated further in the next section and Section 3.1.

2.2 Replica-symmetric partition functions and densities of states

As described in Part I.5 minimal frustration greatly simplifies the folding problem, and allows for an analysis of folding mechanism, structure prediction, and sequence design that is not critically sensitive to the microscopic details of the amino-acid sequence along the chain, but rather on gross, overall features of ensembles of sequences which fold to the same structure. Minimal frustration and the resulting funneled landscape justifies using a replica-symmetric partition function in the canonical ensemble, or a sequence averaged density of states in the microcanonical ensemble, to describe the folding mechanism of a typical sequence folding to a given structure. Physically, replica-symmetric behavior corresponds to all copies of the system following the same behavior, in this case reliably folding to the same structure, as opposed to being trapped in many globally distinct structures.

Formally, the sequence-averaged free energy $\langle F \rangle$ is calculated within the canonical ensemble using the replica identity:

$$\langle F \rangle = -T\langle \ln Z \rangle = -T \lim_{n \to 0} \frac{\langle Z^n \rangle - 1}{n}. \tag{2.9}$$

For two replicas,

$$\langle Z^2 \rangle = \sum_{\alpha=1}^{\nu^N} \sum_{\beta=1}^{\nu^N} \langle e^{-(E_\alpha + E_\beta)/T} \rangle, \tag{2.10}$$

where ν^N is the total number of configurational states in the system. Two configurations α and β are correlated energetically depending on how similar they are, similarity being defined in the context of the Hamiltonian [Eq. (2.1)] (as well as the protein Hamiltonian [Eq. (6.3) of Part I]) as the fraction of shared pair contact interactions:

$$q_{\alpha\beta} = \frac{1}{M} \sum_{i<j} \Delta(r_i^\alpha - r_j^\alpha)\Delta(r_i^\beta - r_j^\beta). \tag{2.11}$$

Then $\langle \exp -(E_\alpha + E_\beta)/T \rangle$ depends only on the overlap between configurations α and β and $\langle Z^2 \rangle$ can be written

$$\langle Z^2 \rangle = \sum_{\alpha=1}^{\nu^N} \sum_{\beta=1}^{\nu^N} -e^{N\epsilon(q_{\alpha\beta})/T}. \tag{2.12}$$

Because the expectation value of the energies of two states depends only on their overlap, to calculate the trace for large N it is sufficient to know the number of configurations having overlap $q_{\alpha\beta}$, $e^{Ns(q_{\alpha\beta})}$. Then for large N, the saddle-point overlap $q^*_{\alpha\beta}$ gives the behavior of $\langle Z^2 \rangle$, and

$$\ln \langle Z^2 \rangle = N \max_{q_{\alpha\beta}} \left(\frac{-\epsilon(q_{\alpha\beta})}{T} + s(q_{\alpha\beta}) \right). \tag{2.13}$$

For n replicas the saddle point is obtained in the space of $n(n-1)/2$ variables.

It has been shown that above the replica symmetry breaking transition, the saddle-point solution which yields the free energy is that in which all replica overlaps $q_{\alpha\beta}$ equal one value q (Sherrington & Kirkpatrick, 1975; de Almeida & Thouless, 1978). Then the free energy can be obtained as a function of q. The analysis outlined above may be straightforwardly generalized to account for variable polymer density.

The thermodynamics in the microcanonical ensemble is considerably simpler. Here one seeks the sequence-averaged log density of states $\langle S(E)\rangle = \langle \ln n(E)\rangle$, which as before depends on the overlap q to a reference state. The replica identity may be used again

$$\langle S(q, E)\rangle = \lim_{p\to 0} \frac{\langle n(q, E)^p\rangle - 1}{p}. \tag{2.14}$$

For *all* moments p, there are two regimes for $n(q, E)$ (Derrida, 1981),

$$\langle n(q, E)^p\rangle \approx \langle n(q, E)\rangle^p \quad E > E_{\rm GS}(q) \tag{2.15a}$$

$$\langle n(q, E)^p\rangle \approx \langle n(q, E)\rangle \quad E < E_{\rm GS}(q), \tag{2.15b}$$

where $E_{\rm GS}(q) = -Nb\sqrt{2s(q)}$ is where $\langle n(q, E)\rangle = 1$ and the entropy typically vanishes.

Under typical folding conditions, a protein reconfigures within a band of energies in the region of large density of states, $E(q) > E_{\rm GS}(q)$ (until $q \approx 1$), so

$$\langle S(q, E)\rangle = \ln\langle n(q, E)\rangle, \tag{2.16}$$

which is the approximation used in Eq. (2.5) in obtaining the high-temperature REM thermodynamics.

2.3 The RHP phase diagram and avoided phase transitions

Even though there may be as few as one energy scale (b) in a RHP (with zero mean attraction between residues), there are several phase transitions in the system. For example, random interactions can induce collapse in a heteropolymer, at a temperature $T_{\rm C}$ distinct from the glass temperature $T_{\rm G}$, depending on the stiffness of the chain.

Collapse occurs below a temperature $T_{\rm C}$, defined as the temperature where the free energy of the coil and collapsed phases of the heteropolymer are equal:

$$F(\chi \simeq 0, T_{\rm C}) = F(\chi \simeq \chi_c, T_{\rm C}). \tag{2.17}$$

From Eq. (2.6*c*) this occurs when

$$-T_{\rm C}s_0 = -T_{\rm C}s_{\rm C} - \frac{\chi_c b^2}{2T_C} - \chi_c\bar{\epsilon} \tag{2.18}$$

where s_0 is the entropy in the coil state (where the number of contacts per residue $\chi \simeq 0$) and $s_{\rm C}$ is the entropy in the collapsed state (where $\chi \simeq 1$). Using the reduction in entropy for collapsed *versus* coil chain statistics from Eq. (4.1) of Part I:

$$s_0 - s_{\rm C} = s(\eta = 0) - s(\eta = 1) = \ln\nu - \ln\frac{\nu}{\rm e} = 1, \tag{2.19}$$

Eq. (2.18) yields the collapse temperature:

$$T_C = \frac{\chi_c\bar{\epsilon}}{2} + \tfrac{1}{2}\sqrt{\chi_c^2\,\bar{\epsilon}^2 + 2\chi_c b^2}. \tag{2.20}$$

Note that even when there is no net homopolymeric attraction ($\bar{\epsilon} = 0$), random interactions can induce collapse in the heteropolymer at a temperature

$$T_{\rm C}^0 = b\sqrt{\frac{\chi_c}{2}}. \tag{2.21}$$

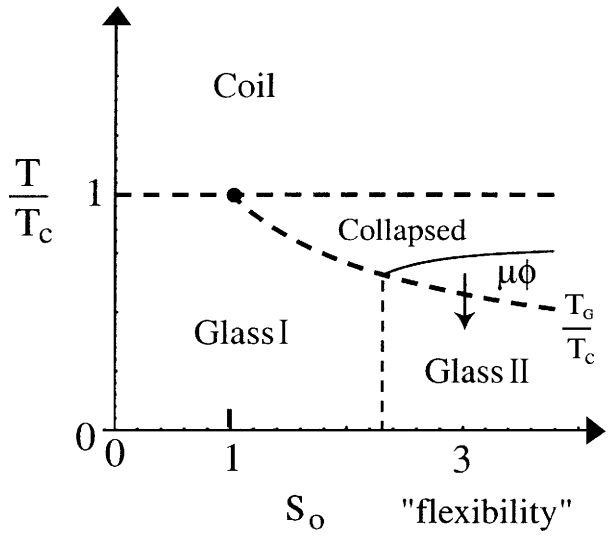

Fig. 2. Phase diagram for a RHP (cf. with Fig. 19). The axes are temperature in units of the collapse temperature, and entropy per residue, which is a measure of the flexibility of the chain. The coil phase is separated from the glass and collapsed phases by second-order transitions, as is the collapsed to glass phase. For sufficient flexibility, a microphase-separated phase may appear depending on the nature of the interactions (see text).

For a heteropolymer with zero net attraction ($\bar{\epsilon} = 0$), the T_G where the entropy vanishes must always be below the collapse temperature, T_C^0, in Eq. (2.21) (Bryngelson & Wolynes, 1990). To see this, assume the converse, i.e. that $T_G > T_C^0$. Then we rewrite Eq. (2.7) as

$$T_G' = \sqrt{\frac{\Delta^2(\eta)}{2\,S_0}}, \tag{2.22}$$

where

$$\Delta^2 = z_c N \eta b^2 \tag{2.23}$$

[this is of the form of Eq. (I-5.14), with $Q = 0$]. Here $\eta = Nv/V$ is the packing fraction, where v is the excluded volume per residue. If the chain is above the collapse transition, the total volume occupied $V = R_g^3 \simeq vN^{\frac{9}{5}}$ (Flory, 1953) and $\eta \simeq N^{-\frac{4}{5}}$, so $\Delta^2 \sim N^{\frac{1}{5}}$. Since the entropy loss at the glass transition scales like $\sim N$, T_G' in Eq. (2.22) scales like $\sim N^{-\frac{2}{5}}$, and so must be $\ll T_C$ as N becomes large, in contradiction with our original assumption. A similar proof by contradiction can be made to show the glass temperature is below the θ point (Bryngelson & Wolynes, 1990). We conclude then that Eq. (2.7) should be written for a collapsed heteropolymer

$$T_G = b\sqrt{\frac{z_c}{2s_0}}. \tag{2.24}$$

Then a phase diagram can be constructed for the RHP in Fig. 2. Here the axes are temperature in units of the collapse temperature, and s_0, which is a measure of the flexibility of the chain. For chains more flexible than $s_0 = 1$, the glass transition curve follows

$T_G/T_C = s_0^{-\frac{1}{2}}$, and the collapse and glass transitions are distinct. For stiffer or lower dimensional chains (with $s_0 < 1$), the glass transition and collapse occur concurrently by the argument given above.

If the residue–residue interaction energies have a few discrete values or are sufficiently distinct, microphase separation may also occur below the collapse temperature (Sfatos *et al.* 1994). This transition line should increase with flexibility since more entropy is lost to phase separate stiffer polymers, as described in Section I-4.4, i.e. microphase separation can be destroyed or induced by increasing the stiffness or flexibility of the polymer chain. While the microphase transition is first order with latent heat, the collapse and freezing transitions are second order.[1]

The glass II phase in Fig. 2 is different than the glass I phase, in that the specific microphase separated basin is favored over all other low-energy basins on the landscape. Since relaxation times diverge in the glass phase for a bulk system, kinetics becomes important in determining what state will be observed in practice. If the glass II region is approached from above as indicated by the arrow in the figure, the system is frozen into the basin corresponding to the microphase separated state, and has residual entropy within that basin. In contrast, the glass I phase has essentially no configurational entropy. If the glass II phase is approached from the left, the slow kinetics of the glassy state prohibits the formation of the microphase separated state, for a large system.

We will see later in Section 5.7 that a similar phenomenon occurs in the context of folding, where at low temperatures the state of a protein is one in which it is frozen into an ensemble of substates in the native basin, so long as the temperature-dependent energy function is not significantly altered (Austin *et al.* 1975). Just as the glass I phase is avoided in microphase separation, a glass I phase is avoided in low-temperature proteins by the presence of a folded state at higher temperature.

2.4 Basic concepts of the entropy of topologically constrained polymers

A theory capable of predicting folding mechanisms from the Hamiltonian must be able to quantitatively describe the free-energy landscape the protein folds upon. The free-energy landscape is constructed by taking an order parameter, and quantifying the number of states and distribution of energies of these states at a given value of the order parameter.

In the context of folding, we take as a first approximation a global scalar parameter Q describing the overall fraction of native contacts present ($0 \leqslant Q \leqslant 1$). Later in Section 7 we generalize this to a field $\mathbf{Q}$ whose components Q_i ($1 \leqslant i \leqslant M$) give the equilibrium probability native contact i is made in the thermal ensemble at a given Q.

In this section we focus on the calculation of the configurational entropy of a heteropolymer under topological constraints. We will apply the entropy as derived here to the thermodynamics of folding, the glass transition, and to folding kinetics.

The entropy depends in principle on the reference configuration, and on which particular contacts are shared. We begin with a mean-field analysis here, so that entropy fluctuations between contact patterns with the same total number of contacts are not accounted for, and neither are any specific properties of the reference configuration. We begin to take these features into account in Section 7. The topological constraints are taken to be the

[1] However the collapse transition may become first-order-like for stiff chains (Lifshitz *et al.* 1978), or when interactions are cooperative.

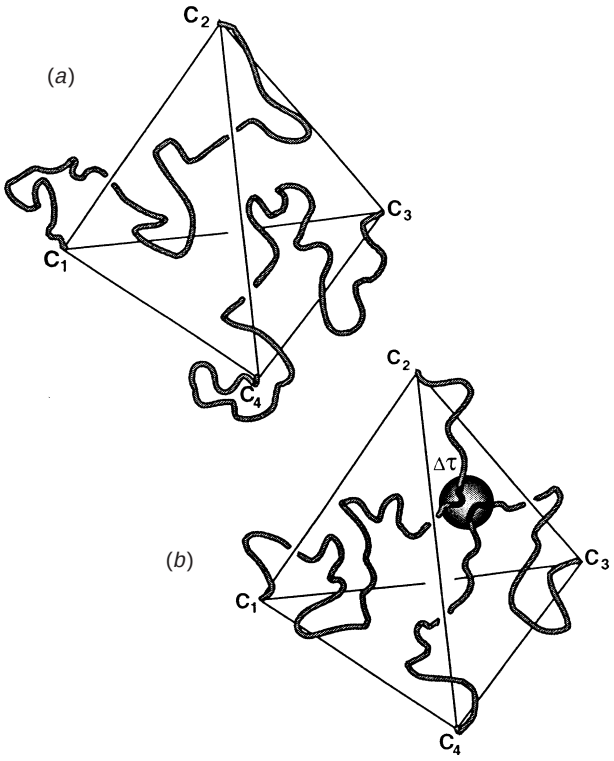

Fig. 3. Allowable configurations of polymer strands (*a*) before and (*b*) after bond formation. Each pair of bonded mers has 4 nearest cross-linked neighbors.

fraction of shared contacts q with a given typical configuration, which can be arbitrarily chosen.

Given the fraction of shared contacts q and packing fraction η, the chain configurational entropy $S(q, \eta)$ is estimated as a sum of 4 terms, described below (Plotkin *et al.* 1996):

$$S_{\text{low}}(q, \eta) = S_0(\eta) + \Delta S_{\text{B}}(q, \eta) + \Delta S_{\text{rout}}(q, \eta) + \Delta S_{\text{AB}}(q, \eta). \tag{2.25}$$

The first term is the entropy of an unconstrained polymer at density η, given by Eq. (4.1) of Part I:

$$S(\eta) = N \ln \mu \approx N \left[\ln \frac{\nu}{\text{e}} - \left(\frac{1-\eta}{\eta} \right) \ln (1-\eta) \right], \tag{2.26}$$

where ν is the number of conformational states per monomer and η is the packing fraction (given by the total volume of the residues over the effective volume the polymer occupies, $0 < \eta < 1$). The remaining terms describe the entropy loss from the unconstrained state, as contacts are randomly added.

Figure 3 illustrates the calculation of the reduction in chain configurational entropy $\Delta S_{\text{B}}(q, \eta)$ due to the addition of specific cross-links in the polymer chain, as first derived by Flory (1956). Consider the region of a cross-linked polymer around a given cross-link about to be formed. Each cross-link and its two associated monomers has four neighboring cross-links denoted C_1, C_2, C_3, C_4 in Fig. 3. We seek the fraction of allowable states that are consistent with the formation of a specific cross-link, $\omega \Delta \tau$, assuming that if the specific cross-

linked monomers are within a volume $\Delta\tau$ of each other then a cross-link is formed. Considering the system to be composed of four separate chains, $\omega\Delta\tau$ equals the probability that all four chains meet in $\Delta\tau$, divided by the probability that the chains meet anywhere in pairs (restoring the allowable configurations in the unbonded initial structure). The probability of forming a cross-link is then given by

$$\omega\Delta\tau = \Delta\tau \frac{\int \mathrm{d}\tau\, G_1(\mathbf{r}_1)G_2(\mathbf{r}_2)G_3(\mathbf{r}_3)G_4(\mathbf{r}_4)}{\int \mathrm{d}\tau\, G_1(\mathbf{r}_1)G_2(\mathbf{r}_2) \int \mathrm{d}\tau\, G_3(\mathbf{r}_3)G_4(\mathbf{r}_4)}, \tag{2.27}$$

where $G_i(\mathbf{r}_i)$ is the chain propagator from position C_i to the volume element $\Delta\tau$, whose vector is $\mathbf{r}_i$. The integrations extend over all space – the specific contact is free to move anywhere.

Performing the integrations in Eq. (2.27) for Gaussian propagators gives the entropy reduction in forming $\mu = qN\chi_c\eta$ specific total cross-links for an ideal polymer chain. The calculation is mean field in that the mean free-chain length when μ contacts are present, $N/2\mu$, is used in calculating the propagators in Eq. (2.27). For polymers in 3 dimensions the entropy reduction is

$$\Delta S_{\mathrm{B}}(q, \eta) = \tfrac{3}{2} N(q\chi_c\eta) \ln(Cq\chi_c\eta), \tag{2.28}$$

where C is a constant of order $\mathcal{O}(1)$ involving the ratio of the contact radius to the persistence length. The change in entropy due to the addition of contacts is negative, as plotted in Fig. 4.

If we imagine the ensemble of configurations that have a given amount of order, say a given number Mq of similar contacts to a given structure, then within this ensemble there are a multiplicity of sub-ensembles of states having different sets of Mq contacts. These are the core-halo ensembles described in Section I-5 in the context of folding, which can be identified as a measure of the number of distinct routes in folding to the native state, or to an arbitrary state in a description of configurational diffusion. Each sub-ensemble contains many states corresponding to the entropy of the disordered polymer around the particular core (e.g. see inset of Fig. 10, Part I). We define the entropy that corresponds to the degeneracy of contact patterns at q as $S_{\mathrm{rout}}(q)$ ($S_{\mathrm{rout}} > 0$), while the configurational entropy lost from the coil state to form that set of contacts is $\Delta S_{\mathrm{B}}(\Delta S_{\mathrm{B}} < 0)$.

In capillarity models of nucleation (Becker & Doring, 1935), S_{rout} corresponds to the log of the translational partition function (Lothe & Pound, 1962; Reiss *et al.* 1967; Lothe & Pound, 1969) which scales logarithmically with system size, plus the entropy of surface fluctuations of droplets of a given size (Langer, 1967; Fisher, 1967) which correspond to logarithmic terms in the expansion of the free energy density. This translational entropy is small compared to the total conformational entropy, however at the spinodal where the free-energy profile $F(q)$ becomes downhill [e.g. $F(Q)$ curves in the third row of Fig. 31], the nucleus is of small amplitude and highly ramified (Gunton *et al.* 1983; Unger & Klein, 1984). In this regime the droplet structure is percolative as in spinodal decomposition of binary fluids, and the capillarity approximation is poor. Field-theoretic descriptions for the structure of the droplet are typically used in this regime (Cahn & Hilliard, 1958; Langer, 1969). Binary fluid approximations to the route entropy in proteins which scale extensively with system size have been used in this limit (Bohr & Wolynes, 1992; Plotkin *et al.* 1996, 1997; Pande *et al.* 1997; Shoemaker *et al.* 1997, 1999; Shoemaker & Wolynes, 1999). The amount of route diversity in folding has also been analyzed in terms of the Shannon entropy (Fernández *et al.* 2000), which is similar in spirit to the

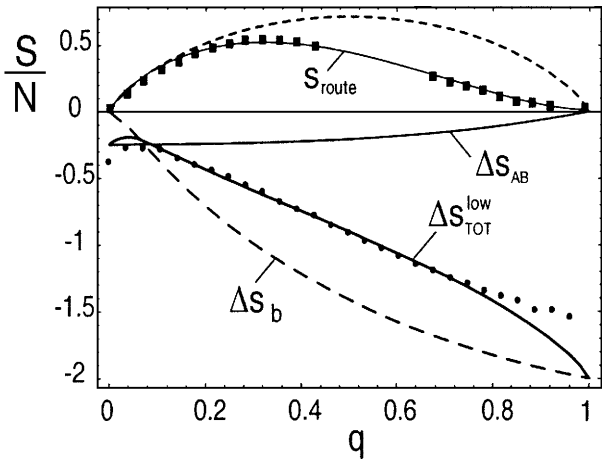

Fig. 4. Entropy contributions (divided by N) for a weakly constrained polymer. Here the length $N = 27$, and the packing fraction $\eta = 1$. – – –, Entropy loss ΔS_b due to the formation of contacts [Eq. (2.28)]. —, Entropy loss ΔS_{AB} due to the elimination of forbidden configurations which would cause the overlap to exceed q. This 'anti-bond' term becomes larger for more compact polymers and for longer polymers [Eq. (2.32)]. - - - -, Putative binary fluid mixing entropy in the absence of the polymer backbone, given through Eq. (2.29). ■—■, Data and theory for the route entropy associated with the number of core configurations consistent with q [Eqs. (2.31*a*) and (2.31*b*)]. S_{rout} includes a prefactor $(1-q^{\alpha})$ corresponding to the entropic asymmetry of applying contacts to an unconstrained polymer and removing contacts from a fully constrained polymer, described in the text. The data are for the 27-mer lattice model structure shown in Fig. 27*a* (Nymeyer, unpublished results), and are obtained for low q values by making subsets of $M(1-q)$ contacts repulsive, Mq contacts attractive, and then finding the most native-like state in a low temperature quench. For high q values they are obtained by making random sets of $M(1-q)$ contacts repulsive, and counting the remaining native cores which are distinct. This method finds the reduction in binary fluid mixing entropy due to chain connectivity and particular native topology of the protein under study. The computation treats all contact formation probabilities on an equal footing (all $q_i = q$), and so the conformational route entropy plotted is an upper limit to the actual thermal route entropy present. ●—●, Total entropy loss for the weakly constrained polymer. Adding the constant s_0 to this gives Eq. (2.25). Finite-size effects add further modifications to the theory for small values of q (Plotkin *et al.* 1996).

following treatment (Plotkin & Onuchic, 2000). We make no capillarity or spinodal assumptions, and treat the route entropy $S_{rout}(\{q_i\})$ as a fairly simple modification of the entropy of a binary fluid mixture (Landau & Lifshitz, 1980):

$$\exp S_{bf}(q) = \frac{M!}{Mq!(M-Mq)!} \cong (\Omega_i^{bf})^M \tag{2.29}$$

$$\Omega_i^{bf} = q^{-q}(1-q)^{-(1-q)}, \tag{2.30}$$

which we interpret here as the product of the complexities per contact Ω_i and is readily generalized to the case where the complexities are not all equal: $\exp S_{bf}(\{q_i\}) \Rightarrow \prod_{i=1}^{M} q_i^{-q_i}(1-q_i)^{-(1-q_i)}$.

There are two principle modifications from the simple mixing entropy in Eq. (2.30) for proteins. One is that as noted above, due to fluctuations in energetics and chain entropy, not all contacts are occupied with equal probability in the thermal ensemble at overall similarity We study this in Section 7 which focuses on heterogeneity in folding. The other is that, q. due to chain connectivity, as contact density increases, there is less sterically allowed space

for a monomer to move around when one of its constraining contacts is broken. Thus not all $M!/Mq!(M-Mq)!$ contact patterns have an entropy $\approx Ns_0+\Delta S_B$. In other words making some contacts forces spatially nearby contacts to be made because the corresponding monomers are forced to be in each other's proximity. So there is a reduction from the putative complexity $(\Omega_i^{bf})^M$ since not all M contacts are independently contributing to mixing, with several contact patterns corresponding to the same constrained state.

This further entropy reduction is subtracted off of the mixing entropy entropy in Eq. (2.30). In Plotkin & Onuchic (2000, 2002), this reduction was taken into account by introducing a phenomenological prefactor $\lambda(q)$ to yield the total route entropy for a polymer system:

$$S_{rout}(q) = \lambda(q)[-q\ln q-(1-q)\ln(1-q)] \tag{2.31a}$$

$$\lambda(q) \equiv 1-q^{\alpha}. \tag{2.31b}$$

The factor $\lambda(q)$ measures the entropy reduction due to the coupling of chain connectivity with the topology of the reference state. The power α in $\lambda(q)$ should be a decreasing function of the persistence length, and also of system size N, since for larger systems more polymer is buried and thus more strongly constrained by surrounding contacts. Allowing fluctuations in contact probabilities $q \to q_i$ will lower the route entropy, but will also turn out to lower the magnitude of bond entropy loss.

Specifying the overlap q introduces an additional entropy reduction due to the fact that $Nz_c\eta - qNz_c\eta$ contacts of the reference state must *not* be formed, since adjacent residues are assumed to be bonded. This 'anti-bond' entropy reduction is largest for small overlaps, and goes to zero as $q \to 1$. It is given by Plotkin *et al.* (1996)

$$\frac{1}{N}\Delta S_{AB}(q,\eta) = \frac{1}{C}\int_{Cqz_c\eta}^{Cz_c\eta} dx \log(1-x^{\frac{3}{2}}), \tag{2.32}$$

where C is the same coefficient in Eq. (2.28).

The sum of Eqs. (2.26), (2.28), (2.31*a*), and (2.32) gives the total entropy in Eq. (2.25), which is plotted in Fig. 4 for a model chain of length $N = 27$ in 3 dimensions, believed to model the folding of small, single domain proteins (Onuchic *et al.* 1995). The total entropy and route entropy agree well with the values obtained from lattice simulations.

The theory gives a maximum number of states at a small, non-zero value of structural overlap, q_{min}. Simulations reveal that q_{min} does not tend to zero as N becomes large, but converges to a small number of about 0.01–0.1, depending on the amount of homopolymer attraction (Bastolla & Grassberger, 2001). To see this and obtain an estimate of q_{min}, consider two random flight chains of length N. The probability a contact of length l is shared between the two replicas is the probability of successful first return for both chains. Taking the chains to be Gaussian,

$$P(l)^2 \simeq \left(\frac{c(d)}{l^{d/2}}\right)^2 \tag{2.33a}$$

$$c(d) \simeq \left(\frac{3}{2\pi}\right)^{d/2}\left(\frac{r_B}{a}\right)^d, \tag{2.33b}$$

where r_B is the bond radius and a is the persistence length. It is possible to generalize the result for self-avoiding chains, which results in a smaller value of q_{min}. From Eq. (2.33*a*), the

probability a residue in both replicas at position i on the chain participates in a contact (of any length) is

$$p_i \simeq \sum_{\substack{j=1 \\ j\neq i}}^{N} \frac{c^2}{|i-j|^d} \simeq \frac{c^2}{d-1}\left(2-\frac{1}{(i-1)^{d-1}}-\frac{1}{(N-i)^{d-1}} \right), \tag{2.34}$$

where we have approximated the events as having small and independent probability of return.

For long chains $i \gg 1$ and $N \gg 1$ and the last two terms in parentheses $\to 0$. The average number of shared contacts between the chains $\bar{n}$ is then $Np_i/2$, since there are 2 residues per contact. The average fraction of the total possible shared contacts $q_{\min}$ is then $\bar{n}/N\tilde{z}_c$ or

$$q_{\min} \simeq \frac{c^2}{\tilde{z}_c(d-1)}. \tag{2.35}$$

Note that $q_{\min} \to 0$ as the dimension $d \to \infty$. We can now obtain a number for polymers on a $d = 3$ cubic lattice, for which the maximum number of contacts per residue $\tilde{z}_c$ approaches 2 as $\tilde{z}_c \approx 2-3N^{-\frac{1}{3}}$ (Douglas & Ishinabe, 1995), and for which the bond volume r_B^3 is 4 sites and the lattice spacing $a \equiv 1$ functions as the persistence length. Then

$$q_{\min}^{3D} \simeq \frac{c^2}{4} = \left(\frac{3}{2\pi}\right)^3 \approx 0.11. \tag{2.36}$$

This number is slightly larger than the number for self-avoiding walks, since the ideal chain approximation was used. Nevertheless, the fact that $q_{\min}$ does not tend to zero as $N \to 0$ means that energetic correlations between chain replicas are always present, and, for example will broaden the glass transition from the REM behavior even in the bulk limit.

When the number of contacts present exceeds the number of residues and there is more than one contact per residue on average, the mean-field Flory theory undergoes an entropy crisis and is longer valid. At some point before this, configurations having fluctuations from the mean-field contact pattern begin to dominate the free energy. It then becomes more accurate to switch the description of entropy loss from that due to a dilute 'gas' of contacts, to an atomistic description ascribing entropy to lengths of chain melted out from the frozen ($q = 1$) three-dimensional (3D) reference structure, and the combinatorics of these pieces of melted chain (Plotkin *et al.* 1996).

It is appropriate then in this regime to start from a reference state in which all the bonds are formed, and the polymer is 'frozen' into the reference structure, which may be the native structure. By switching from the contact representation used at low q to an atomic representation, we can study how certain parts of the frozen polymer are melted out by keeping track of which residues are still in their correct geometrical positions relative to the 3D structure of the reference state (see Fig. 5, upper inset). The melted pieces each carry a certain amount of entropy, and there is also a mixing entropy associated with the different places that the given melted pieces can occur along the sequence of the polymer. The process of melting physically involves the collective freeing up of several monomers at once, i.e. at least some critical number $l_c > 1$ of monomers must be free for the melted strand to have any entropy. Each melted piece of segment length l then has an internal partition function for its entropy

$$\tilde{z}(l) \cong \mu^{l-(l_c-1)}. \tag{2.37}$$

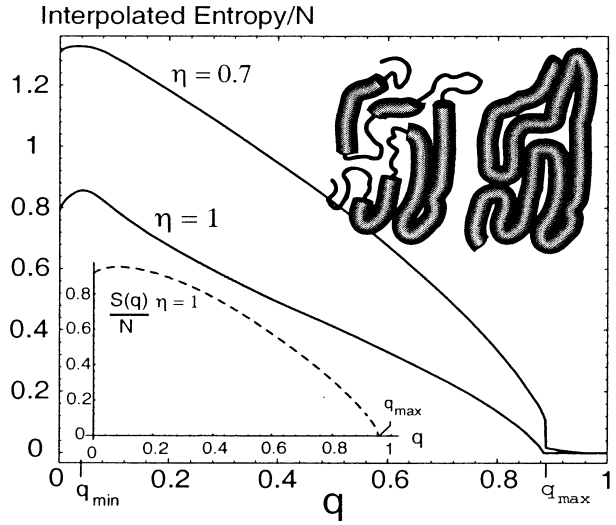

Fig. 5. Configurational entropy of a topologically restricted polymer, for a 3D 27-mer. The lower inset (- - -) is the high-q entropy which is accurate for a strongly constrained polymer [shown here for a 64-mer; cf. Eq. (2.38)]. The solid curves are interpolations between the high-q and low-q entropy formulae, for two different overall packing densities, $\eta = 1$ (Hamiltonian walks) and $\eta = 0{\cdot}7$. The value of $q_{\min}$ is where the entropy is maximal [see Eq. (2.36)]. The value of $q_{\max}$ is related to the minimal amount of polymer which must be melted out to yield entropy. It is a finite-size effect in that $q_{\max} \to 1$ as $N \to \infty$. *Upper inset*: illustration of a polymer in the geometrical configuration of the reference state ($q = 1$), and for a partially native structure ($q < 1$). The entropy can be considered to come from melted out strands along the sequence which are not in their correct geometrical positions (dark lines), and the combinatorics of those melted strands along with the frozen trains between melted strands (see text).

In addition the ends are allowed to be freed up in the same fashion, but we expect them to be easier to free up, with a correspondingly smaller value of critical collective length $l_{\mathrm{EC}} < l_{\mathrm{C}}$.

We can then express the total number of states of an entire polymer composed of melted and frozen pieces, along with melted or frozen ends (see Fig. 5, lower inset) at a given q. We can characterize a state microscopically by the number distribution of melted pieces of length l, $\{n_l\}$, the number distribution of frozen pieces of length l, $\{m_l\}$, and of the probability distribution that the ends have length l, $\{p_l\}$ (we treat the ends on equal footing here). As a consequence of specifying the total number of states in terms of the given distributions $\{n_l\}$, $\{m_l\}$, and $\{p_l\}$, there must be a combinatorial factor present associated with the permutation degeneracy given the above distributions. There is also a mixing term pertaining to the end length distributions, which is necessary for the end lengths to have a probability distribution rather than just their mean value. The melted pieces, frozen pieces, and end lengths each have their own internal partition function [given for melted pieces by Eq. (2.37)]. The frozen pieces do not have any internal entropy in the model. So the total number of states is given by Plotkin *et al.* (1996)

$$\Omega_{\mathrm{tot}} = \sum_{\substack{\{n_l\} \\ \{m_l\} \\ \{p_l\}}} \frac{\left(\sum_{l_{\mathrm{c}}}^{N} n_l\right)!^2}{\prod_{l_{\mathrm{c}}}^{N} n_l! \prod_{1}^{N} m_l!} \prod_{l=l_{\mathrm{c}}}^{N} (\mu^{l-(l_{\mathrm{c}}-1)})^{n_l} \prod_{l=l_{\mathrm{EC}}}^{N} \left(\frac{1}{p_l} \mu^{l-(l_{\mathrm{EC}}-1)} \right)^{2p_l}, \tag{2.38}$$

where the total number of melted pieces essentially equals the total number of frozen pieces in a large system (in the particular configuration of the finite-sized system in the inset of

Fig. 5, there are 3 melted and 4 frozen pieces, and 2 melted ends). The sum is over all possible distributions of $\{n_l\}$, $\{m_l\}$, and $\{p_l\}$. Expressions of this form for the number of states have been used in models of the helix-coil transition and DNA denaturation (Poland & Scheraga, 1970; Flory & Matheson, 1984), and in models of polymer adsorption onto a surface (Silberberg, 1962; Hoeve *et al.* 1965).

The entropy at q for a strongly constrained polymer is obtained by maximizing the log of the largest term in Eq. (2.38) subject to the constraints:

$$\sum_{l_c}^{N} n_l = Nf, \quad \sum_{l_c}^{N} l n_l = N(1-q) - 2l_{E,} \tag{2.39a}$$

$$\sum_{1}^{N} m_l = Nf, \quad \sum_{1}^{N} l m_l = Nq, \tag{2.39b}$$

$$\sum_{l_{EC}}^{N} p_l = 1, \quad \sum_{l_{EC}}^{N} l p_l = l_E, \tag{2.39c}$$

where Nf is the total number of melted or frozen pieces. The constraints are derived by noting for example that $\Sigma_1^N l m_l$ in Eq. (2.39*b*) equals the total number of frozen monomers. If there are N_F frozen monomers, there are $z\eta N_F$ frozen bonds. Equating this with $qNz\eta$ bonds gives $N_F = Nq$. The other constraints follow from this type of reasoning.

Maximizing the log largest term of Eq. (2.38) yields exponentially decaying distributions for n_l, m_l and p_l. Substituting these back into the log largest term gives the configurational entropy $S(q, f, l_E)$ as a function of q, the total number of melted or frozen pieces, Nf, and the mean end length, l_E. Then this function can be maximized to obtain the most probable number of melted pieces and end length as a function of q, and finally the configurational entropy as a function of q only, in the strongly constrained regime. The results are shown in the inset of Fig. 5.

The total entropy can then be obtained by interpolating between the weakly and strongly constrained regimes, yielding the curves in Fig. 5.

An interesting extension of the above analysis would be to incorporate topological effects of the reference (native) structure by allowing the entropy of melted pieces to vary depending where they are in the structure. Such an analysis may prove fruitful in understanding the experimental results from hydrogen exchange experiments (Bai *et al.* 1995; Sadqi *et al.* 1999). Simpler versions of the above analysis which restrict conformations to have one up to a few melted and frozen segments, and which incorporate some aspects of native structure, have been applied with some success in predicting folding rates and mechanisms (Munoz & Eaton, 1999; Alm & Baker, 1999; Galzitskaya & Finkelstein, 1999; Guerois & Serrano, 2000; Galzitskaya *et al.* 2001).

The effects of entropic fluctuations due to structural heterogeneity are treated further in Section 7.

3. Beyond the Random Energy Model

Though the REM has produced qualitatively reasonable results either as applied to the heteropolymer glass transition or to non-native trapping in protein folding, it may seem too extreme. Configurations of a system with structural similarity should have similar energies,

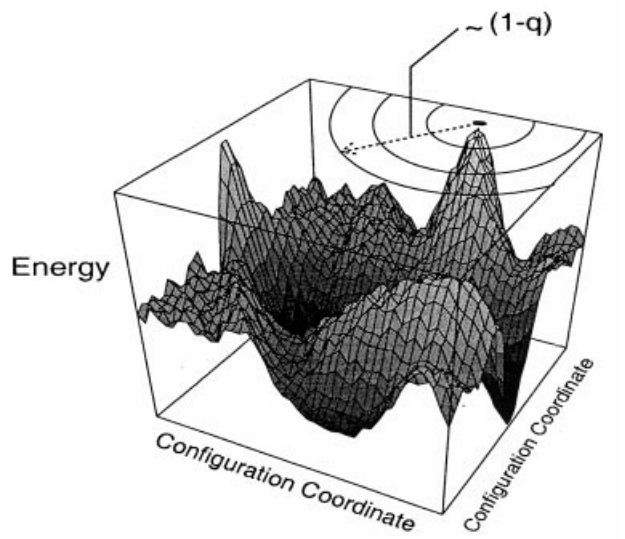

Fig. 6. Qualitative picture of the energy landscape, pictured here as a 2D projection of the multi-dimensional configuration space. We can speak of a distance radius $\sim (1-q)$ from any given state, which measures structural similarity to that state, and determines how correlated the energies of similar states are given the underlying interactions. Correlations smooth out the energy landscape, which affects the nature of the glass transition.

provided interaction ranges are reasonably local and not pathologically many-body. Analogous to random first-order transitions in glasses (Kirkpatrick & Wolynes, 1987; Kirkpatrick *et al*. 1989; Parisi, 2000) and Potts glasses (Gross *et al*. 1985; De Santis *et al*. 1995), many states lie in a given thermodynamic basin, rather than the situation of just one state per basin as in the REM. In fact for proteins, a dominant correlation-induced basin is essential for solving the Levinthal paradox.

For a general disordered system, a model taking into account pair correlations in the energy landscape, and thus capable of calculating disorder-averaged free energies accurate to second order in the partition function, has been defined and solved by Derrida and Gardner (Derrida, 1985; Derrida & Gardner, 1986a, b). Extensions to include higher order correlations are straightforward in principle. The model, known as the generalized random energy model (GREM), is defined by first introducing a similarity measure q to any given state. The parameter q quantifies structural similarity between two configurations of the system, and becomes an order parameter in the analysis. The energies of two states with similarity q are correlated, Gaussian variables with covariance $\langle \delta E_1 \delta E_2 \rangle = \Delta^2(q)$ specified by the underlying interactions. The parameter q functions as a distance measure which stratifies the energy landscape (see Fig. 6). With the landscape thus parameterized, the last defining quantity in the model is the log number of states or configurational entropy $S(q)$ at distance q to a given state, as described in the last section. Thus with a knowledge of the Hamiltonian and configurational phase space of the system, a given disordered system can be mapped to the GREM and solved to give the approximate thermodynamics. This technique can be applied to study the glass transition in a finite-size heteropolymer globule (Plotkin *et al*. 1996).

We can generalize the contact Hamiltonian of Eq. (2.1) to account for many-body interactions of arbitrary order, analogously with p-spin-glass models (Gardner, 1985; Derrida

& Gardner, 1986b). Let a single index i_a label each contact in sets of p contacts, $i_1, i_2, \ldots, i_p$ (there are $\sim N^2$ different pair contacts in the system, and $\binom{N}{p}$ sets of p contacts). Then, generalizing the cut-off function in Eq. (2.1) for p-contact interactions, $\Delta_{i_1}\Delta_{i_1}, \ldots, \Delta_{i_p} = 1$ if *all* p contacts are made, zero otherwise. We associate a 'p-contact' energy with each set, $\epsilon_{i_1, i_2, \ldots, i_p}$. To ensure an extensive energy, p-contact coupling energies must be chosen from the distribution

$$P(\epsilon_{i_1, i_2, \ldots, i_p}) = \left(\frac{M^{p-1}}{2\pi b^2 p!} \right)^{\frac{1}{2}} \exp\left[- \left(\epsilon_{i_1, i_2, \ldots, i_p} \right)^2 \frac{M^{p-1}}{2b^2 p!} \right], \tag{3.1}$$

where $M = N\chi\eta$ is the total number of contacts. The 'many-body' Hamiltonian is then

$$\mathscr{H}_{\mathrm{P}}\{\Delta_i\} = \sum_{1 \leqslant i_1 < i_2, \ldots, < i_p \leqslant M} \epsilon_{i_1, i_2, \ldots, i_p} \Delta_{i_1} \Delta_{i_1, \ldots,} \Delta_{i_p}. \tag{3.2}$$

The probability a state has energy E is simply a Gaussian distribution:

$$\left.\begin{aligned} P(E) &= \langle \delta(E - \mathscr{H}_{\mathrm{P}}\{\Delta_i\}) \rangle \\ &= \int_{-\infty}^{\infty} \prod_{1 \leqslant i_1 < i_2, \ldots, < i_p \leqslant M} \mathrm{d}\epsilon_{i_1, i_2, \ldots, i_p} P\left(\epsilon_{i_1, i_2, \ldots, i_p}\right) \delta(E - \mathscr{H}_{\mathrm{P}}\{\Delta_i\}) \\ &= \frac{1}{(2\pi M b^2)^{\frac{1}{2}}} \mathrm{e}^{-E^2/2Mb^2}. \end{aligned}\right\} \tag{3.3}$$

The last equality is obtained by Fourier transforming the delta function and performing the Gaussian integrals. The final Gaussian distribution has a variance scaling extensively, which justifies using Eq. (3.1).

Given two different configurations, $\{\Delta_i^a\}$ and $\{\Delta_i^b\}$, the probability they have energies E_a and E_b, respectively is

$$\left.\begin{aligned} P_q(E_a, E_b) &= \langle \delta(E_a - \mathscr{H}_{\mathrm{P}}\{\Delta_i^a\}) \delta(E_b - \mathscr{H}_{\mathrm{P}}\{\Delta_i^b\}) \rangle \\ &= \frac{1}{M\pi b^2} \frac{1}{(1 - q^{2p})^{\frac{1}{2}}} \exp\left[- \frac{(E_a + E_b)^2}{4Mb^2(1 + q^p)} - \frac{(E_a - E_b)^2}{4Mb^2(1 - q^p)} \right], \end{aligned}\right\} \tag{3.4}$$

where

$$q = \frac{1}{M} \sum_{i=1}^{M} \Delta_i^a \Delta_i^b \tag{3.5}$$

is the fraction of shared contacts between configurations a and b, and measures their structural overlap.

There are two particularly important cases of Eq. (3.4) (Derrida, 1981). When the number of contacts p necessary for a given energetic interaction becomes large, $q^p \to 0$ for essentially all q, and the distribution factorizes:

$$P_q(E_a, E_b) \to P(E_a) P(E_b). \tag{3.6}$$

The states become uncorrelated for any $q < 1$: Eq. (3.6) is the pair distribution in the REM. Another important limit of Eq. (3.4) is when $p = 1$, which yields the two-point distribution for a Hamiltonian with pair interactions. Equation (3.4) can be generalized to the case where the densities of the two conformations are not equal (Plotkin *et al.* 1996). It is an interesting future topic to investigate Eqs. (3.1) and (3.2) in the limit that the p contacts belong to a spatially contiguous cluster of residues, as in capillarity models of folding and dynamics.

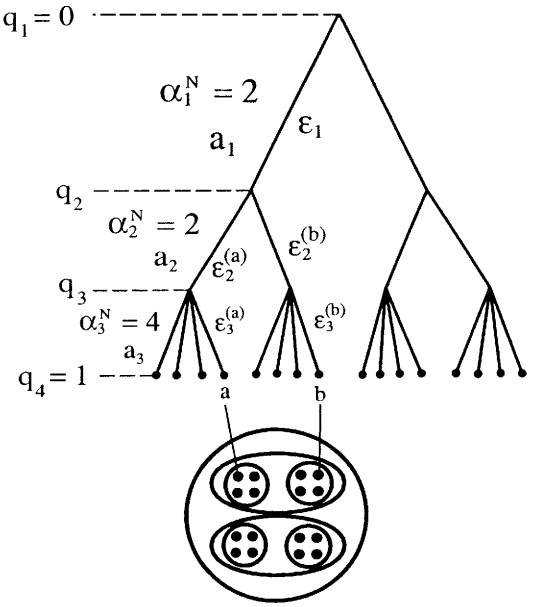

Fig. 7. The ultrametric tree construction used in the GREM model; the parameters q_i, α_i^N, a_i, and $\epsilon_i^{(\beta)}$ are described in Appendix B.

3.1 The GREM and the glass transition in a finite RHP

One can gain insight into the nature of a glass transition by applying the GREM formalism to the RHP. Energetic correlations as well as the structure of the conformational entropy $S(q)$ can modify the transition. For an outline of the GREM construction, see Appendix B and Derrida (1985), Derrida & Gardner (1986b).

The derivation of the free energy in the GREM involves essentially the same concepts as in the REM, but with the modification that instead of the *total* energies of different states being uncorrelated, the contributions to the energies $\epsilon_i^{(\beta)}$ on the branches of an ultrametric tree at the ith level are uncorrelated (see Fig. 7), with the nodes of the ultrametric tree representing the total energies of the states. A freezing temperature associated with each level i involves the same competition between roughness and entropy loss as before, but now the competition is between the decrease in roughness as we move towards a given state an increment $\mathrm{d}q$, and the loss in entropy for the same increment $\mathrm{d}q$. The T_G in Eq. (2.7) is replaced by a q-dependent glass temperature:

$$T_G(q) = \left(\frac{(zb^2)\,(\mathrm{d}v(q)/\mathrm{d}q)}{-2(\mathrm{d}s/\mathrm{d}q)} \right)^{\frac{1}{2}}, \tag{3.7}$$

where $s(q)$ is the conformational entropy per residue at q, and $v(q)$ is a measure of the covariance of the energies of two states and is given through Eq. (B 5). Comparison between Eqs. (3.4) and (B 5) gives $v(q) = q^p$. For a Hamiltonian with pair-interactions ($p = 1$),

$$\frac{T_G(q)}{b\sqrt{z/2}} = \left(-\frac{\mathrm{d}s(q)}{\mathrm{d}q} \right)^{-\frac{1}{2}}, \tag{3.8}$$

where $s(q)$ can be obtained from the methods of Section 2.4 (Fig. 5).

The glass transition temperature $T_G(q)$ describes how upon cooling the system becomes frozen into ergodically separated basins of states when correlations are present. As the temperature is further lowered, the model predicts how the basins shrink to one frozen configuration as occurs at the REM transition.

The glass transition can be investigated only for moderately high polymer densities for the reasons given in Section 2.3. At moderate densities ($\eta < 1$), the system is understood to have some residual entropy even after freezing due to the parts of the polymer that were not interacting. For the two entropy curves in Fig. 5, the glass temperature curves, $T_G(q)$ are shown in the inset of Fig. 8. For moderately high packing fraction $\eta \simeq 0.7$, the curve monotonically decreases, while at full packing fraction $\eta = 1$ the curve has a maximum. Both curves diverge as $q_{\min}$ is approached from above, for the reasons leading to Eq. (2.36). Analogously, two paramagnets in the same field H tend to have an overlap with each other of at least the magnetization $m(H)$.

These two cases have qualitatively different glass transition behaviors in the GREM. When one applies a single breaking of replica symmetry (one-branch on the ultrametric tree), one recovers the free energy of the REM (Gross & Mézard, 1984). It is possible to apply the Parisi ansatz for the structure of the replica symmetry breaking, and then one recovers the free energy of the GREM, as long as the inverse of the replica-symmetry breaking-order parameter $q(x)$ has the form (Derrida & Gardner, 1986a):

$$x(q) = \begin{cases} 0 & 0 < q < q_{\min} \\ \dfrac{T}{T_G(q)} & q_{\min} < q < q_{\max}(T) \\ 1 & q_{\max}(T) < q < 1, \end{cases} \tag{3.9}$$

when $T_G(q)$ has the monotonically decreasing form of the $\eta = 0.7$ curve in Fig. 8 inset. When $T_G(q)$ has a single maximum as in the $\eta = 1$ curve in Fig. 8, inset, $x(q)$ is given by:

$$x(q) = \begin{cases} 0 & 0 < q < q_{\min} \\ \dfrac{T}{T_G^0} & q_{\min} < q < q_g^0 \\ \dfrac{T}{T_G(q)} & q_g^0 < q < q_{\max}(T) \\ 1 & q_{\max}(T) < q < 1. \end{cases} \tag{3.10}$$

One of the upshots is that correlations in the landscape significantly reduce the temperature at which the system is frozen in *one* particular low-energy state, as expected. However, for a RHP with 2-body interactions, the T_G, where the system is now frozen into one of many distinct basins of states, is approximately 5–10% of the REM glass transition temperature. In Eq. (3.10), q_g^0 is the basin size at temperature $T_G^0 \equiv T_G(q_g^0)$ where freezing begins (see Appendix B). This temperature, plotted in Fig. 8 as a function of packing fraction η, is approximately 5–10% of the REM glass transition temperature. Perhaps somewhat surprisingly correlations on the landscape have not significantly modified the temperature at which the heteropolymer system becomes glassy in the thermodynamic sense, because even though the effective energetic variance is reduced, so is the entropy lost at the transition. The residual entropy at the transition comes from the fact that at T_G^0, the system is ergodically localized into basins of states with an extensive amount of entropy, rather than just one state as in the REM. When the interactions are very many-body [large p in Eq. (3.4)], the REM

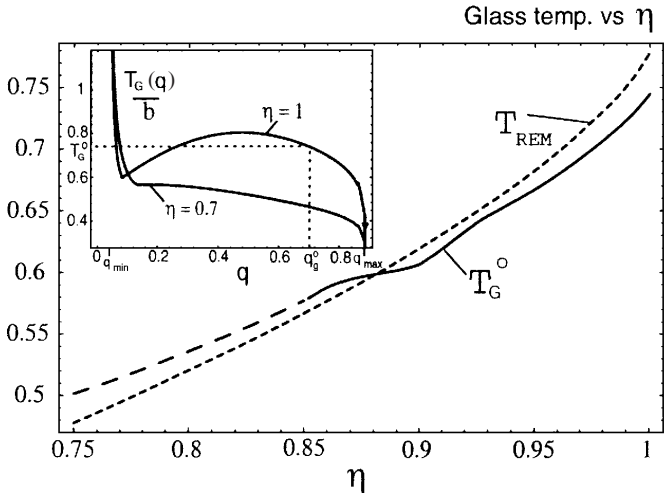

Fig. 8. The temperature T_G^0 at the onset of freezing (—), plotted with the REM freezing temperature T_{REM} (- - -). At $\eta < \eta_c \simeq 0{\cdot}85$ the mechanism behind the glass transition changes from that in Eq. (3.10) to that in Eq. (3.9). Below this density T_G^0 is not precisely defined, but may be estimated (Plotkin *et al.* 1996). *Inset*: glass temperature curves $T_G(q)$ given by Eq. (3.8), which govern the nature of the replica symmetry breaking transition in the GREM. q_g^0 is the basin size at T_G^0 where freezing begins, where q_g^0 and T_G^0 are given by Eqs. (B 14)–(B 16).

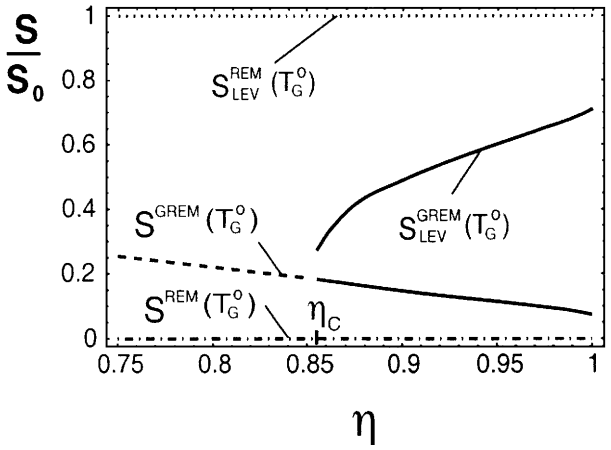

Fig. 9. Levinthal entropy (remaining configurational entropy) and thermal entropy, at T_G^0 for both the REM and the GREM, in units of the total configurational entropy S_0. For the REM the thermal entropy at the glass transition is zero (-·-·-), and the Levinthal entropy is S_0 (·····). The configurational entropy per basin is zero, so the number of basins to be searched at the glass transition is the total number of states. For the GREM, the thermal entropy at the transition is $\sim$ 10–20% of the total entropy, and the Levinthal entropy corresponding to the number of basins to be searched is between about 40–70% of the log total number of states, depending on the density. This is because at T_G^0 there is a significant configurational entropy per basin, which decreases only upon further cooling. At $\eta < \eta_c$ the freezing mechanism changes from that in Eq. (3.10) to that in Eq. (3.9).

result is recovered; between these two regimes the transition temperature varies very little, but the basin entropy changes significantly.

To see this, the Levinthal and thermal entropy are plotted *versus* η for the GREM and compared to the REM results in Fig. 9. Even though the temperature at which the glass

transition occurs did not significantly change, the entropy to be searched at the transition is significantly less. These effects lead to the much smaller Levinthal search time at the glass transition. For example at $\eta \approx 0.95$, the Levinthal entropy on the correlated landscape at the thermodynamic glass temperature is $\approx 0.6\, S_0$. Let the search take place in a polymer that has collapsed and has the effective number of residues reduced by the helix-coil transition. We will assume here that the polymer has not microphase separated or nematically ordered. Then from the arguments of Section I-4 which led to Eq. (I-4.15), correlations reduce the Levinthal search time from $(10^{-12}\text{ s}) \exp N(s_0/2-1) \sim 10^{103}$ yr for Barnase [where Eq. (I-2.2) was used for s_0], to

$$\tau_{\rm F}^{\rm corr} = (10^{-12}\text{ s}) \exp N \left(\frac{0.6\, s_0}{2} - 1 \right) \sim 10^{30}\text{ yr}. \tag{3.11}$$

This number is significantly larger than the number obtained in Eq. (I-2.30) and Section 4 from kinetic arguments on the correlated landscape, $S_{\rm Lev} \approx 0.3\, S_0$. This is because correlations in the landscape reduce the barriers between basins in addition to the total number of basins. The reduced height of the barriers reduces the time in a Levinthal search; this effect is observed in a kinetic rather than thermodynamic analysis. Taking the estimate for the reduced conformational entropy to be searched at the glass transition from Eq. (3.11), and using this as $S_{\rm MG}$ in Eq. (I-2.30) for the kinetic search time, we obtain

$$\langle \tau \rangle^{\rm corr}(T_{\rm G}) \approx (10^{-12} - 10^{-9}\text{ s}) e^{0.3N(0.6\, s_0/2-1)} \sim 10\text{ min.} - 10^2\text{ h}. \tag{3.12}$$

depending on the reconfiguration time. By considering dynamics on a correlated landscape, we have shown here how a glassy random search is a feasible folding mechanism for some very slow folding proteins. Of course, in addition to the issue of kinetic accessibility, the issues of stability and robustness become important for this class of sequences.

The replica-symmetry breaking-order parameter $q(x)$ is plotted in Fig. 10*a* for $\eta = 1$ and $\eta = 0.7$, corresponding to the two cases in Eqs. (3.9) and (3.10). The temperature is taken to be about $(\frac{1}{2})T_{\rm G}$, with $T_{\rm G}$ is given by Eq. (2.24). Also plotted in Fig. 10*b* is the probability distribution of similarity parameter q, $P(q)$, defined as the derivative of Eqs. (3.9) and (3.10), $dx(q)/dq$. That is, $x(q) = \int_0^q dq'\, P(q')$ is the probability two replicas have overlap less than q (Mézard *et al*. 1984). For maximally collapsed heteropolymers, the order parameter retains a large discontinuous jump, as in the REM transition. This means there is a sudden ergodic localization to basins of a characteristic size q_g^0. There are many basins since there is only a fraction of the total entropy counting all the states within q_g^0 of a given structure, and these basins contain dissimilar structures, because the low q peak in the overlap probability distribution function $P(q)$ occurs at $q_{\rm min}$.

There is a critical value of the density $\eta_c \simeq 0.85$ for $N = 27$, where the order parameter $q(x)$ changes from discontinuous to continuous as density is lowered. Appealing to conventional spin-glasses in the presence of a magnetic field, this can be thought of as the analog to a tricritical point on the de Almeida–Thouless line for the spin-glass transition in the field-temperature plane of the phase diagram (de Almeida & Thouless, 1978). Here the line is in the 'hydrophobicity'-temperature plane, where hydrophobicity h is a property of the solvent that induces collapse (makes η larger). At h_c the transition changes from one that is continuous to one with an order parameter jump as the heteropolymer is cooled in that solvent. Equivalently, at η_c in Fig. 8 the transition changes from continuous to discontinuous.

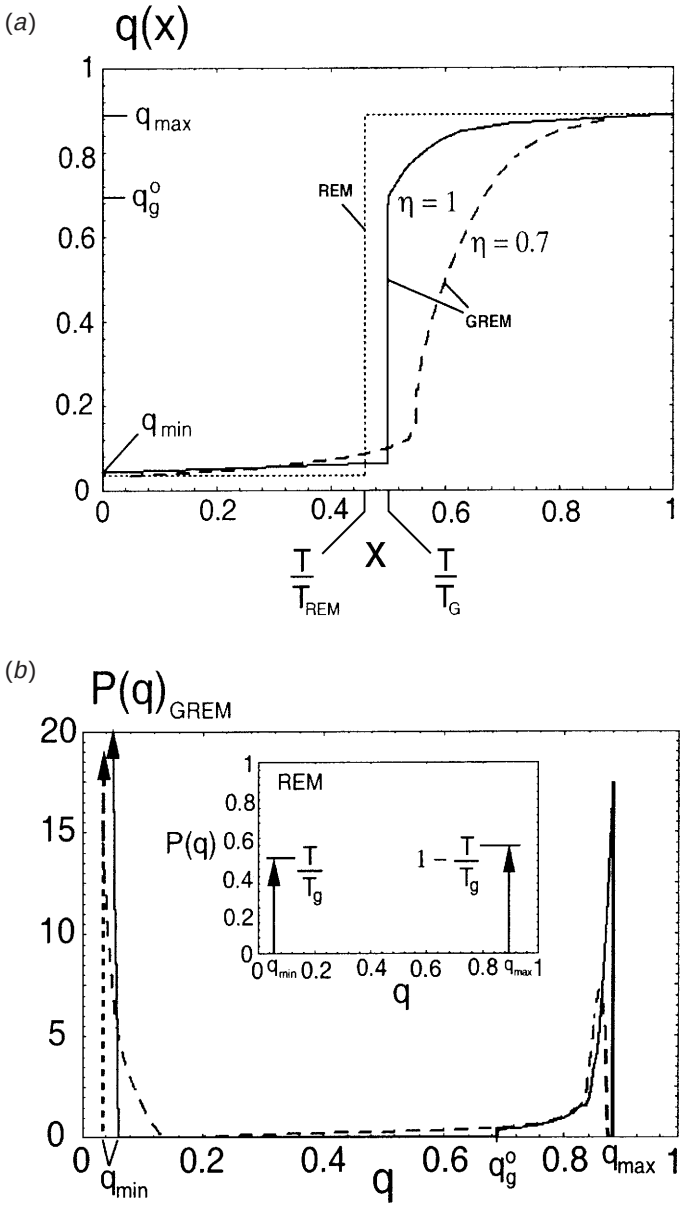

Fig. 10. (*a*) The order parameter $q(x)$ in the analytic theory for a RHP of length $N = 27$, at a temperature of about $(\frac{1}{2})T_G$. - - - -, $q(x)$ in the REM collapsed heteropolymer has a discontinuous jump from q_{min} to q_{max} at $x = T/T_G^{REM}$ where T_G^{REM} is given by Eq. (2.7). ——, For the fully collapsed, correlated RHP, the transition is rounded corresponding to the non-zero entropy of ergodically separated basins. A discrete jump is retained at the glass transition temperature T_G^0, which is within 5–10% of the REM glass temperature. – – –, The partially collapsed RHP has a continuous glass transition, without a discrete jump. The transition from continuous to discontinuous freezing occurs at $\eta_c \approx 0{\cdot}85$. (b) Probability distribution of similarity parameter q in the GREM, and in the REM (inset), at a temperature about $(\frac{1}{2})T_G$. The REM $P(q)$ has two delta functions indicating a single tier of replica-symmetry breaking (see Fig. 7). ——, The collapsed ($\eta = 1$) RHP retains a delta function at q_{min}. The REM spike at q_{max} is spread out into a continuum group of states. - - -, In the partially collapsed ($\eta = 0{\cdot}7$) RHP, there is a finite probability for 2 replicas to have overlaps with all intermediate q values.

4. Basics of configurational diffusion for RHPs and proteins

Understanding configurational diffusion in a protein is essential to predicting folding rates and mechanisms. Specifically, Eq. (I-3.12) for the folding rate contains a prefactor $k_0(D)$ which depends on the configuration diffusion coefficient. To make predictions for protein-folding kinetics or relaxation rates in RHPs, it is necessary to quantitatively understand configurational diffusion for a heteropolymer chain. A protein undergoes state-to-state transitions obeying a master equation: If the probability to occupy state i at time t is $p_i(t)$, then

$$\frac{\mathrm{d}p_i(t)}{\mathrm{d}t} = \sum_j [k_{ji}p_j(t) - k_{ij}p_i(t)]. \tag{4.1}$$

Here k_{ji} is the transition rate from state j to state i.

According to the energy landscape theory (Bryngelson & Wolynes, 1989), protein folding can be seen as a stochastic motion of a few collective coordinates describing protein conformation, on an average thermodynamic potential. To first approximation this motion is Brownian, and the folding time can be computed from diffusive rate theory (Bryngelson & Wolynes, 1989; Socci *et al.* 1996; Klimov & Thirumalai, 1997; Pande & Plaxco, 2001). Then the state-to-state master Eq. (4.1) can be generalized to a master equation along a collective coordinate:

$$\frac{\mathrm{d}p(Q, t)}{\mathrm{d}t} = \sum_{Q'} [k_{Q'Q}p(Q', t) - k_{QQ'}p(Q, t)]. \tag{4.2}$$

Here $p(Q, t)$ is the probability the protein is at similarity Q to the native state, and $k_{Q'Q}$ is the transition rate from Q' to Q, where many states contribute collectively to this rate. Equivalent to a master equation formulation, diffusion along the coordinate Q may be described by a Fokker–Planck eqaution:

$$\frac{\partial p(Q, t)}{\partial t} = \frac{\partial}{\partial Q}\left[D(Q)\left(\frac{\partial p(Q, t)}{\partial Q} + p(Q, t)\frac{\partial(\beta F(Q))}{\partial Q} \right) \right], \tag{4.3}$$

where $D(Q)$ is proportional to the transition rates $k_{Q'Q}$, the proportionality being related to the probability a state to state transition leaves the ensemble of states at Q. In Eq. (4.3), $\beta F(Q)$ is the average thermodynamic potential in units of Boltzmann's constant times the temperature, and is constructed by finding the thermal energy and entropy of the system constrained to be at Q: $F(Q) = E(Q) - TS(Q)$. We pursue this further in Section 5.

In principle the diffusion from state to state may involve many time scales, in which case the validity of Eqs. (4.2) and (4.3) are questionable, in that some information may have been lost on the preojection of all degrees of freedom onto the collective coordinate Q. This is particularly true for a low temperature random heteropolymer chain or poorly designed protein, or for a poorly connected network of conformational states. In these cases, distributions of state-to-state transition rates then translate, upon projection to a reaction coordinate Q, to a spectrum of diffusion coefficients, i.e. the diffusion coefficient then depends on the frequency of the mode looked at, $D(Q) \to D(Q, \omega)$. Similar treatments of diffusion with a distribution of trapping times lead to what are known as fractional Fokker–Planck equations (Metzler & Klafter, 2000).

Equivalently, we can generalize the master equation of Eq. (4.2) to allow for history dependence in the transition rate, i.e. the probability to move from Q to Q' is a function of

the time spent in the states at Q. This non-Markovian behavior is to account for the numerous timescales of diffusion in principle present in the problem. Define the rate for a system which arrived at Q at time zero to move to Q' between time t and $t+\mathrm{d}t$ to be $k_{Q,Q'}(t)\mathrm{d}t$. Then

$$\frac{\mathrm{d}p(Q,t)}{\mathrm{d}t} = \sum_{Q'=0}^{1} \int_0^t \mathrm{d}t' [k_{Q'Q}(t-t')p(Q',t') - k_{QQ'}(t-t')p(Q,t')]. \tag{4.4}$$

is the generalized master equation governing transitions, and the corresponding Fokker–Planck equation governing the diffusion is:

$$\omega P(Q,\omega) - P(Q,t=0) = \frac{\partial}{\partial Q}\left[D(Q,\omega,T)\left(P(Q,\omega)\frac{\partial}{\partial Q}\frac{F(Q,\omega,T)}{T} + \frac{\partial}{\partial Q}P(Q,\omega)\right)\right], \tag{4.5}$$

where $F(Q,\omega,T) = F(Q,T) + T\ln(D(Q,\omega,T)/D(Q,0,T))$, i.e. the frequency-dependent effective potential is related to both the bare potential and the diffusion coefficient. The statistics of transition rates enters into the calculation of the diffusion coefficient $D(Q,\omega,t)$ in Eq. (4.5).

The fact that the annealed approximation is good for proteins as discussed in Section I-5 supports the description that there is not a wide distribution of transition rates between states. Conversely, individual untrapping events and a wide distribution of barrier heights would govern the relaxation dynamics of a poorly designed, frustrated system. States within the stratum Q would be slow to interconvert, and many exponentials would contribute to the rate of diffusion. This would correspond to a wide spectrum of values for the diffusion coefficient, yielding strongly non-Markovian behavior. In extreme cases near the T_G, diffusion may even have to be treated at the level of individual trap escapes, at least for a finite-sized system. However for systems which have a folding temperature, T_F, sufficiently larger than T_G, and when we are considering dynamics at temperatures T well above T_G, Markovian diffusion along the coordinate Q should tend to be a good approximation. This is shown to be the case in Section 6. On the other hand, in the limit when interconversion times between partially native structures are slow compared to the barrier crossing timescale, a protein will begin to exhibit kinetic partitioning, in that fractions of an ensemble of proteins fold with different rates (Guo & Thirumalai, 1995). This behavior is seen for example in hen lysozyme, which shows intermediates corresponding to multi-domain folding, and correspondingly multi-exponential kinetics (Radford *et al.* 1992). In these cases, it is worthwhile to explicitly introduce another order parameter in addition to say Q, which can distinguish between intermediates (Dobson *et al.* 1998). It will be interesting to investigate how such features may arise from the interplay between the energy function and the connectivity of the network of conformational states resulting from the native structure.

As discussed in Section I-3, there is a modest residual free-energy barrier in the potential $F(Q,T)$ in Eq. (4.3). The solution for the mean first passage time to cross the barrier (and thus fold) is (Szabo *et al.* 1980; Deutsch, 1980; Bryngelson & Wolynes, 1989)

$$\bar{\tau}_F = \int_{Q_U \simeq 0}^{Q_F \simeq 1} \mathrm{d}Q \int_0^Q \mathrm{d}Q' \frac{1}{D(Q)} \mathrm{e}^{\beta[F(Q)-F(Q')]}. \tag{4.6}$$

Equation (4.6) can be rewritten in a simpler form by letting $G(Q) \equiv F(Q) - TR(Q)$, where

$R(Q) \equiv \ln(D(Q)/D_u)$ and D_u is the diffusion coefficient in the unfolded state. Then one can perform saddle-point expansions around the unfolded free-energy minimum, and the maximum Q^* of $G(Q)$ to obtain

$$\bar{\tau}_F = \frac{2_\pi T}{D_u \omega_u \omega^*} e^{\beta[G(Q^*)-F(Q_U)]} \tag{4.7a}$$

$$k_F = \bar{\tau}_F^{-1} = \frac{\omega_u \omega^*}{2\pi\zeta(Q^*)} e^{-\beta[F(Q^*)-F(Q_U)]}, \tag{4.7b}$$

which is the well-known Kramers law for barrier crossing by activated diffusion in the spatial diffusion limit (Kramers, 1940; Hanggi *et al*. 1990). Here the rate prefactor is proportional to the curvature of the free energy in the unfolded state as well as to the curvature of $G(Q)$ near Q^*, and inversely proportional to the friction kernel $\zeta(Q^*)$ at the position of the maximum. The rate is exponentially suppressed by the free-energy difference between Q^* and Q_u.

Note that Q^* is in general not equal to the position of the barrier peak in the free energy. Typically, the barrier peak is taken as the position of the transition state because it is assumed the diffusion coefficient does not vary too strongly with Q. We examine the effects of a Q-dependent diffusion coefficient in Appendix C, and find that in summary, a Q-dependent diffusion coefficient may significantly affect the transition state ensemble without significantly affecting the rate (see Appendix C).

Other reaction coordinates for folding or diffusion may be chosen besides Q, e.g. the fraction of native or similar dihedral angles. For these other coordinates, the position and height of the barrier will in general differ from $\Delta F(Q^{\ddagger})$. Of course the rate must be same, so the prefactor will also be different. We choose Q for the analysis because the energetics are easy to calculate, and the entropics can be calculated as in Section 2.4. Then it is in principle straightforward to quantify the mean escape time $\langle\tau\rangle$ and thermodynamic potential $F(Q)$ in terms of this parameter.

In the limit of the most minimally frustrated protein, a Gō model protein (Ueda *et al*. 1975), Rouse–Zimm times govern state to state diffusion. Transitions between states are fast, and are determined by properties of the polymer chain and native structure. For proteins not so strongly funneled, configurational diffusion is colored by escape from numerous local energetic traps which pock-mark the energy landscape. Trapping is facilitated by the low energy of a given configuration, and opposed by the entropic driving force of numerous dissimilar structures. As mentioned earlier, the diffusion coefficient and the state-to-state transition rates are not independent quantities. By equating the master equation description in Eq. (4.4) to a description in terms of the Fokker–Planck equation [Eq. (4.5)], one obtains the diffusion coefficient in terms of the rate (or time) between transitions (Kenkre *et al*. 1973; Bryngelson & Wolynes, 1989). The general result is given in Section 6. Taking the zero-frequency (long-time) limit of Eq. (6.10) gives

$$D \cong \frac{\lambda}{\langle\tau\rangle}, \tag{4.8}$$

where λ sets a 'distance' scale of local moves on the landscape. The strategy for estimating folding rates then reduces to finding the mean escape time $\langle\tau\rangle$ in Eq. (4.8) thus determining $\zeta = k_B T/D$ in Eq. (4.7*b*), and determining the reaction surface or thermodynamic potential $F(Q)$ in Eq. (4.7*b*).

At the other extreme from the Gō model, we can consider a RHP or very poorly designed protein near the T_G. We can make some statements about the structure of the distribution of relaxation times in such a material as follows. First we may postulate an Arrhenius law for escape from individual states. For a state of energy E, the escape time is

$$\tau = \tau_0 e^{(E^*-E)/T}, \tag{4.9}$$

where E^* is an activation energy, assumed fixed.

Using Eq. (4.9), we can explain the initial time dependence of the energy for a RHP system which has undergone a sudden temperature jump from $T_0 = \infty$ to $T \lesssim T_G$ (Shakhnovich & Gutin, 1989c). For such a system, at time τ, all states with energies with $E' > E(\tau)$ [where $E(\tau) = E^* - T\ln(\tau/\tau_0)$ is the inverse of Eq. (4.9)] have relaxed to their equilibrium Boltzmann distribution, while all states below $E(\tau)$ are nearly unpopulated (since the initial temperature was ∞). The average energy at time τ is then

$$\bar{E}(\tau) = \frac{\int_{E(\tau)}^{\infty} dE\, En(E)e^{-\beta E}}{\int_{E(\tau)}^{\infty} dE\, n(E)e^{-\beta E}} = -\frac{d}{d\beta}\ln\int_{E(\tau)}^{\infty} dE\, e^{-E^2/2\Delta^2-\beta E}$$

$$= -\beta\Delta^2 + \sqrt{2}\pi\Delta\frac{e^{-X(\beta)^2}}{\mathrm{erfc}(X(\beta))}, \tag{4.10}$$

where β is the reciprocal final temperature, and $X(\beta) = (\frac{1}{2}\Delta)(\beta\Delta^2 + E(\tau))$. Because $E(\tau)$ is always above the ground state energy, and $\beta\Delta^2$ is always larger than the magnitude of the ground-state energy (since $\beta > 1/T_G$), X is positive and reasonably large, until the equilibrating energies are down in the discrete part of the spectrum. Then one can approximate the complementary error function in Eq. (4.10) to yield

$$\bar{E}(\tau) = E(\tau) = E^* - T\ln\left(\frac{\tau}{\tau_0}\right) \tag{4.11}$$

so that the thermal energy relaxes logarithmically with elapsed time, and proportional to the final temperature.

To further investigate the dynamics when $T < T_G$, we can expand the density of states near the tail end of the spectrum shown in Fig. 1 (i.e. around E_{GS}) as

$$P(E) \simeq e^{E/T_G}, \tag{4.12}$$

and then obtain from Eq. (4.9) a power law distribution of transition times:

$$P(\tau) = \frac{P(E(\tau))}{|d\tau/dE|} = A\tau^{-(1-x)}, \tag{4.13}$$

where $x = T/T_G \lesssim 1$. Power law distributions of transition times typically lead to stretched exponential relaxation functions (Shlesinger & Montroll, 1984). To see this, let $N(t)$ be the number of systems in an ensemble which have not yet made a transition in time τ which would equilibrate the system. Then $\dot{N}(t) = -k(t)N(t)$ where $k(t)$ is the time-dependent rate coefficient. We let $N(t)/N_0$ serve as the relaxation function $\phi(t)$

$$\phi(t) = \frac{N(t)}{N_0} = \exp\left(-\int_0^t dt\, k(t)\right). \tag{4.14}$$

The rate coefficient at time t is proportional to the time rate of change of the number of distinct states $\mathbf{\Omega}(t)$ visited within time t (Shlesinger & Montroll, 1984): $k(t) = \mathrm{d}\mathbf{\Omega}/\mathrm{d}t$. The number of distinct states visited in time t in a d-dimensional walk scales like the time elapsed over the mean time between steps, raised to a power γ which depends on the dimensionality of the walk (the connectivity of the state space for the heteropolymer example; for $d = 3$, $\gamma = 1$, for $d = 1$, $\gamma = \frac{1}{2}$)

$$\mathbf{\Omega}(t) = \mathcal{A}' \left(\frac{t}{\langle t \rangle} \right)^{\gamma}. \tag{4.15}$$

For the Levy waiting distribution in Eq. (4.13), the mean time $\langle \tau \rangle$ in Eq. (4.15) diverges slower than the time waited, as τ^{1-x}, so $\mathbf{\Omega}(\tau) \sim \tau^{x\gamma}$ and the relaxation function

$$\phi(\tau) = \mathrm{e}^{-\mathbf{\Omega}(\tau)} = \exp(-\mathcal{A}\tau^{\gamma T/T_{\mathrm{G}}}) \tag{4.16}$$

is stretched exponential.

For a finite-sized system such as a model protein below T_{G}, relaxation to $Q = 1$ starting from $Q \simeq 0$ is dominated by escape from one or a few states with RHP ground-state energies. The smallest barriers with sequence-dependent energies E^* are the rate-limiting steps and dominate the relaxation rate, which turns over to an Arrhenius law for such a finite-sized system.

$$k(T) \approx k_0 \mathrm{e}^{-(E^* - E_{\mathrm{GS}})/T}. \tag{4.17}$$

4.1 Kinetics on a correlated energy landscape

The strategy we follow is to first find $\langle \tau(T) \rangle$ for a RHP (Wang *et al*. 1997). The quantities that enter are the entropy S which drives trap escape, the temperature T over T_{G}, and lastly a nonlinearity parameter which characterizes the residual barrier height for trap escape. In Wang *et al*. (1997), this was taken to come from a nonlinear entropy function. However nonlinearity may also arise from cooperative energetic effects to yield the same result. Once $\langle \tau(T) \rangle$ is obtained for a RHP, we may substitute $S \to S(Q)$, and $T_{\mathrm{G}} \to T_{\mathrm{G}}(Q)$ to estimate the diffusion coefficient $D(Q, T) = \lambda / \langle \tau(Q, T) \rangle$ and thus friction $\zeta(Q, T) = T/D(Q, T)$ in Eq. (4.7*b*) for protein folding. Escape from traps determines the effective diffusion coefficient (*versus* Q) for flow of an ensemble of unfolded protein structures towards the folded state.

With a knowledge of the number of states which exist on the landscapes a distance q from a given state i, i.e. $S(q)$, and their energetic correlations to state i of energy E_i, we may calculate a free-energy profile about a state i, with the similarity measure q now acting as a reaction coordinate for escape from the basin centered around the state of energy E_i.

The statistics of the energies of states on the landscape is treated by using Eqs. (3.3) and (3.4). The probability of there being a state of energy E at similarity q to a given state i, given i has energy E_i, is

$$P_q(E \mid E_i) = \frac{P_q(E, E_i)}{P(E_i)} \approx \exp\left[-\frac{(E - q^p E_i)^2}{2M(1 - q^{2p})b^2} \right]. \tag{4.18}$$

Note that when $q \to 1$, $P_q(E \mid E_i) \to \delta(E - E_i)$, and when $q \to 0$, the states are uncorrelated, and $P_q(E \mid E_i) \to P(E)$. This equation is generalized in Section 5 to include a different energetic variance in the reference configuration i, which may be relevant for proteins where native energetic variance may be reduced. When the variance in the reference state is set to

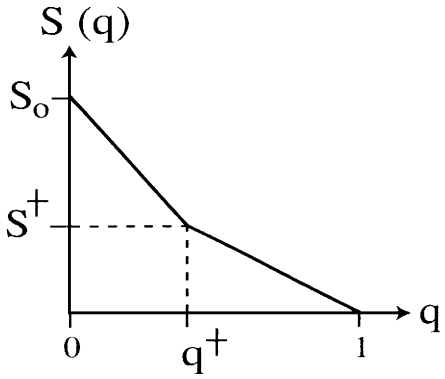

Fig. 11. Bi-linear form of $S(q)$ used in the GREM calculation of mean escape time. The bilinear form is a good approximation since contacts formed initially for a weakly constrained polymer cost more entropy than for a strongly constrained one at high q. The entropy has a discontinuity in slope at $q = q^{\mp}$, where the fraction of remaining entropy is $S(q^{\mp})/S_0 \equiv \tilde{s}^{\mp}$.

zero, the denominator of the exponent in Eq. (4.18) is replaced by $2M(1-q^p)b^2$. This is the result also obtained by taking a saddle-point solution on an ultrametric tree of states (Wang *et al*. 1997), as well as when the set of all contact energies in the native or reference state is known and specified. Diffusion on the landscape was treated for both cases in Wang *et al*. (1997).

For two-body interactions $p = 1$, and the mean number of states of energy E having similarity q to i is

$$\bar{n}_q(E|E_i) = e^{S(q)}P_q(E \mid E_i) = \exp\left[S(q) - \frac{(E-qE_i)^2}{2M(1-q)b^2} \right], \tag{4.19}$$

where we have taken the saddle-point solution mentioned above. $S(q)$ is the log total number of conformational states at q. This function was treated in Section 2.4, and we will use this analysis for the thermodynamic potential for folding $F(Q)$. However in treating the diffusion coefficient we take a simple bi-linear fit for the entropy shown in Fig. 11, to obtain simple, analytic expressions for the mean escape time. The shape of the escape potential $F(q|E_i)$ fluctuates from trap to trap depending on the energy E_i if conformational state i, so heuristically we will assume the simple bi-linear form of the entropy in Fig. 11 to capture the gross features of the escape process, and expedite the calculation. Following the reasoning used to obtain Eq. (2.6*c*) from Eq. (2.5), we can obtain the free-energy profile:

$$F(q|E_i) = qE_i - TS(q) - \frac{1}{2T}M(1-q)b^2. \tag{4.20}$$

A free-energy barrier for escape can be calculated from Eq. (4.20) for each state i of energy E_i (Wang *et al*. 1997) (see Fig. 12). The escape time $\tau(E_i, T)$ from a given state with energy E_i is calculated from Eq. (4.20) by an Arrhenius law:

$$\tau(E_i, T) = \tau_0 \exp[(F(E_i, T, q^{\mp}) - F(E_i, T, 1))/T], \tag{4.21}$$

where τ_0 is the timescale for local motions along q. Trap escape is treated as a mini-unfolding event from trap conformation i.

The distribution of escape times at temperature T, $P(\tau, T)$, is calculated from

$$P(\tau, T) = \int dE_i\, P(E_i, T)\delta[\tau - \tau(E_i, T)], \tag{4.22}$$

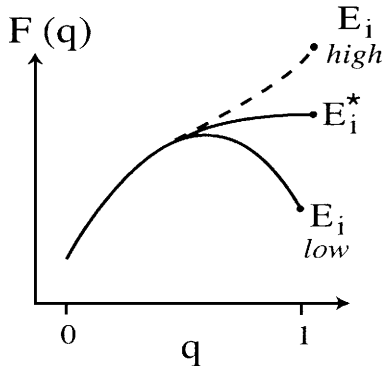

Fig. 12. At a given temperature, low-energy states have a barrier for escape, while states of higher energy have downhill free-energy profiles. E_i^* is the critical energy for downhill escape. The temperature where the thermal energy equals E_i^* is roughly the dynamic glass temperature.

where $P(E_i, T)$ is the probability an occupied state has energy E_i at temperature T:

$$P(E_i, T) \approx \mathrm{e}^{-S(\tilde{E}-1/\tilde{T})^2}, \tag{4.23}$$

where $\tilde{E} = E/|E_{\mathrm{GS}}|$ is the energy in units of the ground-state energy $\Delta\sqrt{2S}$, and $\tilde{T} = T/T_{\mathrm{G}}$ is the temperature in units of the glass temperature $\Delta/\sqrt{2S}$. Integrating Eq. (4.22) yields

$$P(\tau, T) = w_{\mathrm{BL}}(T)\delta(\tau-\tau_0) + w_{\mathrm{B}}(T)\frac{A}{\tau}\exp[-\alpha\ln^2(\tau/\tau')]. \tag{4.24}$$

The first term in the distribution of Eq. (4.24) corresponds to the collection of states at temperature T with downhill free-energy (barrier-less) profiles, and thus escape time $\sim \tau_0$. The second term corresponds to the lower energy states with free-energy barriers to escape, which have a log-normal distribution of escape times. The time $\tau'(T)$ is a temperature-dependent timescale. Each piece of the distribution has a temperature-dependent weight; $w_{\mathrm{B}}(T)$ increases and $w_{\mathrm{BL}}(T)$ decreases as temperature is lowered.

The mean escape time $\langle\tau(T)\rangle$ is just the first moment of the distribution:

$$\langle\tau(T)\rangle = \int_{\tau_0}^{\infty} \mathrm{d}\tau\, \tau P(\tau, T), \tag{4.25}$$

and has the form (see Fig. 13)

$$\langle\tau(T)\rangle \approx \begin{cases} \tau_0 & \text{for } T_{\mathrm{A}} < T \\ \tau_0 \exp[S_{\mathrm{Lev}}^{\mathrm{G}} - S(2-q^{\ddagger})(1-(1/T))^2] & \text{for } T_{\mathrm{G}} < T < T_{\mathrm{A}} \\ \tau_0 \exp(S_{\mathrm{Lev}}^{\mathrm{G}}) & \text{for } T < T_{\mathrm{G}}, \end{cases} \tag{4.26}$$

where $S_{\mathrm{Lev}}^{\mathrm{G}} = S(1-q^{\ddagger}-\tilde{s}^{\ddagger})$ is the reduced Levinthal entropy in the kinetic GREM, and

$$T_{\mathrm{A}} = \frac{T_{\mathrm{G}}}{1+\tilde{s}^{\ddagger}}[2-q^{\ddagger}+\sqrt{(2-q^{\ddagger})(1-q^{\ddagger}-\tilde{s}^{\ddagger})}] \tag{4.27}$$

is a temperature above which escape barriers disappear, i.e. above T_{A} the free-energy profile for thermally occupied states is downhill (Wang *et al.* 1997). However, below this temperature, dynamics become activated for a large fraction of the states, and one obtains a modified form of the Ferry law often seen in treatment of glass dynamics [see Eq. (4.28)

below]. It can be seen from Eq. (4.27) that when the configurational entropy is purely linear ($\tilde{s}^{\ddagger} = 1 - q^{\ddagger}$), $T_A \to T_G$, so that the kinetics are unactivated all the way down until the thermodynamic glass transition temperature – entropic gains always compensate energetic losses, leaving no residual free-energy barriers.

The mean diffusion time is Eq. (4.26) is plotted as a function of temperature in Fig. 13. The diffusion coefficient is essentially the reciprocal of Eq. (4.26). The numerical values of the escape time for the correlated landscape are in much better agreement (than the REM) with the values inferred from lattice simulations.

It is worthwhile comparing Eqs. (4.26) and (4.27) with the results for an uncorrelated landscape (Bryngelson & Wolynes, 1989):

$$\langle \tau(T) \rangle_{\mathrm{REM}} \approx \begin{cases} \tau_0 \exp(2S/T^2) & \text{for } 2T_G < T \\ \tau_0 \exp[S - 2S(1-(1/T))^2 & \text{for } T_G < T < 2T_G \\ \tau_0 \exp(S) & \text{for } T < T_G, \end{cases} \tag{4.28}$$

A more detailed analysis (Wang *et al*. 1997) obtains Eq. (4.28) as a limiting case of the GREM result [Eq. (4.26)]. However we can see much of that limit here, when we let $\tilde{s}^{\ddagger}$ and $q^{\ddagger} \to 0$. Then the free-energy landscape is highly cratered, and there is no entropic gain until all energetic bonds are broken; the lower two temperature regimes in Eq. (4.26) reduce to those of Eq. (4.28), and $T_A \to (2+\sqrt{2})T_G$. The Levinthal search at T_G involves the total entropy in the REM limit. A more careful analysis recovers the REM crossover temperature $T_A \to 2T_G$, as well as the Ferry law behavior of the higher temperature regime.

A physical interpretation of T_A is the temperature when the energies of thermally occupied states have downhill free-energy profiles. In the REM limit there is always a barrier to escape from a thermally occupied state. For bulk systems (lim $N \to \infty$), $\tilde{s}^{\ddagger} \to \approx 0.3$, $q^{\ddagger} \to \approx 0.18$, and $T_A \to \approx 2.1\ T_G$ (Wang *et al*. 1997).

One may also study the landscape statistics from many-body Hamiltonians, as in Eqs. (3.2) and (4.18). For these models the landscape becomes more golf-course-like, because energetic correlations become extremely short range in structural similarity space or q. For p-contact interactions, $T_A \to \infty$ as $p^{\frac{1}{2}}$ in the limit of large p. The dynamics are always activated as in the REM – there are no energetic correlations between the states until they are nearly identical.

Finally, we mention that analyses of kinetics on landscapes having global kinetic moves, so that all states are kinetically connected, have already been carried out (Saven *et al*. 1994; Wang *et al*. 1996).

5. Thermodynamics and kinetics of protein folding

5.1 A protein Hamiltonian with cooperative interactions

As mentioned in Section I-6, one can quantitatively describe a funnel with a statistical Hamiltonian having the form of Eq. (I-6.3):

$$\mathscr{H}_P\{\Delta_i\} = \sum_{i<j} [\epsilon_{ij}^N \Delta_{ij} \Delta_{ij}^N + \epsilon_{ij}(1 - \Delta_{ij}^N)\Delta_{ij}],$$

with pair-interaction contact energies chosen from Eq. (I-6.4). However, the hydrophobic force driving folding is believed to be a cooperative, many-body effect. This prompts us to investigate the effects of cooperativity within the context of the energy landscape theory. To

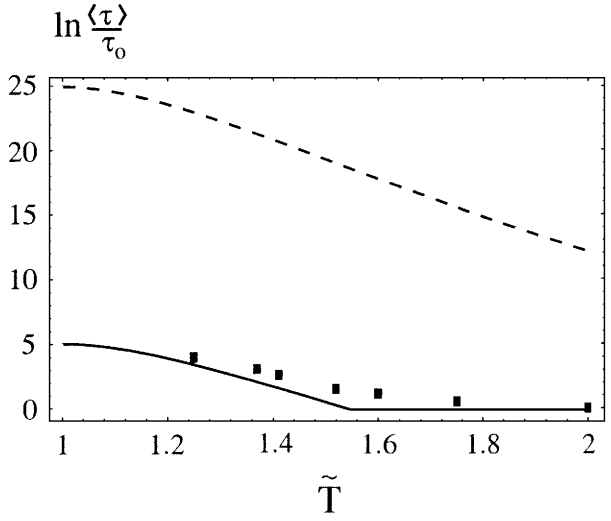

Fig. 13. Logarithm of the mean escape time for the correlated landscape model of a 27-mer random heteropolymer *versus* temperature in units of T_G. ——, The correlated landscape [Eq. (4.26)] with $q^{\neq} = \tilde{s}^{\neq} = 0{\cdot}4$, $S = 0{\cdot}9 \times 27$, $T_A \simeq 1{\cdot}55$. - - -, The REM (uncorrelated) model, Eq. (4.28). The data-points are adapted from measurements of the diffusion coefficient from simulations on a specific 3-letter sequence 27-mer (Socci *et al.* 1996), with the data at $T = 2\ T_G$ normalized to τ_0. The dynamic glass transition at T_A is apparently rounded due to the finite size of the system ($N = 27$).

generalize this protein Hamiltonian to p-contact interactions, we can follow the reasoning leading to Eqs. (3.1) and (3.2) to give

$$\mathscr{H}_P\{\Delta_i\} = \sum_{1 \leqslant i_1 < i_2, \ldots, < i_p \leqslant M} \left\{ \epsilon^N_{i_1, i_2, \ldots, i_p} \left(\prod_{i=i_1}^{i_p} \Delta_i^N \right) \left(\prod_{i=i_1}^{i_p} \Delta_i \right) + \epsilon_{i_1, i_2, \ldots, i_p} \left[1 - \left(\prod_{i=i_1}^{i_p} \Delta_i^N \right) \right] \left(\prod_{i=i_1}^{i_p} \Delta_i \right) \right\}, \tag{5.1}$$

where the coupling energies $\epsilon^N_{i_1, i_2, \ldots, i_p}$ and $\epsilon_{i_1, i_2, \ldots, i_p}$ are chosen from distributions of different mean, and possibly variance. Equation (5.1) is an energy function with purely cooperative interactions. Two points are worth mentioning here. One can straightforwardly generalize the Hamiltonian to include a heirarchy of terms representing interactions with various levels of cooperatively. Another interesting topic is the issue of the most likely configurations of native contacts given Eq. (5.1). For example the p contacts may most likely belong to spatially contiguous clusters of residues, as in capillarity models.

5.2 Variance of native contact energies

The variance in coupling energies in the native structure need not be the same as the variance over structures whose energy is unconstrained. That is, the low energy of the native structure can reduce the energetic variance contact to contact. To illustrate this, let the allowed contact energies in a $p = 1$ Hamiltonian have two values, b and $-b$. Then the distribution of coupling energies is

$$P(\epsilon) = \tfrac{1}{2}\delta(\epsilon + b) + \tfrac{1}{2}\delta(\epsilon - b). \tag{5.2}$$

This distribution has a mean of zero, so we have taken energies relative to the mean energy here. The mean energy per contact $\bar{\epsilon}(E)$ in a structure of energy E is $(1/M)\Sigma_i \epsilon_i = E/M$, where we have labeled each of the M contacts by a single index i. This number must be between $-b$ and b, and will tend to $-b$ as $E \to -Mb$. The variance per native contact $\overline{\delta\epsilon^2}$ is $\overline{\epsilon^2} - \bar{\epsilon}^2 = b^2 - E^2/M^2$. When $E = 0$ (or E is the average energy), $\overline{\delta\epsilon^2} = b^2$, but when E is large and negative, the variance is reduced. When $E = -Mb$, $\overline{\delta\epsilon^2} = 0$. For native-like energies a factor γ below the random heteropolymer ground state energy, i.e. $E = -\gamma Mb\sqrt{2s_0/z}$ with $\gamma \geqslant 1$,

$$\overline{\delta\epsilon^2} = b^2 \left(1 - \gamma^2 \frac{2s_0}{z} \right), \tag{5.3}$$

so the native variance is appreciable only when $\gamma^2 2s_0/z < 1$. Taking a concrete model such as a lattice model for folding, typical collapsed conformational entropies have values of $s_0 \cong \ln(6/e)$. So for there to be any native variance, $z \gtrsim 1.6\,\gamma^2$. The larger the entropy s_0, say if other models are considered, the more stringent the lower bound on the number of neighbors per monomer. The number of neighbors per monomer z for a collapsed 'Hamiltonian' walk on a 3D cubic lattice is $\cong 2 - 3N^{-\frac{1}{3}}$, thus for any appreciable native variance $N \gtrsim 3^3/(2 - 1.6\,\gamma^2)^3$. For $\gamma = 1$, $N \gtrsim 420$! That is, for system sizes involved in simulations, there is essentially no variance in the native structure. Real proteins have a large 'two-letter' component to their energy functions, loosely corresponding to hydrophobic–hydrophobic and hydrophobic–hydrophilic interactions. The above argument implies that there should be a significant reduction in the variance of the interaction energies in the native structure, compared to generic collapsed structures.

In principle the variance is then a function of E, which for funneled landscapes is a function of Q, so there is some reduction in variance as folding progresses. Residual variance may of course be present in real proteins for other reasons such as assisting function.

In general we may find the native variance $\langle \delta\epsilon_i^2 \rangle$ from $\langle \epsilon_i^2 \rangle - \langle \epsilon_i \rangle^2$, where

$$\langle \epsilon_i^p \rangle = \frac{\int \prod_j P_{\mathrm{N}}(\epsilon_j) \epsilon_i^p \delta \left(\sum_j \epsilon_j - E_{\mathrm{N}} \right)}{\int \prod_j P_{\mathrm{N}}(\epsilon_j) \delta \left(\sum_j \epsilon_j - E_{\mathrm{N}} \right)}. \tag{5.4}$$

Another interesting special case is when the interaction energies are chosen from a Gaussian distribution of variance b, rather than the binary distribution of contact energies in Eq. (5.2). In this case the native variance b_{N} is essentially not reduced: $b_{\mathrm{N}}^2 \equiv \langle \delta\epsilon_i^2 \rangle = b^2(1 - 1/M)$ regardless of E, hence for large enough polymers $b_{\mathrm{N}} \equiv \delta\epsilon_{\mathrm{N}} = b$. This is because the distribution of interaction energies is a continuous (non-discrete) function. For distributions of interaction energies with many possible values, we still expect to have some variance in the energies of native stabilizing interactions. We take up this issue in Section 7.

5.3 Thermodynamics of protein folding

The fact that proteins are minimally-frustrated motivates one to let the coupling energies $\epsilon^{\mathrm{N}}_{i_1, i_2, \ldots, i_p}$ and $\epsilon_{i_1, i_2, \ldots, i_p}$ in Eq. (5.1) be chosen from distributions of different mean and variance. We choose effective Gaussian distributions for simplicity. The probability of there

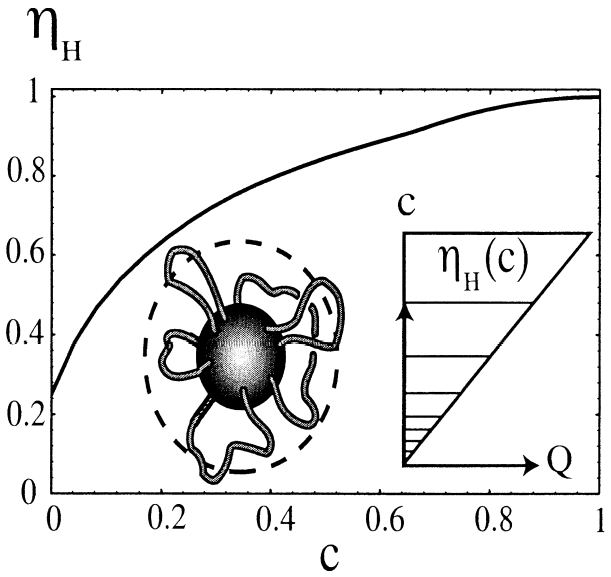

Fig. 14. The halo density η_H as a function of the fraction of the total contacts c. *Left inset*: the partially native protein can be pictured as a frozen, compact, native core surrounded by a halo of unfolded polymer of variable density (Plotkin *et al.* 1997). *Right inset*: a surface contour plot of $\eta_H(Q, c)$ in the model. The halo density $\eta_H(c)$ is a function only of the total number of contacts present, irrespective of whether those contacts are native or not.

being a state of energy E at similarity Q to the native structure of energy E_N, is then modified from Eq. (4.18) to:

$$P_Q(E \mid E_N) = \frac{P_Q(E, E_N)}{P(E_N)} \approx \exp\left[-\frac{(E - Q^p E_N)^2}{2M(1-Q^p)(b^2 + Q^p b_N^2)} \right]. \tag{5.5}$$

Note that when $Q \to 1$, $P_Q(E \mid E_N) \to \delta(E - E_N)$, and when $Q \to 0$, or $p \to \infty$, the states become uncorrelated and $P_Q(E \mid E_N) \to P(E)$. Moreover, when the native variance $b_N^2 \to b^2$, Eq. (4.18) is recovered, and when $b_N^2 \to 0$, the saddle-point solution of the GREM is recovered. Again the above arguments indicate it is likely b_N^2 is reduced from b^2. When $p = 1$, the landscape statistics of a two-body Hamiltonian are recovered. The more many-body the Hamiltonian is, the more de-correlated states of a given structural similarity are.

The a priori assertion of the existence of a low-energy state, plus the energetic correlations which exist due to structural similarity, and the locality of interactions (p is not large), induce a global funnel topography to the landscape, when E_N is considerably lower than the RHP ground state.[2] The funnel topography induced yields a much larger stability of the native structure against sequence mutations or environmental perturbations, as described in Section I-3.

Concurrent collapse with folding may be important to consider when the protein is strongly funneled or has weak non-specific attraction. In these cases unfolding is loosely analogous to sublimation. To account for collapse as well as native similarity, we wish to

[2] The minimal frustration of the native structure is encoded into the sequence in a manner similar to the hidden order in unfrustrated spin-glass models such as the Mattis model (Mézard *et al.* 1986). For such a system a gauge transformation to an appropriate spin conformation reduces the Hamiltonian to an unfrustrated ferromagnet. The 'gauge transformation' to the least frustrated structure for a given sequence is considerably more complex.

stratify the energy landscape with respect to both the fraction of *native* contacts Q, and the fraction of *total* contacts c (both native and non-native). Then the results may directly be compared with existing simulations (Socci *et al.* 1998), for which Q and c are convenient parameterizations. However the theory of configurational entropy described in Section 2.4 was characterized in terms of packing fraction η, so a theory of collapse must be introduced to find the polymer density η ($0 < \eta < 1$) as a function of Q and c. This functional dependence enters through the configurational entropy, $S(Q, c) = S(Q, \eta(Q, c))$.

A partially native protein consists of a dense native core with $\eta_C = 1$ surrounded by a less dense halo region $\eta_H \leqslant 1$ (see Fig. 14). As Q increases, the size of the native core increases, and the amount of polymer in the halo decreases. The number of loops decorating the core, their average length, and the average length of the two dangling ends of the polymer can be taken from the high-Q analysis for a strongly constrained polymer in Section 2.4. This results in a theory for the packing fraction η in terms of Q and c: $\eta(Q, c)$ (Plotkin *et al.* 1997).

Once the polymer issues are under control, the thermodynamics of the landscape may be deduced as in Eqs. (4.19) and (4.20). The mean number of states $\bar{n}(E|E_N, Q, c)$ having energy E, similarity Q, and density c on the minimally frustrated landscape is $\exp(S(Q, c))P(E|E_N, Q, c)$. When the mean number of states is $\gg 1$, the microcanonical entropy $S(E|Q, c)$ is obtained by taking the log of $\bar{n}(E|E_N, Q, c)$, and the thermodynamics in the canonical ensemble obtained through the Legendre transform $\partial S/\partial E = T^{-1}$ as before. This yields:

$$\frac{E}{M}(T, Q, c|E_N) = c^p\bar{\epsilon} + Q^p\epsilon_N - \frac{c^p}{T}(1-Q^p)(b^2 + Q^p b_N^2) \tag{5.6a}$$

$$\frac{S}{M}(T, Q, c|E_N) = \frac{s(Q, c)}{\chi} - \frac{c^p}{2T^2}(1-Q^p)(b^2 + Q^p b_N^2) \tag{5.6b}$$

$$\frac{F}{M}(T, Q, c|E_N) = c^p\bar{\epsilon} + Q^p\epsilon_N - T\frac{s(Q, c)}{\chi} - \frac{c^p}{2T}(1-Q^p)(b^2 + Q^p b_N^2). \tag{5.6c}$$

A larger number of total contacts c lowers the energy and thus the free energy due to the first 'homopolymer' term on the right-hand side of Eqs. (5.6*a*) and (5.6*c*), assuming $\bar{\epsilon} < 0$ as is typically the case. Cooperative p-contact interactions are introduced for this homopolymer force as well here. The last term on the right-hand side quantifies the roughness of the landscape. This term comes from the non-native parts of the protein outside the native core, and induces a free energy bias towards states with many non-native contacts (c large and Q small). The protein can find itself in statistically low-energy non-native states due to the random nature of the interactions. The term $Q^p\epsilon_N$ on the right-hand side of Eqs. (5.6*a*) and (5.6*c*) embodies the slope of the funnel, inducing a free energetic bias towards structures with greater nativeness. The third, entropic term in Eq. (5.6*c*) gives a bias towards expanded states with small Q and c, where the conformational entropy is largest. The larger p is, the more native-like structures must be to be low in energy.

When the Hamiltonian consists of pair interactions, $p = 1$. When we can neglect native energetic variance, $b_N = 0$. For these cases, Eq. (5.6*c*) becomes (Plotkin *et al.* 1997) (recall $M = N\chi$):

$$\frac{F}{N}(T, Q, c|E_N) = c\chi\bar{\epsilon} + Q\chi\epsilon_N - (1-Q)\frac{c\chi b^2}{2T} - Ts(Q, c), \tag{5.7}$$

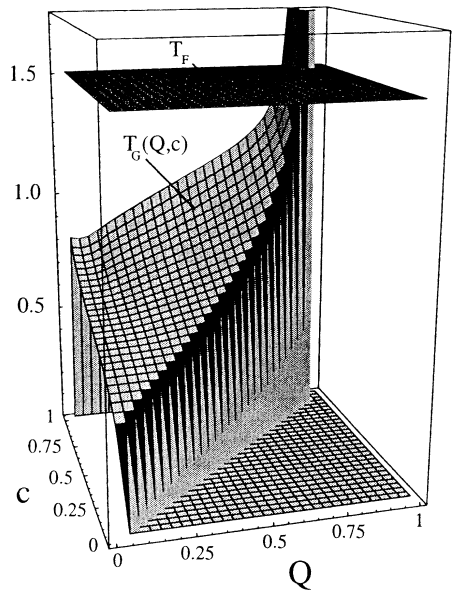

Fig. 15. The folding temperature (T_F) and glass transition temperature [T_G (Q, c)] as a function of the fraction of native contacts (Q) and the fraction of total contacts (c). The parameters used in the plot are taken from a fit of the theory to simulations (N, b, ϵ_N, $\bar{\epsilon}$, ν, b_N, p) = (27, 1·1, −2·1, −2·1, −1·3, 6, b, 1). The parameter ν is the number of conformational states per monomer in the coil phase. T_F is above T_G [Eq. (5.10)] for most values of Q and c, indicating that folding properties including rates and mechanism are largely self-averaging and not sensitive to sequence over most of the range of the order parameters.

which may be compared with Eq. (4.20) when $E_i = M\epsilon_N$ and a term $cM\bar{\epsilon}$ corresponding to the mean energy of collapse is added. Compare also Eq. (5.7) to Eq. (I-5.15) in the mean-field limit, i.e. neglecting core free-energy fluctuations so that $\delta F_C^2 = 0$. Equation (I-5.15) gives, in the notation of this section (Plotkin *et al.* 1997):

$$\frac{F_{MF}}{N}(Q, c) = cz\bar{\epsilon} + Qz\epsilon_N - (1-Q)\frac{cz b^2}{2T} - \frac{T}{N}(\bar{S}_C(Q, c) + S_{rout}(Q)), \tag{5.8}$$

so in Eq. (5.8) [and Eq. (I-5.15)] the entropy has been partitioned into a contribution from the polymer surrounding the core $\bar{S}_C$, and the number of distinct cores S_{rout}.

In equilibrium at the folding temperature, T_F, the folded ($Q \simeq 1$, $c \simeq 1$) and unfolded ($Q \simeq 0$, c) states have equal thermodynamic weights. Equation (5.6c) then gives an equation for T_F:

$$c^p\bar{\epsilon} - \frac{c^p b^2}{2T_F} - T_F\frac{s(0, c)}{z} = \bar{\epsilon} + \epsilon_N. \tag{5.9}$$

There is also a Q and c dependent temperature $T_G(Q, c)$ where the entropy Eq. (5.6b) vanishes:

$$T_G(Q, c) = \left[\frac{zc^p(1-Q^p)(b^2 + Q^p b_N^2)}{2s(Q, c)}\right]^{\frac{1}{2}}. \tag{5.10}$$

$T_G(Q, c)$ is plotted along with T_F in Fig. 15, for the case when $p = 1$, $b_N = b$. For this region

of the phase diagram, the folding funnel is indeed self-averaging, with $T_F/T_G \simeq 2$ in the molten globule or unfolded phase. Late in the folding process however it can be seen that $T_G \approx T_F$. Beyond this point, sequence specific features dominate the energy landscape, late-stage structural intermediates are predicted to be very sensitive to mutations, and the late-stage kinetics are governed by a few pathways rather than a multiplicity of routes. If the sequence were more poorly designed (smaller $|\epsilon_N|$), T_G would be comparable to T_F at smaller values of the reaction coordinates, with non-self-averaging behavior dominating more of the folding process (Bryngelson *et al.* 1995).

For the unfolded $Q \simeq 0$ phase,

$$T_G(0, c) = \sqrt{\frac{z c^p b^2}{2s(0, c)}}. \tag{5.11}$$

For large cooperativity p, $T_G(0, c)$ is small unless the polymer is fully collapsed ($c \approx 1$).

For a Gō model protein, $b = 0$, and the solution of Eq. (5.9) gives for the folding transition temperature:

$$T_F^{Go} = \frac{z[|\epsilon_N| - \bar{\epsilon}(1 - c^p)]}{s(0, c)}. \tag{5.12}$$

In general then when $b \neq 0$, T_F is given by

$$T_F = \frac{T_F^{Go}}{2} + \sqrt{\left(\frac{T_F^{Go}}{2}\right)^2 - (T_G(0, c))^2}. \tag{5.13}$$

It is interesting that even in an unfrustrated model protein with $b = 0$, the entropy may still vanish. From Eq. (5.10),

$$T_G(Q, c, b = 0) = b_N \sqrt{\frac{z c^p Q^p (1 - Q^p)}{2s(Q, c)}}. \tag{5.14}$$

This equation is similar in spirit to Eq. (I-5.18), in that below T_G in Eq. (5.14), the system takes one folding route to the native structure, through those strata of Q where $T < T_G(Q, c, b = 0)$. The folding mechanism for a single-route folder is described further in Section 7 (see bottom row of Fig. 31).

5.4 Free-energy surfaces and dynamics for a Hamiltonian with pair-wise interactions

The following analysis pertains to the case of a 2-body Hamiltonian ($p = 1$), unless otherwise noted.

To estimate realistic energy parameters for the funnel, a correspondence as described in Section I-6 was established between real proteins and minimalistic lattice models (Onuchic *et al.* 1995). We follow this prescription by fitting the resulting free energy of Eq. (5.6*c*) with $p = 1$ in our theoretical model to the free energy obtained from a lattice simulation. Temperature is fixed to the (arbitrary) value in the simulations at the point of folding equilibrium (where the free-energy depth of the folded and unfolded wells are equal) $T_F \equiv 1{\cdot}5$. Then the other three parameters b, $\bar{\epsilon}$, ϵ_N are found by minimizing a cost function to the shape of the lattice potential free energy (Plotkin *et al.* 1997): $(b, \bar{\epsilon}, \epsilon_N, T_F) = (1{\cdot}1, -1{\cdot}3, -2{\cdot}1, 1{\cdot}5)$. The parameters were found to be in reasonable agreement with those

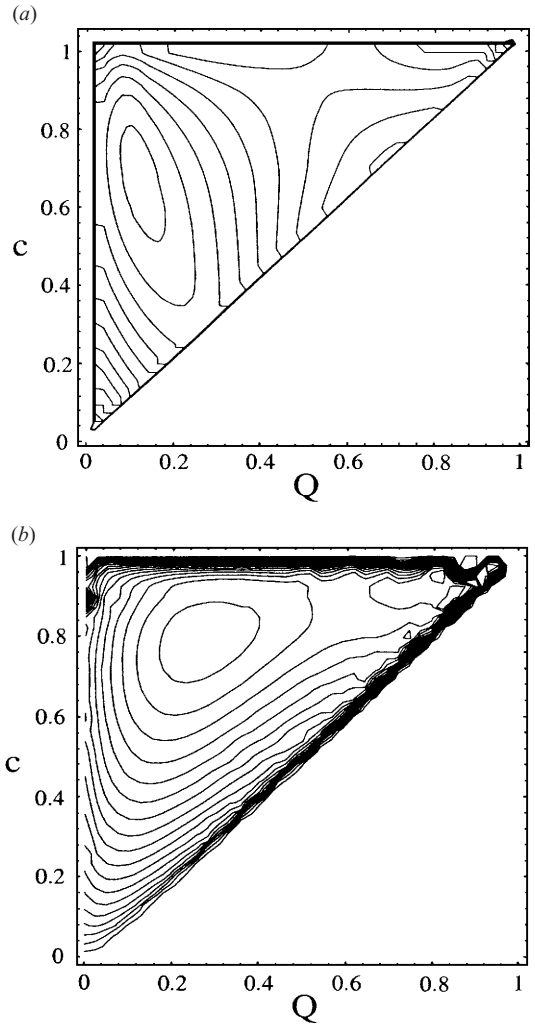

Fig. 16. (*a*) Free-energy surface $[F(Q, c)]$ at T_F for the 27-mer, obtained from Eq. (5.6*c*) with the parameters $(b, \bar{\epsilon}, \epsilon_N, T_F) = (1{\cdot}1, -1{\cdot}3, -2{\cdot}1, 1{\cdot}5)$, and $b_N = 0$, $p = 1$. The surface is plotted in contours of about $(\frac{1}{2})\, k_B T_F$. The surface has a double-well structure with a transition-state ensemble at $Q^{\ddagger} \simeq 0{\cdot}50$, and barrier height $\Delta F^{\ddagger} \simeq 3{\cdot}0\ k_B T$. (*b*) The free-energy surface $[F(Q, c)]$ at T_F, as obtained from simulations (Onuchic *et al.* 1995). The surface is plotted in contours of about $1\ k_B T_F$. For both cases the native minimum is in the uppermost right corner. The plots are in the upper diagonal half because there are always more total contacts than native contacts.

in the lattice simulations. The resulting free-energy profile, shown in Fig. 16, gives an approximation for the free-energy profile at T_F for a small single-domain protein, e.g. λ-repressor (Huang & Oas, 1995; Plotkin *et al.* 1997). For these parameters the free energy has a double-well structure at T_F. The transition is first-order-like, but the barrier height is only $\cong 3\, k_B T_F$, compared to an entropic barrier of $\cong 20\, k_B T_F$ to reach the transition state. The transition is nearly second-order due to the near cancellation of entropic losses with (negative) energetic gains as Q increases. As interactions become more cooperative, the barrier increases and the transition becomes more first-order-like, as we will see below.

The barrier peak is located at $Q^{\ddagger} \cong 0{\cdot}5$ and contains a transition state ensemble of $\approx 10^3$ thermally occupied states, supporting a description of generally delocalized nuclei seen in several studies (Itzhaki *et al*. 1995; Boczko & Brooks, 1995; Onuchic *et al*. 1996). Other native structures may have transition states with more localized nuclei, in that certain sets of contacts are preferred significantly over others, due to entropic or energetic reasons (Abkevich *et al*. 1994; Martinez *et al*. 1998; Grantcharova *et al*. 1998). The folding nucleus for some structures is inherently specific, while for other structures the folding nucleus is inherently diffuse, or non-specific (Onuchic *et al*. 1996; Klimov & Thirumalai, 1998b; Shoemaker *et al*. 1999). The degree of nucleus specificity in proteins is a quantitative rather than qualitative question. However at the mean-field level given here, the theory cannot address it.

A crude estimate of the reconfiguration time at the barrier position may be obtained from $\ln(k_f \bar{\tau}(Q^{\ddagger})) \simeq -(F^{\ddagger} - F_u)/T$. For example, for λ-repressor at the folding midpoint the folding rate is about 400 s^{-1} (Huang & Oas, 1995). Using the barrier height obtained from the above model $\Delta F^{\ddagger} \approx 3\, k_B T_F$ for the corresponding 27-mer lattice protein gives a reconfiguration time $\bar{\tau}(Q^{\ddagger}) \approx 10^{-4}$ s. Since Rouse–Zimm times for free polymer motions are in the nanosecond range, this suggests that configurational diffusion in the transition state region may be activated even at T_F. Unactivated diffusion would imply a free-energy barrier of about 15 $k_B T_F$.

5.5 The effects of cooperativity on folding

As the level of explicit cooperativity in the model increases, the funneled landscape converts to a golf-course topography, reproducing the REM limit, (see Figs. I-5*a* and 17). When interactions are strongly cooperative, much of the protein must be in native proximity to obtain a significant energetic benefit, leading to large entropic losses to reach the transition state. If all the residues must come together to achieve any energetic benefit, the Levinthal landscape is recovered. Detailed studies of the hydrophobic effect at variable length scales (Lum *et al*. 1999; Huang & Chandler, 2000; Hummer *et al*. 2000) indicate that the de-wetting effect involved in the attraction between hydrophobic elements in the protein is a collective one that appears on length scales $\gtrsim 1$ nm, comparable in size to a protein domain. De-wetting transitions have been studied recently as a late stage phenomenon in folding (Sheinerman & Brooks, 1998; Bursulaya & Brooks, 1999; Panick *et al*. 1999; Garcia & Hummer, 2000). While proteins have interspersed hydrophilic residues and relaxations involving side-chains which broaden the crossover, it is clear that interactions involving many-body effects are present in folding (Kolinski *et al*. 1996; Plotkin *et al*. 1997; Takada *et al*. 1999; Eastwood & Wolynes, 2001). The effects of these many-body effects may be investigated within the energy landscape formalism through Eq. (5.6*c*). The inset of Fig. 17*a* plots Eq. (5.6*c*) for two different values of p for purposes of illustrating the increase in barrier height, and the increase in the nativeness of the transition state cores, as cooperativity is increased. Figure 17*b* plots the trend in transition-state barrier height decomposed into entropic and energetic parts.

5.6 Transition-state drift

The stability gap ϵ_N may be decreased, for example by adding denaturant or making mutations in the sequence. As the native state is destabilized, the folding free-energy profile becomes more uphill, and the transition state should shift to larger values of Q. This transition-state drift has been seen in experiments, for example in CI2 and U1A (Oliveberg

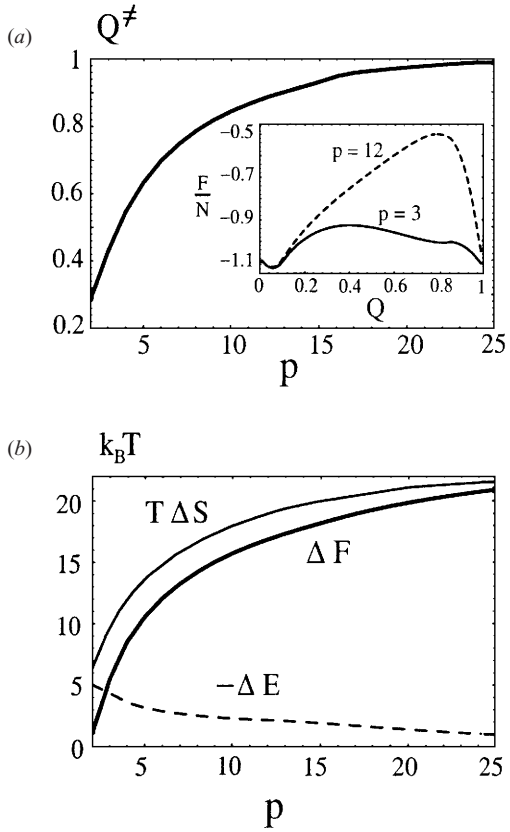

Fig. 17. (*a*) *Inset*: Free energy per monomer F/N for a 27-mer, in units of $k_B T_F$ as a function of Q, at constant density $\eta = 1$, with $s_0 = 0{\cdot}8$, for protein-like energetic parameters $(\epsilon_N, b) = (-2{\cdot}3, 1{\cdot}6)$. For these parameters $T_F \approx |\epsilon_N|$. For illustrative purposes, two values of p-contact interactions are chosen: ——, pure 3-body interactions; - - -, pure 12-body interactions. Note the trends in height and position of the barrier, and note how in the $p = 12$ case the free-energy curve is essentially $-T$ times the entropy curve $s(Q)$ of Fig. 5 with $\eta = 1$, until Q is very large. (*a*) *Main figure*: the position of the barrier peak (Q^+) increases with explicit cooperativity in p-contact forces. (*b*) The free-energy barrier height (ΔF) (in units of $k_B T_F$) is an increasing function of p. The barrier height rises to the limit of $T_F S(Q = 0)$ as $p \to \infty$, when it becomes completely entropic. Also shown are the energetic (- - -) and entropic (——) contributions to the barrier.

et al. 1998; Otzen *et al*. 1999), and it is interesting to compare the theoretical and experimental results. The mean transition-state position is experimentally measured by the change in rate over the change in stability under some global external perturbation such as adding denaturant, changing temperature, or making sequence mutations throughout the protein (for example by comparing sequence homologs):

$$\beta^+ \equiv -\frac{\delta \ln(k_F/k_0)}{\delta \ln K_{eq}}. \tag{5.15}$$

Here K_{eq} is the folding equilibrium constant. When the change in the rate prefactor with the perturbation can be neglected, Eq. (5.15) becomes

$$\beta^+ \simeq \frac{\delta F(Q^+) - \delta F_U}{\delta F_F - \delta F_U}, \tag{5.16}$$

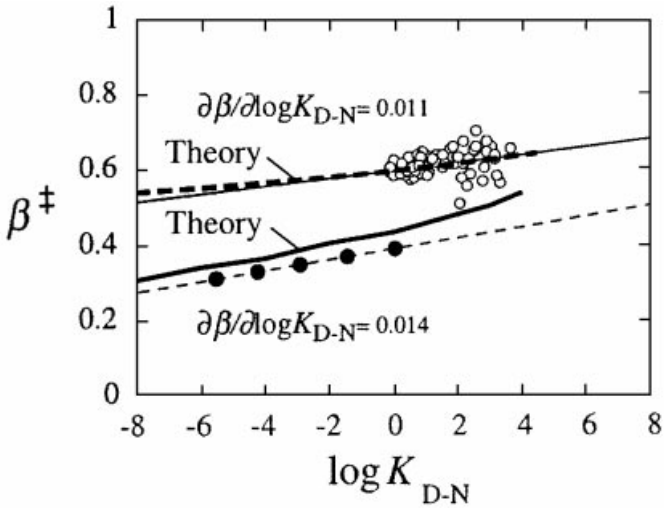

Fig. 18. Position of the transition state $\beta^{\ddagger}$ of CI2 plotted against protein stability. The slope $\partial\beta^{\ddagger}/\partial \ln K_{\mathrm{D-N}}$ is the transition-state drift. The lower curve is the result of thermal destabilization monitored by ϕ-values. The upper curve is the result from GdnHCl binding (*m*-values). The lower theory curve is from Eq. (5.18) derived from the free energy in Eq. (5.7) for the parameters (N, b, $\bar{\epsilon}$, ϵ_{N}, T, b_{N}, ν, p) = (27, 1·1, −1·3, −2·1, 1·5, 0, 6, 1) (see Plotkin *et al*. 1997). The upper experimental curve arises from hydrophobic forces which are believed to be intrinsically many-body in nature. The upper theory curve is obtained from Eqs. (5.18) and (5·6*c*) for $p = 4$, corresponding to 4-contact or 8-body interactions. The position of the transition state measured by overall collapse in Fig. 16 has somewhat larger values ($\epsilon^{\ddagger} \sim 0{\cdot}85$) than the upper curve here measuring hydrophobic burial of the transition state. (Adapted from Oliveberg *et al*. 1998.)

where we have approximated the free energy of the transition state by the free energy at $Q^{\ddagger}$. For small perturbations, the change in transition-state free energy may be approximated as a linear interpolation between the unfolded free-energy change and folded free-energy change:

$$\delta F(Q^{\ddagger}) \approx \left(\frac{Q^{\ddagger} - Q_{\mathrm{U}}}{Q_{\mathrm{F}} - Q_{\mathrm{U}}} \right) \delta F_{\mathrm{F}} + \left(\frac{Q_{\mathrm{F}} - Q^{\ddagger}}{Q_{\mathrm{F}} - Q_{\mathrm{U}}} \right) \delta F_{\mathrm{U}}, \tag{5.17}$$

where Q_{U}, Q_{F}, and $Q^{\ddagger}$, are the positions of the unfolded, folded, and transition state. When the transition state is nearly identical to the folded structure, $Q^{\ddagger} \to Q_{\mathrm{F}}$ and from Eq. (5.17) $\delta F(Q^{\ddagger}) = \delta F_{\mathrm{F}}$ as expected, and when $Q^{\ddagger} \to Q_{\mathrm{U}}$, $\delta F(Q^{\ddagger}) = \delta F_{\mathrm{U}}$. Inserting Eq. (5.17) into (5.16) gives:

$$\beta^{\ddagger} \simeq \left(\frac{Q^{\ddagger} - Q_{\mathrm{U}}}{Q_{\mathrm{F}} - Q_{\mathrm{U}}} \right). \tag{5.18}$$

Figure 18 shows a plot of the transition state position for CI2 *versus* stability, for two methods of measurement and for the theoretical results. The lower experimental curve shows the effect of thermal destabilization on the average ϕ-value, while the upper curve shows the effect of GdnHCl binding on exposed hydrophobic surface area. The transition state as measured from interaction energies (via thermal destabilization) is smaller and less native than the transition state measured from hydrophobic effects. The lower solid theory curve is the result of Eqs. (5.18) and (5.6*c*) with $b_{\mathrm{N}} = 0$, $p = 1$, and $N = 27$, as the stabilization energy ϵ_{N} is decreased (Plotkin *et al*. 1997). Again the theoretical 27-mer may be entropically

equivalent to a larger real protein due to transient helix formation (Onuchic *et al.* 1995) (see Section I-4.2), and this increases our faith in the comparison even though the chain lengths are indeed different. As mentioned above, the de-wetting transition involved in burying surface area is inherently a many-body effect. Thus it is interesting to ask what level of cooperativity in the theory is necessary to obtain the same result as the upper curve. Taking Eq. (5.18) using Eq. (5.6*c*) for $p = 4$, corresponding to 4-contact or 8-body interactions, gives good agreement with the experimental results (The curves for $p = 3$ and $p = 5$ differ from the curve shown by $\approx 5\%$). The theoretical transition-state drift is comparable to the observed drift.

Why is one curve higher than the other? Different experimental probes measure different order parameters, which may have different transition state positions. For example, a probe measuring the number of native interactions may infer a transition-state position at the $T_F \approx 0{\cdot}5$ from Fig. 16, while a probe measuring degree of overall collapse may measure a transition-state position of $\approx 0{\cdot}8$–$0{\cdot}9$ from the same figure. Moreover one may infer different transition-state ensembles from different measurements, since each measurement effectively projects different ensembles onto the transition state. For example, referring to Fig. 16 an experiment effectively using Q as a reaction coordinate measures the $Q^{\ddagger} \approx \frac{1}{2}$ transition-state ensemble, which includes states with all the degrees of collapse having $c \gtrsim \frac{1}{2}$. On the other hand, an experiment effectively using c as a reaction coordinate measures the $c \approx 0{\cdot}9$ transition-state ensemble, which includes states with all $Q \lesssim 0{\cdot}9$.

The stronger many-body effects are, the less drift. That is, larger cooperativity results in a larger, more sharply peaked barrier. Thus the transition-state drifts less for a given amount of destabilization, and the barrier persists over a larger range of denaturant concentration or thermal destabilization. Temperature dependence of interactions may additionally modify thermal drift measurements (Crane *et al.* 2000).

Changes in the prefactor may play a role in transition-state drift. For example, if the prefactor increased with native destabilization, due for example to the destabilization of kinetic traps with the addition of denaturant, rate-stability isotherms would curve upwards, opposite to the direction of curvature expected for the increase in native structure in the transition state. It is possible the effects of prefactor enhancement and transition-state destabilization may compensate each other to yield linear Bronsted plots over a larger range of stability than naively expected. On the other hand, if one then does observe rate-stability curvature in the direction of Hammond behavior, it is a good assumption that this is due to drift towards a more native thermodynamic transition state. However because of the possibility of this kind of hidden cancellation, one should use caution when drawing conclusions based on the linearity of Bronsted plots.

5.7 Phase diagram for a model protein

By finding the global free-energy minimum of Eq. (5.7) in the parameter space of the thermodynamic variables of the system, we can construct the phase diagram for a model protein, as shown in Fig. 19.

At the highest temperatures the protein is in the coil phase. As temperature is lowered or non-native variance is increased, a collapse transition takes place. For sufficiently low ruggedness, folding and collapse may occur concurrently. The coil-to-globule transition is second order here, without any free-energy barrier.

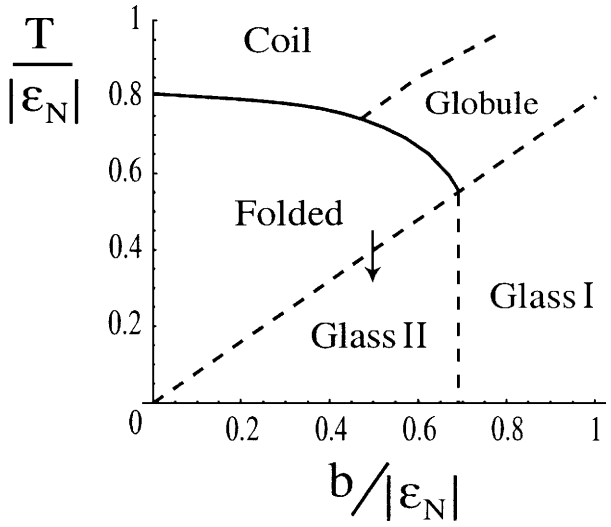

Fig. 19. Phase diagram for a model protein (cf. with Fig. 2 for the RHP). The axes are temperature in units of the mean native stability per monomer, and the roughness or standard deviation of non-native contact energies, in the same units. Other parameters are $(\bar{\epsilon}, b_N, p) = (-1{\cdot}2, 0, 1)$. The coil and globule phases are separated from the folded phase by a first-order-like transition, while the coil-to-globule and glass transitions are second order. In the glass II phase, the native basin is favored over all other low-energy basins. If it is approached above as indicated by the arrow, it retains non-zero configurational entropy, in contrast to the glass I phase, which has zero configurational entropy, and favors no specific basin.

The glass II phase in Fig. 19 is different than the glass I phase, in that the specific folded basin is favored over all other low-energy basins on the landscape. Since relaxation times diverge in the glass phase for a bulk system, kinetics becomes important in determining what state will be observed in practice. If the glass II region is approached from above as indicated by the arrow in the figure, the system is frozen into the basin corresponding to the folded state, and has residual entropy within that basin. At low temperatures the state of the protein is one in which it is frozen into an ensemble of substates in the native basin, as long as the temperature-dependent energy function is not significantly altered (Austin *et al*. 1975). In contrast, the glass I phase has essentially no configurational entropy. If the glass II phase is approached from the right, the slow kinetics of the glassy state prohibits the formation of the folded state, for a large system. This scenario as analogous to the phenomenon we saw earlier in Section 2.3 and in Fig. 2 in the context of micro-phase separation in a RHP. Just as the glass I phase is avoided in microphase separation, a glass I phase is avoided in low-temperature proteins by the presence of a folded state at higher temperature.

5.8 A non-Arrhenius folding-rate curve for proteins

To a good approximation the motion in Q is overdamped and Markovian, i.e. Brownian motion (see Section 6). Thus the folding time τ_f can be computed from diffusive rate theory (Bryngelson & Wolynes, 1989). We may obtain the mean folding rate from the Kramers law, Eq. (4.7*b*) using parameters from the energy landscape theory. The barrier $\Delta F^{\ddagger}$ and potential curvatures $\omega_u \omega^{\ddagger}$ are obtained from the thermodynamic analysis of Section 5.4. The friction kernel or diffusion coefficient D in Eq. (4.8) is obtained using Eq. (4.26).

The position of the kinetic bottleneck, Q^*, is the value of Q which, when substituted into Eq. (4.7*b*), maximizes the expression for the folding time. This includes the effects of a Q-dependent prefactor. Using the free-energy profiles in two reaction coordinates, Q and c, the value of Q^* is within 10% of $Q^{\ddagger}$, the position of the thermodynamic bottleneck, for the parameters used in Fig. 16.

The resulting mean first passage time, Eq. (4.7*a*), is plotted in Fig. 20*a* as a function of reciprocal temperature in units of T_F, and shows the non-Arrhenius behavior characteristic to proteins. Note this is the forward folding time, not the total relaxation time which would include both forward and backward rates. At high temperatures, the large entropy of the unfolded state slows the rate, and at low temperatures, various reconfigurational barriers contribute more strongly to slow the folding rate. In real proteins, the interactions which stabilize the folded structure are themselves temperature-dependent, which further slows the rate at low temperatures. This effect is not accounted for in this analysis, which assumes a temperature-independent Hamiltonian. The fact that proteins fold on biological timescales at biological temperatures is linked with the fact that above T_G where diffusion is slow, the thermodynamic profile favors the native state. Thus the temperature where a protein is biologically active is between T_F and T_G, which can only occur when $T_F/T_G > 1$. Sequences with a large range of foldable temperatures, i.e. with large T_F/T_G, tend to have faster folding rates (Bryngelson *et al*. 1995; Mélin *et al*. 1999; Dinner *et al*. 1999; Buchler & Goldstein, 1999). A relation between the optimal smallest folding time τ_f^{opt} and T_F/T_G should be derivable within the energy landscape formalism and is a problem for the future. The rate should correlate with T_F/T_G when the system is weakly to moderately minimally frustrated. However for steep funnels, i.e. T_F/T_G sufficiently large, the rate-limiting steps in folding may be governed more strongly by other factors, such as native topology (Plaxco *et al*. 1998), overall stability (Dinner & Karplus, 2001), specific collapse (Thirumalai, 1995), or net hydrophobicity (Klimov & Thirumalai, 1996).

6. Non-Markovian configurational diffusion and reaction coordinates in protein folding

Interactions with solvent and self-interactions within a protein damp intra-molecular motions. At the lengthscales and timescales of folding dynamics, the diffusion of side-chains and backbone is overdamped as discussed in Section I-3, and overdamped Langevin equations are occasionally used to simulate folding in coarse-grained models (Guo *et al*. 1992; Guo & Thorumalai 1996; Berriz *et al*. 1997; Guo & Brooks, 1997; Takada *et al*. 1999; Hoang & Cieplak, 2000). As well as all-atom models (Eastman & Doniach, 1998; Bursulaya & Brooks, 2000; Elmer & Pande, 2001). A coordinate whose motion is governed by a Langevin equation has a propagator or probability distribution $p(x, t)$ which obeys a Fokker–Planck equation (Doi & Edwards, 1986).

According to the energy landscape theory previously developed, protein folding can be seen as a stochastic motion of one or a few collective coordinates describing protein conformation, on an average thermodynamic potential. We saw in the last section that Fokker–Planck diffusion in Q gave a fairly accurate prediction of folding rate. However it is not clear a priori that the ensemble distribution $p(Q, t)$ of collective coordinate Q

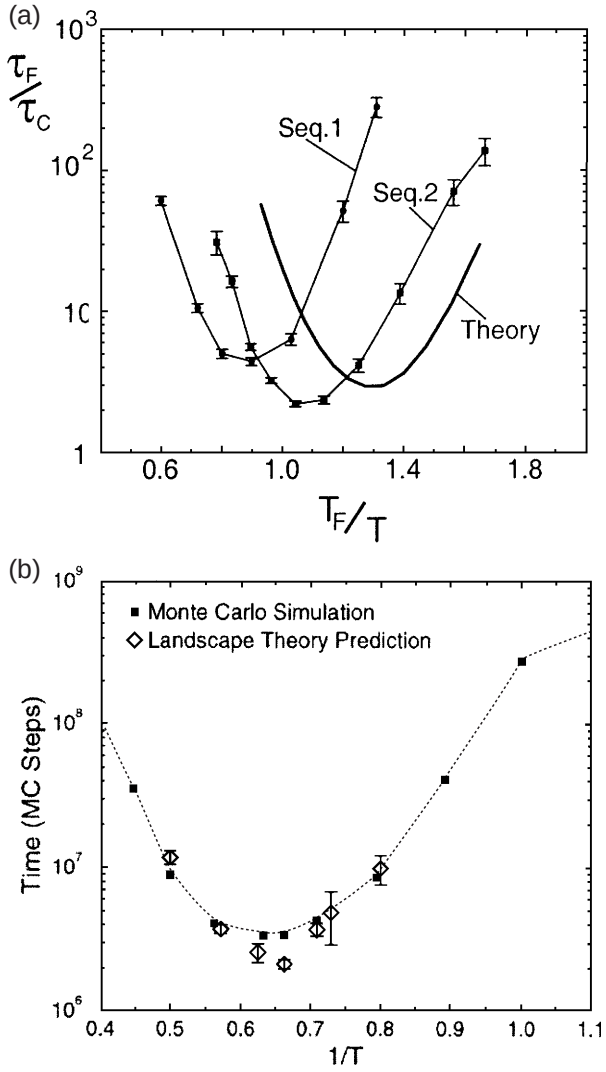

Fig. 20. (*a*) Folding time (not relaxation time), in units of the collapse time, as a function of one over temperature, in units of T_F. The plots show a minimum value which due to selection pressure may be close to biological temperatures. At low temperatures, τ_F becomes large in the model because diffusion is slow. Realistic temperature-dependent energy functions may no longer favor the native conformation at low temperatures, and this also slows the forward rate. At high temperatures diffusion is fast but folding is thermodynamically uphill because of the large entropy of the unfolded state, which again results in large folding times. The theory plot is for a sequence having the energetic parameters found earlier in Fig. 16, by fitting to a 27-mer lattice model with a 3-letter code. The folding time is normalized to the Rouse–Zimm timescale τ_0, assumed to be of the same order as the time τ_C for non-specific collapse. The data are from two lattice models (Nymeyer *et al.* 2001): Sequence 1 (●) is a 3-letter code ABCACABCCACBBCACACCCABCCACB with coupling energies either $\epsilon_{ij} = -3$ for like residues or $\epsilon_{ij} = -1$ for unlike residues. It has a ratio $T_F/T_G \approx 1{\cdot}44$. Sequence 2 (■) is a 36-mer with a 20-letter code NSKFFJOTGQAEECTRRPSNMBLHEKJDIJOPLIID with a Miyazawa–Jernigan contact energy matrix (Miyazawa & Jernigan, 1985, 1996), and $T_F/T_G \approx 1{\cdot}91$. The simulations seem to have relative optimal folding temperatures below those in the theory, for the parameters chosen here. This means that the model proteins in the simulations are more frustrated, in that their temperatures of fastest folding are near or above T_F indicating local kinetic traps are becoming important in determining folding rates even at T_F. On the other hand, the theory has a

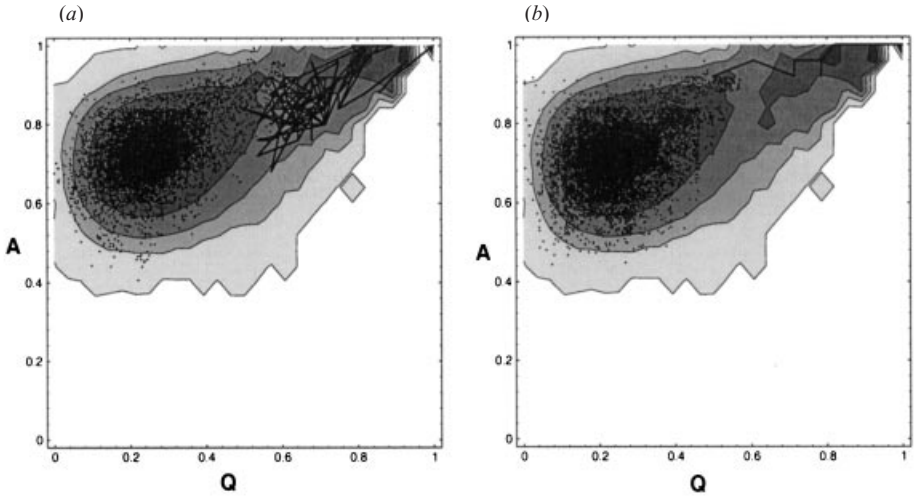

Fig. 21. Two folding trajectories projected onto the Q–A plane, where Q is the fraction of native contacts and A is the fraction of native dihedral angles. The model is a 3D cubic lattice heteropolymer with a contact potential where like monomers have contact energy -3 and unlikes have energy -1. The sequence ABABBBCBACBABABACACBACAACAB has all interactions equal to -3 in the ground state. The trajectories are superimposed on a contour plot of the free energy with levels spanning the range from $-82{\cdot}5$ to $-67{\cdot}5$ in increments of $2{\cdot}5$. The trajectories span $\sim \frac{1}{4}$ of the folding time, about 3×10^6 Monte Carlo steps. In the early part of the trajectories, the individual points are not connected and shown simply as dots, while in the latter part they are. In (*a*), the transition event occurs in $\sim 10^5$ Monte Carlo steps, indicating a diffusive, shuttling motion across the free-energy barrier. In (*b*), the trajectory moves quasi-ballistically across the transition region, in about 3000 Monte-Carlo steps. When such fast trajectories are present, non-Markovian effects may become important in determining the folding rate. (Adapted from Onuchic *et al*. 1995.)

representing degree of nativeness at time t indeed obeys Fokker–Planck diffusion as in Eq. (4.3), or equivalently that the coordinate Q obeys a Langevin equation:

$$-\frac{\mathrm{d}F(Q)}{\mathrm{d}Q} - \zeta(Q)\dot{Q}(t) + \xi(Q, t) = 0,$$

with $\langle \xi(Q, t) \rangle = 0$ and $\langle \xi(Q, 0)\xi(Q, t) \rangle = T\zeta(Q)\delta(t)$.

In fact when the dynamics of reconfiguration, which occurs on many timescales for a system with a rugged landscape or with many relevant lengthscales, is projected onto a single reaction coordinate such as Q, the information of the dynamics of the fast and slow modes is obtained in a new frequency-dependent diffusion constant. Thus the dynamics

---

temperature regime where as folding becomes more thermodynamically downhill, the rate increases, because kinetic slowing down has not yet become appreciable. At lower temperatures, energetic traps become more important and the folding time then increases. (*b*) When the friction and barrier are obtained directly from the lattice data (see Section 6.3), the Kramers rate expression [Eq. (6.29)] and the mean first passage time directly measured from simulations are within a factor of 2, indicating a diffusive barrier crossing theory is a good predictor of rates. The numbers given for the landscape theory include a calculation of the diffusion coefficient appearing in the rate prefactor, as well as the free-energy barrier. Both quantities are obtained for the same model protein for which the mean first passage time was obtained directly. The prefactor is obtained by measuring the auto-correlation time of conformational motions projected onto Q in the molten globule state for the simulated model protein, and the free-energy barrier obtained directly from sampling (hence the error bars for the landscape theory results). (Adapted from Socci *et al*. 1996.)

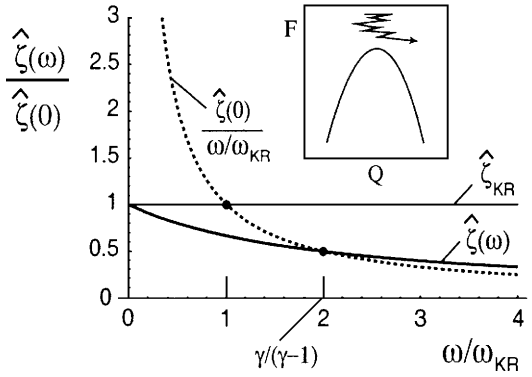

Fig. 22. Enhancement of escape rate from the barrier peak over the Kramers escape rate [with friction $\hat{\zeta}(0)$], for a frequency-dependent friction kernel obeying Eq. (6.7), with $\gamma = 2$. From Eq. (6.5), the escape frequency ω^* is where $\hat{\zeta}(\omega^*)/\hat{\zeta}(0) = \omega_{KR}/\omega^*$, and so is determined through the intercept of $1/\omega$ with the friction as a function of frequency. Here then $\omega^* = \gamma/(\gamma-1)\omega_{KR}$.

should rigorously be treated as non-Markovian (Plotkin & Wolynes, 1998). Non-Markovian dynamics will affect reaction rates when the time to cross the top of the barrier is comparable to the memory time of the fluctuating forces acting on the collective coordinate.

In simulations, many barrier-crossing trajectories are diffusive, as in Fig. 21*a*, supporting a Kramers description for the folding rate. However, some barrier-crossing trajectories are quasi-ballistic as in Fig. 21*b*, indicating that these fast trajectories may cross within the memory time of the effective forces driving diffusion. To the first approximation, when the (Laplace-transformed) friction evaluated at the Kramers barrier-crossing frequency is significantly less than the friction at zero frequency, i.e. when

$$\hat{\zeta}\left(\frac{m\omega^{\mp 2}}{\hat{\zeta}(0)}\right) \lesssim \hat{\zeta}(0), \tag{6.1}$$

then non-Markovian effects are important in determining the rate.

Then motion along the coordinate Q should be characterized by an overdamped generalized Langevin equation (GLE):

$$\frac{\mathrm{d}F(Q)}{\mathrm{d}Q} - \int_0^t \mathrm{d}\tau\, \zeta(Q, t-\tau)\dot{Q}(\tau) + \xi(Q, t) = 0, \tag{6.2}$$

with $\langle \xi(Q, t)\rangle = 0$ and $\langle \xi(Q, 0)\xi(Q, t)\rangle = T\zeta(Q, t)$.

6.1 An illustrative example

A simple example to illustrate the importance of non-Markovian effects is to consider the characteristic escape time or escape frequency from an inverted oscillator with stiffness $m\omega^{\mp 2}$ (inset of Fig. 22). Defining the time autocorrelation function $c(t)$ as

$$c(t) = \frac{\langle Q(0)Q(t)\rangle}{\langle Q(0)^2\rangle}, \tag{6.3}$$

Eq. (6.2) becomes

$$m\omega^{\mp 2}c(t) - \int_0^t \mathrm{d}t'\ \zeta(t-t')\dot{c}(t') = 0, \tag{6.4}$$

whose Laplace transform $\hat{c}(\omega)$ has the form $\hat{c}(\omega) = c(0)/(\omega - (m\omega^{\mp 2}/\hat{\zeta}(\omega))$, with a pole at

$$\omega^* = \frac{m\omega^{\mp 2}}{\hat{\zeta}(\omega^*)}, \tag{6.5}$$

which is precisely the Grote–Hynes barrier crossing frequency, as determined in Grote & Hynes (1980) from time correlation functions for the forward rate constant. If the random force correlations decay rapidly compared to the 'velocity' $\dot{Q}(t)$, Eq. (6.4) becomes

$$m\omega^{\mp 2}c(t) - \dot{c}(t)\hat{\zeta}(0) = 0, \tag{6.6}$$

which yields an exponentially diverging time-correlation function: $c(t) = c(0)\mathrm{e}^{(m\omega^{\mp 2}/\hat{\zeta}(0))t}$, whose Laplace transform $\hat{c}(\omega)$ has a pole at $m\omega^{\mp 2}/\hat{\zeta}(0)$, which is the Kramers correction to the forward rate in the spatial diffusion limit (Kramers, 1940).

One can see from Eq. (6.5) that the escape time from the barrier peak involves the high frequency components of the spectral resolution of $\zeta(t)$. If these are smaller than the zero frequency (long-time) friction assumed in the Kramers approximation, the forward rate is significantly modified.

To be specific, let the friction have an exponential time decay, as $\zeta(t) = \hat{\zeta}(0)\gamma\omega_{\mathrm{KR}}\ \mathrm{e}^{-\gamma\omega_{\mathrm{KR}}t}$, where ω_{KR} is the Kramers frequency $m\omega^{\mp 2}/\hat{\zeta}(0)$ and γ is a proportionality constant with $\gamma \geqslant 0$. Then the frequency-dependent friction kernel is

$$\hat{\zeta}(\omega) = \frac{\gamma\omega_{\mathrm{KR}}}{\omega + \gamma\omega_{\mathrm{KR}}}\hat{\zeta}(0). \tag{6.7}$$

Inserting this into Eq. (6.5) gives the barrier-escape frequency: $\omega^* = (\gamma/(\gamma-1))\omega_{\mathrm{KR}}$. This has a real, positive frequency only when $\gamma > 1$, i.e. when the random force correlations decay more rapidly than the Kramers frequency. Otherwise, the velocities are not in equilibrium over the period of time the system crosses the barrier peak, and the motions are ballistic. For $\gamma > 1$, the escape frequency $\omega^* > \omega_{\mathrm{KR}}$, so the escape rate is enhanced, as illustrated in Fig. 22. The effective friction governing escape is given by

$$\hat{\zeta}(\omega^*) = \left(1 - \frac{1}{\gamma}\right)\hat{\zeta}(0). \tag{6.8}$$

When $\gamma \to \infty$, the forces decorrelate infinitely fast, then $\omega^* \to \omega_{\mathrm{KR}}$ and $\hat{\zeta}(\omega^*) \to \hat{\zeta}(0)$.

This example illustrates that the dynamics that determine the barrier crossing rate depend on the short time 'non-adiabatic' friction experienced during passage over the barrier and thus involve the high-frequency components of the spectral resolution of the friction. When these components of the friction are much weaker than the long-time values, the forward rate may be strongly enhanced.

6.2 Non-Markovian rate theory and reaction surfaces

The projection onto Q of dynamics occurring on many timescales introduces memory effects into the friction kernel. In what follows, we determine the impact of these non-Markovian

effects on the folding dynamics (Plotkin & Wolynes, 1998). This addresses the validity of using Q as a reaction coordinate: if non-Markovian effects are large, it is obvious then that much information was lost in the projection of dynamics onto Q.

For dynamics governed by a GLE as in Eq. (6.2), it is implicit that Q responds linearly to fluctuations in the other coordinates of the polymer chain apart from the nonlinearity inherent in the thermodynamic potential for Q. This should be a good approximation if many individual configurational states of the polymer chain are sampled for each value of Q, as expected above the glass transition temperature. On the other hand, nonlinearities must be present in proteins that have multi-exponential kinetics, as occurs for example in kinetic partitioning mechanisms (Guo & Thirumalai, 1995), which will be an interesting phenomenon to incorporate into this framework.

A system governed by the generalized Fokker–Planck equation in Eq. (4.5) shows the same linear response as the GLE in Eq. (6.2) (see Appendix D for a proof of this). That is, the Fourier transformed friction $\hat{\zeta}(Q, \omega)$ and the diffusion coefficient $\hat{D}(Q, \omega)$ at frequency ω are related by

$$\hat{\zeta}(Q, \omega, T) = \frac{k_B T}{\hat{D}(Q, \omega, T)}. \tag{6.9}$$

As mentioned earlier in Section 4 Eq. (4.8), these quantities may be obtained by mapping the generalized Fokker–Planck equation to a generalized master equation, with transition dynamics between states obeying a waiting-time distribution. The waiting-time distribution which determines the diffusion coefficient may be obtained by appealing to the statistics of escape times on the energy landscape, as in Eq. (4.24). It was shown in Bryngelson & Wolynes (1989) by employing this mapping that the diffusion coefficient is given by

$$\hat{D}(Q, \omega, T) = \frac{k_B T}{\hat{\zeta}(Q, \omega, T)} = \lambda(Q)\frac{\langle 1/(1+\omega\tau)\rangle}{\langle \tau/(1+\omega\tau)\rangle}, \tag{6.10}$$

where $\lambda(Q)$ involves the distance scale for conformational diffusion, and is related to the step size in Q, ΔQ, and the probability that a given microscopic transition changes Q.

The averages in Eq. (6.10) are taken over the hopping time distribution $P_Q(\tau, T)$. For example,

$$\left\langle \frac{1}{1+\omega\tau} \right\rangle \equiv \int \mathrm{d}\tau \, P_Q(\tau, T)\frac{1}{1+\omega\tau}, \tag{6.11}$$

where $P_Q(\tau, T)$ is obtained from Eq. (4.24), with the entropy S and T_G given by their values at Q: $S \to S(Q)$ and $T_G \to T_G(Q)$.

The diffusion coefficient obtained in this way is plotted in Fig. 23. At a rigorous dynamic glass temperature T'_A, where escape barriers on all timescales disappear, the system is free to reconfigure at relatively fast Rouse–Zimm timescales (top curve in Fig. 23). Below T'_A however, a distribution of barrier heights induces a stronger frequency dependence to the diffusion coefficient. The dispersion arises from the number of deep traps *versus* the number of shallow traps, and so maximal at an intermediate temperature between T'_A and T_G, where both escape processes have large contributions to the diffusion coefficient.

Non-Markovian rate theory (Chandler, 1978; Grote & Hynes, 1980; Pechukas, 1981; Pollak *et al.* 1990; Pollak, 1992; Berezhkovskii *et al.* 1992; Rips, 1998) proceeds by

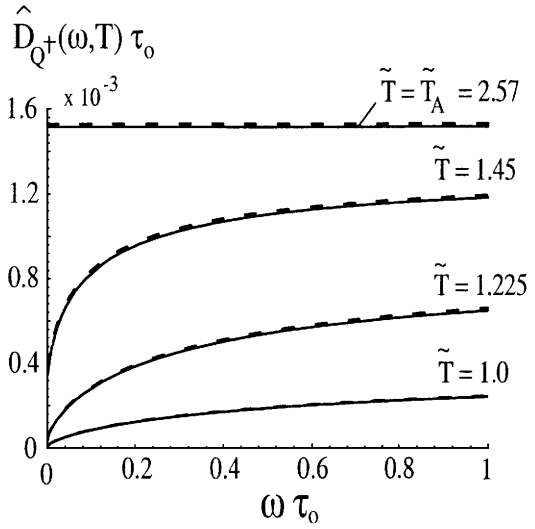

Fig. 23. Diffusion coefficient $\tau_0\,\hat{D}(Q^{\ddagger}, \omega, \tilde{T})$ for the 64-mer near the transition state $Q^{\ddagger} \approx 0{\cdot}3$, as a function of frequency (times τ_0), at several temperatures between the thermodynamic glass temperature and dynamic glass temperature, where the dynamics is no longer activated. The solid lines are from Eqs. (6.10) or (D 8), and the dashed lines are for the closed-form approximate solution, Eq. (D 10). Here temperatures $\tilde{T}$ are in units of T_G. There is a rapid increase from the zero frequency value $\hat{D}(Q, 0, \tilde{T})$, which depends on the typical escape time at that temperature, to a higher asymptotic value depending on how many of the states are untrapped and have short lifetimes at that temperature. The dispersion in the values of the diffusion for different frequencies is thus maximum at intermediate values of temperature. The temperature T_A here, where there is no frequency dependence left in the diffusion coefficient, is above the dynamic glass temperature in, e.g. Fig. 13. This is because at T_A here, all traps must have downhill free-energy profiles for escape, not just the traps typically occupied (at the thermal energy). The largest values of the diffusion constant are set by $\lambda(Q)$ in Eq. (6.10), and at T_A, $\hat{D}(Q^{\ddagger}, \omega, T_A) = \lambda(Q) \approx 0{\cdot}0015/\tau_0$ for the 64-mer.

recognizing that the GLE is equivalent to a particle bi-linearly coupled to a bath of oscillators (Zwanzig, 1973; Caldeira & Leggett, 1983) with an effective Hamiltonian

$$\mathscr{H} = \frac{p_Q^2}{2m^*} + F(Q) + \frac{1}{2}\sum_j \left[\frac{p_{xj}^2}{m_j} + m_j\omega_j^2 \left(x_j - \frac{c_j Q}{m_j\omega_j^2} \right)^2 \right] \tag{6.12}$$

with

$$\zeta(Q, t) = \sum_j \left(\frac{c_j^2}{m_j\omega_j^2} \right) \cos(\omega_j t). \tag{6.13}$$

Because the dynamics in Q is overdamped, m^* will be set to zero at the end of the calculation, i.e. there are no inertial terms. The observable quantities $m^*\omega^{\ddagger 2} = F''(Q^{\ddagger})$ and $\zeta(Q, t)$ or $\hat{\zeta}(Q, \omega)$ are taken to remain finite in this limit.

The additional collective modes of the bath in Eq. (6.12) describe the dynamics behind the fluctuations in Q within linear response. Rather than explicitly dealing with integral equations accounting for memory in the non-Markovian dynamics of Q, we can study the dynamics of an equivalent multi-dimensional system without memory, by re-projecting out onto the many dimensions of the bath, as long as bath modes reproduce the spectral decomposition of the friction, as ensured by Eq. (6.13).

When a single barrier exists in $F(Q)$ it makes sense to use multi-dimensional transition state theory (TST). The Hamiltonian [Eq. (6.12)] is brought to normal coordinates through an orthogonal normal mode transformation

$$m^{*\frac{1}{2}}Q' \equiv m^{*\frac{1}{2}}(Q-Q^{\ddagger}) = u_{00}\rho + \sum_j u_{j0}y_j, \tag{6.14}$$

where u_{00}, u_{j0} are coefficients of the transformation, which are a function of the friction kernel. For example

$$\frac{u_{00}^2}{m^*} = 2\left[\frac{\hat{\zeta}(Q^{\ddagger},\lambda^{\ddagger})}{\lambda^{\ddagger}} + \left.\frac{\partial\hat{\zeta}(Q^{\ddagger},\omega)}{\partial\omega}\right|_{\omega=\lambda^{\ddagger}}\right]^{-1} \equiv v_{00}^2. \tag{6.15}$$

The coordinate ρ in Eq. (6.14) is the reaction coordinate along the unstable normal mode, having imaginary frequency $i\lambda^{\ddagger}$ given by the solution of

$$\lambda^{\ddagger}\hat{\zeta}(Q^{\ddagger},\lambda^{\ddagger}) = m^*\omega^{\ddagger 2} = \left|\frac{\partial^2 F(Q)}{\partial Q^2}\right|_{Q^{\ddagger}}. \tag{6.16}$$

This frequency is identical to the (overdamped $m^* \to 0$) Grote–Hynes reactive frequency (Grote & Hynes, 1980). Friction leaves the barrier height unchanged, but rotates the reaction coordinate to a different direction in configuration space. The Grote–Hynes frequency arises from solving diffusion with memory on an inverted parabolic potential, as we saw in Section 6.1. When the motion in Q is Markovian and diffusive, the reactive frequency is that of an overdamped inverted harmonic oscillator corresponding to the Kramers prefactor in the rate. That is

$$\lambda^{\ddagger} = \frac{m^*\omega^{\ddagger 2}}{\hat{\zeta}(Q^{\ddagger},0)}. \tag{6.17}$$

Once transformed, the Hamiltonian has the form

$$\mathcal{H} = \tfrac{1}{2}[p_\rho^2 - \lambda^{\ddagger 2}\rho^2 + \sum_j (p_{y_j}^2 + \lambda_j^2 y_j^2)] + F_{\mathrm{AN}}(m^{*-\frac{1}{2}}[u_{00}\rho + \sum_j u_{j0}y_j]), \tag{6.18}$$

which is quadratic except for the anharmonic part of the potential F_{AN} which mixes all the coordinates nonlinearly. However this mixing is done only through the sum $\Sigma_j u_{j0}y_j$. It is therefore useful to define, in addition to the Grote–Hynes coordinate ρ, a residual collective bath coordinate σ by

$$m^{*\frac{1}{2}}\sigma \equiv (1-u_{00}^2)^{-\frac{1}{2}}\sum_j u_{j0}y_j \equiv \frac{1}{u_1}\sum_j u_{j0}y_j, \tag{6.19}$$

and calculate the TST rate k_{F} (Hanggi *et al.* 1990) across a new thermodynamically determined dividing surface on the 2D potential in (ρ, σ) space:

$$k_{\mathrm{F}} = \frac{\int \mathrm{d}p_\rho\, \mathrm{d}\rho\, \mathrm{d}p_\sigma\, \mathrm{d}\sigma\, \delta(f)(\nabla f\cdot\mathbf{p})\theta(\nabla f\cdot\mathbf{p})\mathrm{e}^{-\beta\mathcal{H}^{\ddagger}}}{\int \mathrm{d}p_\rho\, \mathrm{d}\rho\, \mathrm{d}p_\sigma\, \mathrm{d}\sigma\, \mathrm{e}^{\beta\mathcal{H}^{\ddagger}}}. \tag{6.20}$$

The effects of dynamic friction, reflected by recrossings in the Q coordinate, are then accounted for by ballistic motion across the surface $f = 0$ dividing reactants and products. The delta function $\delta(f)$ in Eq. (6.20) localizes the integration to that surface, and $\nabla f\cdot\mathbf{p} =$

$p_\rho \partial f/\partial\rho + p_\sigma \partial f/\partial\sigma$ is the flux density across the surface, which the theta function insures is in the forward direction. The function $f = \rho - g(\sigma)$ serves as a new reaction coordinate in this formulation of the problem. The problem is now reduced to determining the surface $f = \rho - g(\sigma) = 0$ that gives the slowest TST rate, or lowest upper bound to the true rate. Note in this analysis no assumptions are made about the memory time of the friction, or how anharmonic the potential is.

The shape of the dividing surface $g(\sigma)$ that minimizes the TST rate k across the surface can be found by using the calculus of variations (Miller, 1974; Pollak, 1991) as, for example, in the derivation of Lagrange's equations in mechanics, yielding a differential equation for the shape of the dividing surface $g(\sigma)$

$$\frac{g''}{1+g'^2} = \beta \left[g' \frac{\partial E[g]}{\partial \sigma} - \frac{\partial E[g]}{\partial g} \right], \tag{6.21}$$

where $g' \equiv \mathrm{d}g/\mathrm{d}\sigma$, and

$$E[g] = \tfrac{1}{2}(m^*\Omega^2\sigma^2 - \lambda^{\ddagger 2} g(\sigma)^2) + F_{\mathrm{AN}}(v_{00} g(\sigma) + \sigma), \tag{6.22}$$

where $m^*\Omega^2 = (v_{00}^2/\lambda^{\ddagger 2} - 1/m^*\omega^{\ddagger 2})^{-1}$ is a collective bath frequency.

We can treat g and σ as parameterized variables in terms of an independent parameter t, such that, e.g. $g' = \dot{g}/\dot{\sigma}$, and set the first integral to an effective energy:

$$\tfrac{1}{2}(\dot{g}^2 + \dot{\sigma}^2) \equiv E_0 - V_\beta. \tag{6.23}$$

This recasts the variational Eq. (6.21) into Hamilton's equations of motion for g and σ,

$$\ddot{g} = -\frac{\partial V_\beta}{\partial g} \tag{6.24a}$$

$$\ddot{\sigma} = -\frac{\partial V_\beta}{\partial \sigma}, \tag{6.24b}$$

on an effective temperature dependent potential:

$$V_\beta = -\frac{1}{2\beta} \exp(-2\beta E[g]) \tag{6.25}$$

at total energy

$$\tfrac{1}{2}(p_g^2 + p_\sigma^2) + V_\beta = 0. \tag{6.26}$$

The optimal dividing surface is a classical periodic trajectory (Pechukas, 1981) with infinite period, on the potential V_β at total energy zero, that divides the (ρ, σ) space into reactants and products.

Equation (6.20) for the rate then becomes

$$k_{\mathrm{F}} = p_{\mathrm{AN}} \frac{\lambda^{\ddagger}}{\omega^{\ddagger}} k_0, \tag{6.27}$$

where $k_0 = (\omega_0/2\pi)\exp(-\beta F^{\ddagger})$ is the TST rate, while $\lambda^{\ddagger}/\omega^{\ddagger}$ is the Grote–Hynes transmission factor.

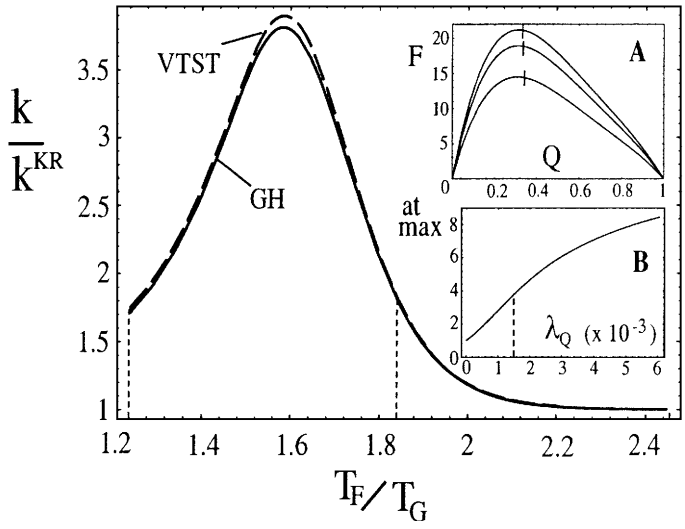

Fig. 24. Ratio of the Grote–Hynes (GH) rate (solid lines) and variational TST rate (VTST – dashed lines) to the Kramers rate, for a 64-mer at folding equilibrium, as a function of how minimally frustrated to protein is, characterized by T_F/T_G. The VTST result includes rate enhancement due to anharmonic effects of a finite size barrier. The effect here is small, indicating that the Grote–Hynes prediction of $k^{GH}/k^{KR} = \hat{D}(Q^{\ddagger}, \lambda^{GH})/\hat{D}(Q^{\ddagger}, 0)$ is a good approximation for proteins with a large, dominant folding barrier. In fact the Grote–Hynes result is typically within a factor of about 3 of the Kramers rate, indicating that even the Kramers result is a good approximation (see also Section 6.3). Larger variational effects on the reaction coordinate are seen for shorter polymers that for longer ones. *Inset* A: Thermodynamic potentials *versus* Q at T_F. For more rugged landscapes the barrier is flatter, and this reduces the overall prefactor to the rate since there are more recrossings. However, the non-Markovian effects on rate are actually enhanced for these moderately rugged landscapes, because of the increased dispersion in the spectral decomposition of the diffusion coefficient (cf. Fig. 23). The T_F/T_G values are 2·45, 1·84, and 1·24 in order of decreasing barrier size, which are marked by the dashed vertical lines in the main figure. The small vertical bars near the barrier peaks are where the VTST dividing surfaces cross the coordinate Q. These are close to the barrier peak, but need not coincide with it, due to the fact that the barrier is not exactly an inverted parabola. *Inset* B: Enhancement of the rate k/k^{KR} at the maximum value when $T_F/T_G \approx 1{\cdot}6$ by allowing the 'step size' λ_Q in the diffusion coefficient $\hat{D}(Q^{\ddagger}, \lambda^{GH})$ to vary ($\lambda(Q) \approx 0{\cdot}0015$ is the value in the main figure, which gives $k/k^{KR} \approx 3{\cdot}8$).

The anharmonic correction p_{AN} to the Grote–Hynes prefactor is given by the classical action of a fictitious particle following the trajectory of the dividing surface on the effective potential V_β of Eq. (6.25):

$$p_{AN} = \left(\frac{\beta^2 m^* \Omega^2}{2\pi} \right)^{\frac{1}{2}} \int \mathrm{d}s \sqrt{-2V_\beta} \tag{6.28}$$

where ds is arc length along the trajectory.

For large heteropolymer globules (with larger folding barriers), the potential $F(Q)$ is nearly parabolic near the barrier peak, and the rate approaches the Grote–Hynes rate, with $p_{AN} \cong 1$ in Eq. (6.27). This is shown in Fig. 24, which plots the forward folding rate in units of the Kramers rate, taking into account the effects of non-Markovian diffusion, on a model protein of size $N = 64$ *versus* the amount of minimal frustration in the protein, T_F/T_G. For these larger barriers (shown in inset A of Fig. 24), non-Markovian effects increase the rate

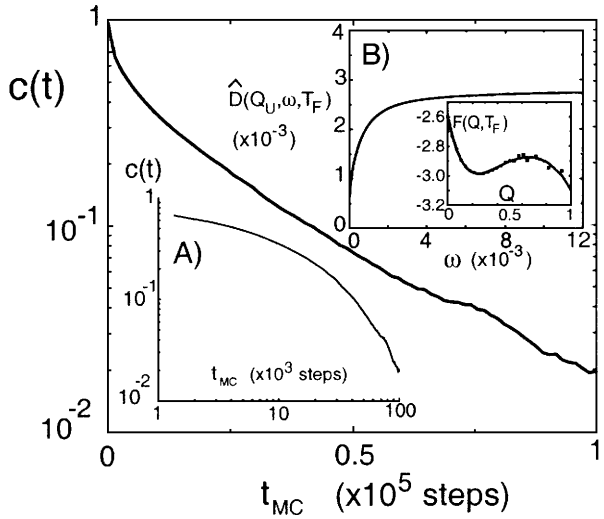

Fig. 25. Autocorrelation function [Eq. (6.3)] from the lattice data for the 27-mer 3-letter code, at the folding transition temperature (T_F), in the unfolded free-energy minimum (see Socci *et al*. 1996). *Inset* A shows the same data on a log–log plot. *Inset* B shows the corresponding diffusion coefficient from Eqs. (6.30) and (6.9) as a function of frequency. The data cannot be fitted by one exponential; the faster decay at small times means that the high-frequency diffusion coefficient is larger than that for the low-frequency modes. The diffusion coefficient and potential $F(Q)$ in the inset are used to calculate the non-Markovian forward folding rate.

about 4-fold over the Kramers approximation. In the limiting case where the potential $F(Q)$ is parabolic and the friction ζ_0 is frequency independent, the Kramers rate

$$k_{\mathrm{KR}} = \frac{m^*\omega_u\omega^+}{2\pi\zeta_0}\exp(-\beta F^+) \tag{6.29}$$

is recovered from Eq. (6.27).

6.3 Application of non-Markovian rate theory to simulation data

The Kramers rate theory has already been applied to the data for the lattice 27-mer in Socci *et al*. (1996), and shown there to give values within a factor of 2 or 3 of the simulated folding rates. We can go a step further here and test the validity of the Kramers result by applying non-Markovian rate theory to calculate rates for model proteins for which simulation data are available, and compare the result to the one assuming white-noise diffusion.

For example, the thermodynamic reaction surface in one coordinate is shown for the 3-letter code 27-mer at T_F in Fig. 25, inset B. From measurements of the autocorrelation function defined by Eq. (6.3) and shown in Fig. 25 (see Socci *et al*. 1996), the friction $\hat{\zeta}(\omega)$ may be obtained from the GLE [Eq. (6.2)] at the position of the unfolded free-energy minimum:

$$\hat{\zeta}(\omega) = \frac{F''(Q^+)}{1/(\hat{c}(\omega)) - \omega}, \tag{6.30}$$

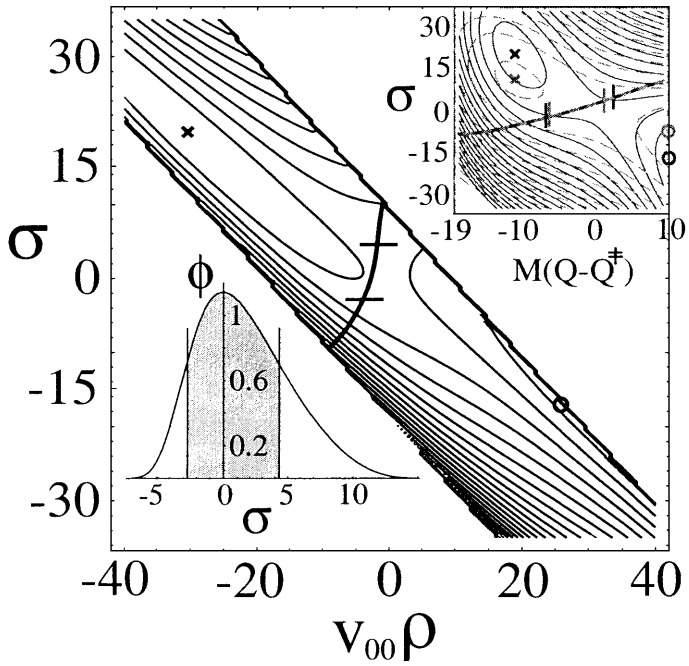

Fig. 26. Potential surface in the normal coordinates, $E(v_{00}\rho, \sigma)$, and in Q and the bath coordinate, $E(Q-Q^{\ddagger}, \sigma)$ (solid contours in inset), along with the variational dividing surface which minimizes the TST flux (heavy curve), for a lattice-model 3-letter code protein of length $N = 27$. Contours are drawn at intervals of about 2 $k_B T$. Note the kinetic dividing surface is slightly off the thermodynamic saddle point, towards the shallower well. The potential in the Markovian case (dashed inset), with the corresponding Kramers rate, is further skewed with respect to the dividing surface, indicating paths in this case are even more diffusive. × marks the position of the unfolded minimum, and ○ the native minimum. The short horizontal lines (and vertical lines in the inset) bound a region of ≈ 70% of the total flux across the dividing surface. The distribution of flux across the surface as a function of bath coordinate σ is shown in the lower inset. The shaded region contains ≈ 70% of the flux. In $(Q-Q^{\ddagger}, \sigma)$ space there is flux over a wide range of Q values, $\Delta Q/(Q_F - Q_U) \approx 0{\cdot}44$, so that the TST that reproduces the multiple crossing physics in Kramers theory does not have a well defined value of $Q^{\ddagger}$. However in $(v_{00}\rho, \sigma)$ space the TST surface tends towards orthogonality to the reaction coordinate $v_{00}\rho$: $\Delta\rho/(\rho_{native} - \rho_{mg}) \approx 0{\cdot}04$, indicating trajectories behave more ballistically along ρ, and would correlate more strongly with the probability of folding. The finite width of the strip in $(v_{00}\rho, \sigma)$ space is due to the finite range of Q: $0 < MQ < 28$.

where $\hat{c}(\omega) = \mathscr{L}_t c(t)$. By Eq. (6.9), the diffusion coefficient $\hat{D}(\omega)$ may then be obtained, as shown in Fig. 25, inset B. The frequency-dependence of the friction near the barrier peak may deviate from this function, and it will be interesting to investigate it for computational models, and potentially for single-molecule probes at some future time.

The anharmonic corrections to the Grote–Hynes rate for the lattice 27-mer may be calculated from Eqs. (6.27) and (6.28), which results in $p_{AN} \cong 0{\cdot}85$. The rate is thus moderately reduced from the Grote–Hynes value of $1{\cdot}57\, k^{KR}$, giving $k = 1{\cdot}33\, k^{KR}$ for the corrected rate in Eq. (6.27), in closer agreement with the Kramers value. Note that these rates are all within a factor of 2 of each other. The numerically close agreement between the rate calculated from the physics of a distribution of relaxation modes, to the Kramers value for the rate, is a good justification for the Markovian approximation assumed in earlier analyses. Envisioning protein folding as stochastic motion of a collective coordinate on an average

thermodynamic potential, governed by Langevin dynamics or a Fokker–Planck equation, is a reasonable description of the process of folding for a typical minimally frustrated protein.

However, from Fig. 26 (inset) we see that the flux through the TST dividing surface is quite spread out over a large range in the coordinate Q. This is to be expected since Q behaves as a diffusive reaction coordinate rather than a ballistic one. On the other hand, the TST dividing surface tends to be nearly orthogonal to the Grote–Hynes reaction coordinate ρ, indicating trajectories behave ballistically along this reaction coordinate. The function $f = \rho - g(\sigma)$, when interpreted as progress across the barrier, generalizes the notion of a scalar reaction coordinate such as Q. However, unlike Q, it is difficult to interpret precisely what σ means for a conformational state. The non-Markovian effective potential in Eq. (6.22) and the optimal dividing surface are shown in Fig. 26. One may infer from the considerable spread of the transition-state region along the Q coordinate that the folding transition-state ensemble does not have a well-defined value of Q, but rather includes configurations from a disperse region. A disperse distribution of experimental ϕ-values supports this description (Onuchic *et al.* 1996).

The observation that rates are well-predicted by Fokker–Planck diffusion on an average thermodynamic potential has been made in several simulation studies (Socci *et al.* 1996; Pande & Plaxco, 2001), while it is also observed that the transition states may be significantly spread out around the barrier peak (Abkevich *et al.* 1994; Onuchic *et al.* 1996; Du *et al.* 1998; Pande & Plaxco, 2001). The energy landscape theory applied here is indeed consistent with these observations.

Important effects may be seen in analyses with several reaction coordinates, particularly if the friction is anisotropic. In these cases phenomena such as saddle-point avoidance may modify the value of the barrier height as well as the prefactor. The methods may also be applied to dynamics in other condensed matter systems with rugged landscapes, e.g. RNA, protein–ligand binding, glasses, and clusters.

7. Structural and energetic heterogeneity in the folding mechanism

The wide range of folding rates for different native structures indicates that native structure is a strong determinant of at least some properties of the free-energy profile, such as the size of the folding barrier. However, native structure is not an exclusive determinant of the thermodynamics. Proteins folding to the same structure may have rates different by several orders of magnitude (Kim *et al.* 1998; Dalessio & Ropson, 2000), and may even have different folding mechanisms. For example, although the four-helix proteins Im7 and Im9 are structural homologs, wild-type Im9 folds by a two-state mechanism while Im7 folds through an *en route* intermediate (Ferguson *et al.* 1999): the free-energy landscape may fluctuate sequence to sequence for amino-acid chains that fold to the same native structure.

In this section we address the effects on folding rate and mechanism that arise from distributions of quantities. That is, we quantify a model protein in terms of the full distribution of native contact energies $\{\epsilon_i\}$, as well as the full distribution of native contact lengths $\{l_i\}$ (sequence lengths pinched off by each native contact), under the assumption that the protein under consideration is well-designed, or minimally frustrated with T_{F} reasonably larger than T_{G}. Native heterogeneity is retained explicitly, while non-native interactions are treated through an average background field – the scalar quantity b in, e.g. Eq. (5.6*c*). We are

thus isolating the effects of native heterogeneity on the folding mechanism. It has been found (Plotkin & Onuchic, 2000, 2002) that even though there is a large entropy present in the transition state of the system at T_F, there are still in fact strong dependencies of the barrier and folding mechanism on the distribution of native stability and distribution of native contact lengths. In fact local fluctuations in native stability and structure do not average out, but contribute extensively in determining properties of the folding mechanism.

A quantity such as folding temperature or folding barrier which fluctuates over an incompletely specified ensemble may have a mean that is still useful in characterizing trends as a function of one or more parameters. An example is the increase on average in folding rate, or decrease in folding barrier, as mean native contact length $\bar{l}$ (more specifically $\bar{l}/N$) is decreased (Plaxco *et al*. 1998, 2000), for which several models have been proposed (Munoz & Eaton, 1999; Fersht, 2000), and which we consider here within the theoretical framework of this section as well (see Section 7.4). The observed correlation between rates and $\bar{l}$ implies that many proteins are sufficiently well-designed such that native topology plays a role at least as important as native stability in governing folding rates and mechanism, a topic recently investigated by several authors (Alm & Baker, 1999; Munoz & Eaton, 1999; Shoemaker *et al*. 1999; Galzitskaya & Finkelstein, 1999; Shea *et al*. 1999; Riddle *et al*. 1999; Du *et al*. 1999; Fersht, 2000; Clementi *et al*. 2000a, b; Taverna & Goldstein, 2000; Maritan *et al*. 2000; Dinner & Karplus, 2001).

Here we will go beyond the first moments of the contact length distribution $\bar{l}$ and stability distribution $\bar{\epsilon}$. We investigate how the full distributions of energetics and topology as well as correlations between them affects the free-energy profile, corresponding barrier, folding rate, and overall folding mechanism. Native heterogeneity, both entropic and energetic, plays an important role in quantifying protein folding mechanisms. One can extend the analysis of thermodynamic quantities in Section 5 by using functionals rather than functions to describe folding properties which are not necessarily self-averaging, but which may depend on distributions of coupling parameters. To this end we derive in this section a simple field theory with a non-uniform order parameter to study fluctuations away from uniform ordering, through free-energy functional methods (Shoemaker *et al*. 1997, 1999; Shoemaker & Wolynes, 1999). An induced heterogeneity in the participation of candidate transition states has also been observed in Monte Carlo simulations of sequence evolution for lattice protein models, when the selection criteria involves fast folding rate (Gutin *et al*. 1995). Here we see how, from general considerations of the energy landscape theory, selecting for rate can induce heterogeneity in the transition-state ensemble. The folding barrier for a well-designed protein is maximized when the nucleus is the most diffuse. For typical values of native energies, well-designed proteins have heterogeneous funneled folding mechanisms (Radford *et al*. 1992; Bai *et al*. 1995, Boczko & Brooks, 1995; Lazaridis & Karplus, 1997, Sheinerman & Brooks, 1998).

These results are supported by several experiments in the literature, and also suggest experiments which can test the results (see Section 7.6). For example the reduction of barrier height with folding heterogeneity should be experimentally testable by measuring the dependence of folding rate for a well-designed protein on the dispersion of ϕ-values. It is important that before and after the mutation(s) the protein remains fast-folding to the native structure without 'off-pathway' intermediates, and that its native state stability remain approximately the same, perhaps by tuning environmental variables.

In the arguments below we associate reductions in the free-energy barrier $\Delta F^{\ddagger}$ to increases

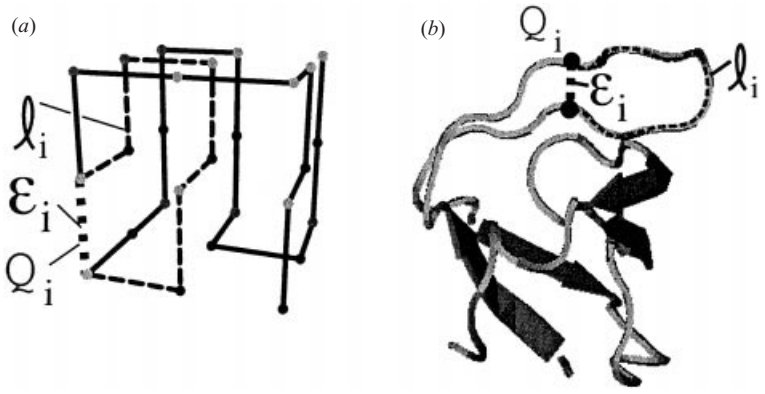

Fig. 27. (*a*) lattice, and (*b*) Rasmol representations of the native structure, characterized through the distribution of contact energies $\{\epsilon_i\}$ and contact entropies $\{s_i\}$, (defined through the distribution of loop lengths $\{l_i\}$). The probability to form contact i having energy ϵ_i and loop length l_i, at partial degrees of nativeness Q, is Q_i (Q).

in the folding rate k_F. This is true as long as the prefactor $k_0(\zeta)$ in the expression for the rate, Eqs. (4.7*b*) or (6.29), is more weakly affected than the barrier height over temperature $\Delta F^{\ddagger}/T$ under redistribution of native stability. However it has been shown (Plotkin & Onuchic, 2002) that even for perturbations in native energy large enough to kill the barrier, the T_F varies only weakly compared to the changes in barrier height, so that the ratio T_F/T_G should also not vary significantly compared to the changes in barrier height. The prefactor which is a function of T_F/T_G is then not strongly affected.

When the Hamiltonian consists of pair interactions alone, redistributions of native stability can eliminate the barrier entirely at the T_F (see Fig. 31). It is worth noting that many-body interactions which are believed to be present in real protein interactions (Horovitz & Fersht, 1992; Hao & Scheraga, 1997; Sorenson & Head-Gordon, 1998; Klimov & Thirumalai, 1998a; Lum *et al.* 1999; Takada *et al.* 1999; Prince *et al.* 1999) tend to increase the barrier height (Kolinski *et al.* 1996; Plotkin *et al.* 1997; Eastwood & Wolynes, 2001), and in their presence the barrier may be more robust to redispersement of native stability.

7.1 The general strategy

We adopt here a coarse-grained description for the native structure, and describe it by its distributions of native contact energies $\{\epsilon_i\}$ and native loop lengths or contact lengths $\{l_i\}$. Here ϵ_i is the solvent-averaged effective free energy of contact i, and l_i is the sequence length pinched off by contact i (see Fig. 27). We use a single subscript index i for labelling native contact i (rather than e.g. ij) because we are only considering effects on the particular set of native contacts for a given native structure. Non-native interactions are treated by an average field, since the protein is assumed to be well-designed to its native structure, and native interactions are then thought to be most important in determining the folding mechanism. The index i runs from 1 to M, where M is the number of residue pair contacts in the lowest energy native structure. At partial degrees of nativeness the equilibrium probability to form contact i is defined as $Q_i(Q)$. Non-uniformity in Q_i values indicates that the protein prefers to fold some regions over others.

Following the formalism used in inhomogeneous fluids (Percus, 1982; Evans, 1992) and the theory of first-order phase transitions (Gunton *et al*. 1983) we write a free-energy functional $F(\{Q_i\}, \{\epsilon_i\}, \{l_i\})$ to characterize the effects of structural and energetic heterogeneity superimposed on the overall folding funnel. This approach has been used earlier to describe domain growth in proteins (Bohr & Wolynes, 1992) and more recently as a calculational tool to compute ϕ-values (Shoemaker *et al*. 1997, 1999; Shoemaker & Wolynes, 1999).

In the functional method, all the native contact energies $\{\epsilon_i\}$ and the native loop lengths $\{l_i\}$ for a protein are initially assumed as given, and the thermal (most probable) distribution native of contact probabilities $\{Q_i^*(\{\epsilon_i\}, \{l_i\}, Q)\}$ is found by minimizing the free-energy functional $F(\{Q_i(Q)\}|\{\epsilon_i\}, \{l_i\})$ with respect to the distribution of occupation probabilities, subject to the constraint that the average probability is Q, i.e. $\Sigma_i Q_i = MQ$ (Q then parameterizes the values of the $Q_i's$). This procedure is analogous to finding the most probable distribution of occupation numbers, and thus the thermodynamics, by maximizing the microcanonical entropy for a system of particles obeying a given occupation statistics. Here the effective particles (the contacts) behave like fermions, since no more than one bond can 'occupy' a contact. The system can be understood to have a set of free energy levels obeying a distribution governed by the native structure and energies of the protein, and we seek the fraction of time (the probability) those levels are occupied given a fixed overall number of levels filled.

The free energy for a system obeying the thermal (most probable) distribution $\{Q_i^*(Q, \{\epsilon_i\}, \{l_i\})\}$ is then considered a function of the contact energies for a *fixed* native structure: $F(Q, \{\epsilon_i\}|\{l_i\})$. That is, we consider the folding free energy barrier as a functional of the interaction energies $\{\epsilon_i\}$ for a *given* native topology. The free energy depends on the energies $\{\epsilon_i\}$ both explicitly and implicitly through the thermal contact probabilities $\{Q_i^*(\{\epsilon_i\}|Q, \{l_i\})\}$. Then we can seek the special distribution of contact energies $\{\epsilon_i^*(l_i)\}$ that extremizes (minimizes or maximizes, depending on the second derivative) the thermo-dynamic folding barrier to a particular structure by finding the extremum of $F^{\ddagger}(\{\epsilon_i\}|\{l_i\})$ with respect to the contact energies ϵ_i, subject to the constraint of fixed total native energy: $\Sigma_i \epsilon_i = M\bar{\epsilon} = E_N$, i.e. while maintaining the same overall stability of the native structure. Thus we are isolating the effect of heterogeneity (as opposed to stability changes) on the folding mechanism. This distribution when substituted into the free energy gives in principle the extremum free-energy barrier as a function of native structure $F^{\ddagger}(\{l_i\})$, which might then be optimized for the fastest/slowest folding structure and its corresponding barrier. However, we will find below that in fact the only distribution of energies for which the free energy is an extremum is in fact the distribution which *maximizes* the barrier by tuning all the contact probabilities to the same value: $Q_i(Q^{\ddagger}) = Q^{\ddagger}$. In this case the coupling energies would be tuned to eliminate any information contained in the native structure, except for the mean loop length $\bar{l} = (1/M)\Sigma_i l_i$. Any perturbation away from this scenario lowers the free-energy barrier. We also examine the effects of structural dispersion on the barrier, i.e. the free energy for variable loop distribution (various native structures) but fixed coupling energies, $F(Q, \{l_i\}|\{\epsilon_i\})$, and arrive at the same conclusion: at fixed native stability, increasing structural variance (at fixed average loop length) lowers the barrier and thus speeds the rate, as long as the protein is sufficiently well-designed that the rate is governed by the free-energy barrier.

7.2 An illustrative example

We illustrate the procedure by applying it to a more trivial system – an Ising paramagnet in a non-uniform external field. The Hamiltonian for this system is

$$\mathscr{H} = -\sum_{i=1}^{N} \epsilon_i \sigma_i, \tag{7.1}$$

where $\sigma_i = \pm 1$ is the ith spin and ϵ_i is (minus) its local field energy. To obtain the free-energy functional we need an expression for the configurational entropy in terms of the spin degrees of freedom. If the field was uniform, the configurational entropy per spin $s(q)$ could be written in terms the fraction of up spins $N_+/N \equiv q$ as

$$s(q) = \frac{S(q)}{N} = \frac{1}{N} \ln \frac{N!}{(Nq)![N(1-q)]!} \cong [-q \ln q - (1-q) \ln(1-q)]. \tag{7.2}$$

Here $q = (1+\bar{\sigma})/2$ where $\bar{\sigma} = (1/N)\Sigma_i \sigma_i$ is the average magnetization per site. However if the field (or the strength of the moment) varies from site to site, so will the equilibrium value of the spin. To allow for this the entropy per spin must be written in terms of $q_i = (1+\sigma_i)/2$, and the total entropy is then a functional $S(\{q_i\})$. The free-energy functional is then

$$F(\{\sigma_i\}, \{\epsilon_i\}) = \sum_{i=1}^{N} \left[-\epsilon_i \sigma_i + T \left(\frac{1+\sigma_i}{2} \ln \frac{1+\sigma_i}{2} + \frac{1-\sigma_i}{2} \ln \frac{1-\sigma_i}{2} \right) \right]. \tag{7.3}$$

The equilibrium values of the spins σ_i^* are obtained by finding the extremum of the free energy, subject to a fixed overall magnetization $\mathscr{M} = \Sigma_i \sigma_i$:

$$\frac{\delta}{\delta \sigma_i} \left(F + h_M \sum_j \sigma_j \right) = 0. \tag{7.4}$$

This leads to the equation

$$\sigma_i^* = \tanh \left(\frac{\epsilon_i + h_M}{T} \right) \tag{7.5}$$

for the equilibrium values of the spins. Each spin follows its local field according to the well-known Brillion function (for spin $\frac{1}{2}$). The Lagrange multiplier h_M is determined from the sum $\Sigma_i \sigma_i^* = \mathscr{M}$. For a uniform field, $h_{\mathrm{M}} = T \tanh^{-1} (\mathscr{M}/N) - \epsilon$. The second variation of F is positive indicating the free energy is minimized and σ_i^* are the thermal equilibrium values:

$$\left. \frac{\delta^2 F}{\delta \sigma_i \delta \sigma_j} \right|_{\{\sigma_i^*\}} = \delta_{ij} \frac{T}{1-\sigma_i^{*2}} > 0. \tag{7.6}$$

Substituting $\sigma^*{}_i(\epsilon_i)$ [Eq. (7.5)] back into the free-energy functional [Eq. (7.3)] gives the free energy in terms of the coupling energies $\{\epsilon_i\}$:

$$\frac{F(\{\epsilon_i\})}{T} = -N \ln 2 - \sum_{i=1}^{N} \ln \left[\cosh \left(\frac{\epsilon_i + h_M}{T} \right) \right] + \frac{h_M \mathscr{M}}{T}. \tag{7.7}$$

This free energy is equivalent to the form obtained from the partition function in the canonical ensemble.

Now we can seek the set of fields ϵ_i^* that extremizes the free energy subject to a given total coupling energy $E = \Sigma_i \epsilon_i$:

$$\frac{\delta}{\delta \epsilon_i}\left(F + p\sum_j \epsilon_j \right) = 0. \tag{7.8}$$

This yields the condition that all the spins have the same value and thus that the field be uniform:

$$\sigma_i(\epsilon_i^*) = p, \tag{7.9}$$

$$\epsilon_i^* = \epsilon. \tag{7.10}$$

However, second variation of the free energy gives

$$\left.\frac{\delta^2 F}{\delta \epsilon_j \delta \epsilon_i}\right|_{\{\epsilon_i\}=\{\epsilon\}} = -\delta_{ij}\frac{1}{T}\operatorname{sech}^2\left(\frac{\epsilon + h_M}{T}\right), \tag{7.11}$$

which is negative, indicating this choice of coupling energies *maximizes* the free energy. Thus any perturbations away from the uniform field will lower the free energy. Although the entropy functional is much more complicated for proteins, we find that there too the only free energy extremum is a maximum.

7.3 Free-energy functional

We refer the interested reader to Plotkin & Onuchic (2000, 2002), for a derivation, and give the result here for the free energy for a fast-folding protein which includes heterogeneity in the folding mechanism:

$$F(\{Q_i(Q)\}\,|\,\{\epsilon_i\}, \{l_i\}) = F_{\mathrm{MF}}(Q, \bar{\epsilon}, \bar{l}) + \delta F(\{\delta Q_i\}\,|\,\{\delta\epsilon_i\}, \{\delta l_i\}). \tag{7.12}$$

We have written the total free energy here in terms of a mean-field term plus a fluctuation due to variations in energy, loop length, and contact probability. The free energy that we saw earlier in Eqs. (5.7), (5.8) is generalized here to account for these variations, and for a finite average mean return length $\bar{l}$ for native contacts. A distribution of native stabilizing interactions is introduced directly into the Hamiltonian, much like the coupling energies ϵ_i were introduced into the Hamiltonian in the last section. Variations in mean return length are accounted for by assuming a modified Flory law for the entropy of loop closure:

$$s_i(l_i, \{Q_k\}) \approx \tfrac{3}{2}\ln\left(\frac{a}{l_{\mathrm{eff}}(l_i, Q)}\right). \tag{7.13}$$

Here $l_{\mathrm{eff}}(l_i, Q)$ is an effective loop length that depends only on the local 'bare' loop length l_i, and the mean contact probability field Q present. This approximation is analogous to the Hartree approximation used in the theory of metals.

Equation (7.13) is consistent with the constraint that the conformational entropy be a state function, and so have zero curl:

$$\frac{\partial s_j}{\partial Q_i}(l_j, \{Q_k\}) = \frac{\partial s_i}{\partial Q_j}(l_i, \{Q_k\}) \quad \text{for } i \neq j. \tag{7.14}$$

After the calculation (Plotkin & Onuchic, 2002) the mean-field entropy loss due to contact formation becomes a function of $\bar{l}$. This produces a dependence of the free-energy barrier on $\bar{l}$, as shown in Fig. 29. The parameter $\bar{l}$ here is proportional to a parameter known as contact order (Plaxco *et al.* 1998, 2000), which is known to correlate very strongly with folding rates.

The fluctuation term in Eq. (7.12) is in fact given by

$$\frac{\delta F}{M}\left(\{\delta Q_i\}\,|\,\{\delta\epsilon_i\},\{\delta l_i\}\right)=\langle\delta Q\delta\epsilon\rangle+T\lambda(Q)\left\langle Q_i\ln\frac{Q_i}{Q}+(1-Q_i)\ln\frac{1-Q_i}{1-Q}\right\rangle+\tfrac{3}{2}T\langle\delta Q\,\delta\ln l\rangle, \tag{7.15}$$

where the angle brackets indicate averages over the native contacts. For example

$$\langle\delta Q\,\delta\ln l\rangle\equiv\frac{1}{M}\sum_{i=1}^{M}(Q_i-Q)(\ln l_i-\ln\bar{l}).$$

Equations (7.12) and (7.15) describe the free energy for an arbitrary distribution of contact probabilities $\{Q_i(Q)\}$. The most likely distribution, $Q_i^*(Q)$, i.e. the thermal distribution, is obtained by minimizing the free energy subject to the constraint $\Sigma_i Q_i(Q)=MQ$. This yields a Fermi distribution for the contact occupation probabilities, with an effective 'chemical potential' determined by the mean occupation probability Q.

We can then vary the values of $\{\epsilon_i\}$ at fixed overall stability (fixed total native energy) $\Sigma_j\epsilon_j=E_{\rm N}$, to find the distribution $\{\epsilon_i^*(\{l_j\})\}$ that extremizes the free-energy barrier, i.e. that satisfies

$$\sum_i\left[\frac{\delta\Delta F^{+}}{\delta\epsilon_i}-p\right]\delta\epsilon_i=0 \tag{7.16}$$

for arbitrary and independent variations $\delta\epsilon_i$ in the energies. The Lagrange multiplier p imposes the constraint that the total native energy $E_{\rm N}$ is constant. The minimization results in:

$$Q_i(Q^{+},\epsilon_i^{*},l_i)=Q^{+}, \tag{7.17}$$

meaning that this folding scenario is that of a symmetric funnel: the protein is equally likely to order from any place within it. Equation (7.17) should be compared with Eq. (7.9).

Evaluating the second derivative stability matrix shows $Q_i=Q^{+}$ in Eq. (1.17) to be an unstable maximum:

$$\left(\frac{\delta^2\Delta F^{+}}{\delta\epsilon_j\delta\epsilon_i}\right)_{\epsilon_i^*,\epsilon_j^*}=\frac{\partial Q_i}{\partial\epsilon_j}\cong-\delta_{ij}\frac{Q^{+}(1-Q^{+})}{\lambda^{+}T}, \tag{7.18}$$

which is negative, meaning that tuning the energies so that $Q_i=Q^{+}$ maximizes the free energy at the barrier peak [cf. with Eq. (7.11)]. (See Fig. 28.)

Thus the free energy at the barrier peak becomes

$$\Delta F^{+}\{\epsilon_i^{*}+\delta\epsilon_i\}\cong\Delta F_{\rm MF}^{+}-M\frac{Q^{+}(1-Q^{+})}{2\lambda^{+}T}\,\overline{\delta\epsilon^2}. \tag{7.19}$$

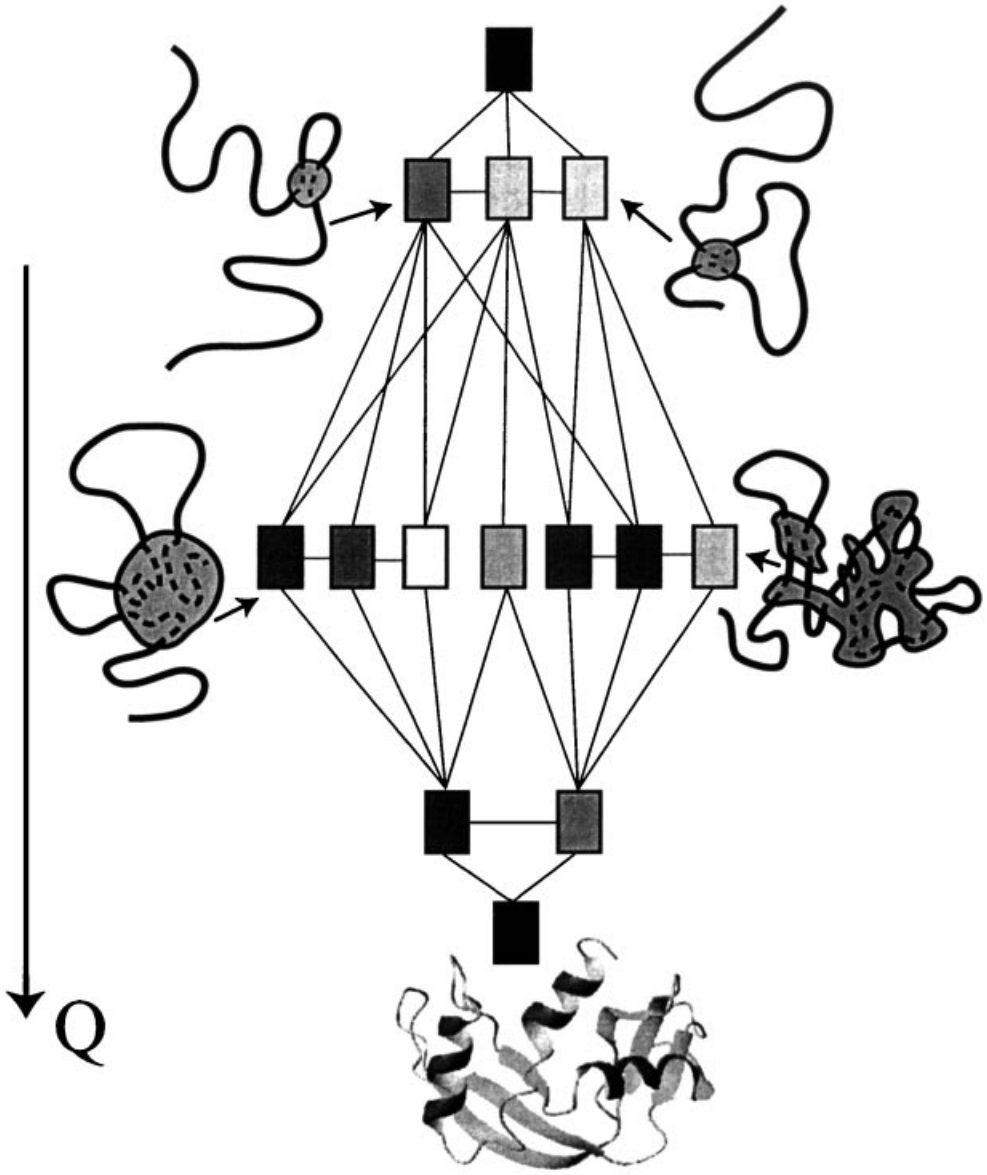

Fig. 28. Illustration of folding heterogeneity. At partial degrees of nativeness, a protein adopts conformations containing various native cores as indicated schematically (the core may be globular or ramified). These native cores are occupied with varying probabilities depending on their free energies (larger probability is indicated here as a darker shade of grey). As folding heterogeneity increases, the route entropy at degree of nativeness Q decreases. However the energy at Q always decreases, and the polymer halo entropy increases, such so that the free energy at Q goes down. See also Burton *et al.* (1998) for an illustration showing heterogeneity specifically for λ-repressor within the diffusion–collision model.

For an energetic standard deviation of about a $k_B T$ from the optimal distribution, the barrier goes down by about $\sim N k_B T/2$. The barrier governed rate thus increases with native energetic heterogeneity as

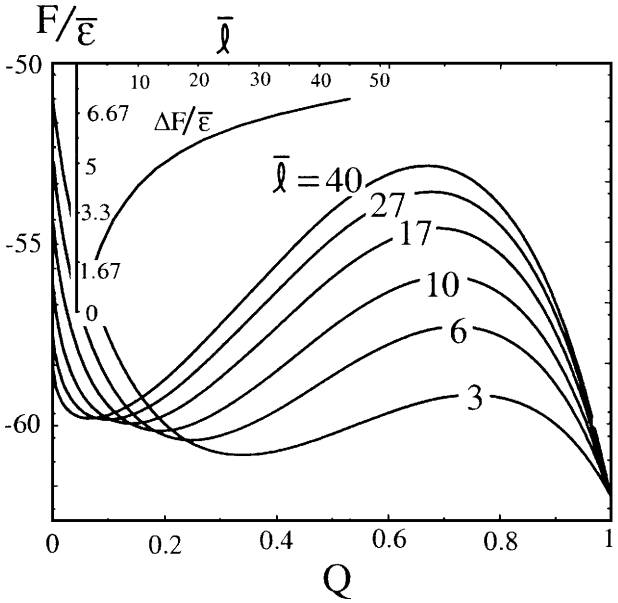

Fig. 29. Dependence of the free-energy profile $F(Q)$ at T_F on the mean loop length $\bar{l}$, for the analytic model with length $N = 50$, $l_i = \bar{l}$, and $\epsilon_i = \bar{\epsilon}$. The value of $\bar{l}$ labels each curve. The barrier undergoes an increase that is stronger initially (see inset). The inset plots the barrier height as a function of $\bar{l}$, in units of $\bar{\epsilon}$. The trend in barrier height with $\bar{l}$ shown here is a lower limit to the full theoretical dependence given in Eq. (7.22) (see text).

$$k = k_0 \exp\left(-\frac{\Delta F^{\ddagger}}{T}\right) = k_{\text{homo}} \exp\left(Q^{\ddagger}(1-Q^{\ddagger})\frac{M\overline{\delta\epsilon^2}}{2\lambda^{\ddagger}T^2}\right), \tag{7.20}$$

where k_{homo} is the rate in the absence of native heterogeneity.

The theory also allows us to investigate the effects of native structural variance on the barrier, as well as the correlations between structure and energetics. Considering perturbations in the free energy of a homogeneous system with $l_i = \bar{l}$, $\epsilon_i = \bar{\epsilon}$, $Q_i = Q^{\ddagger}$ by letting $l_i = \bar{l} + \delta l_i$ and $\epsilon_i = \bar{\epsilon} + \delta\epsilon_i$, and expanding to second order in the perturbations $\delta\epsilon$ and δl results in (Plotkin & Onuchic, 2000, 2002):

$$\Delta F^{\ddagger}\{\bar{\epsilon}+\delta\epsilon_i, \bar{l}+\delta l_i\} = \Delta F^{\ddagger 0}\{\bar{\epsilon}, \bar{l}\} - M\frac{Q^{\ddagger}(1-Q^{\ddagger})}{2\lambda^{\ddagger}T}\overline{\delta\epsilon^2}$$
$$- MT\frac{9}{8}\frac{Q^{\ddagger}(1-Q^{\ddagger})}{\lambda^{\ddagger}}\frac{\overline{\delta l^2}}{\bar{l}^2} - M\frac{3}{4}\frac{Q^{\ddagger}(1-Q^{\ddagger})}{\lambda^{\ddagger}}\frac{\overline{\delta l\delta\epsilon}}{\bar{l}}. \tag{7.21}$$

The first term on the right-hand side is the mean-field free-energy barrier. The second term on the right-hand side describes the lowering of the barrier with random energetic variance, and the third term indicates that structural dispersion (fluctuations from the mean native loop length) also lowers the barrier. The fourth term indicates that the free-energy barrier is additionally lowered in the model when shorter range contacts become stronger energetically ($\delta l_i < 0$ and $\delta\epsilon_i < 0$) or longer range contacts become weaker energetically ($\delta l_i > 0$ and $\delta\epsilon_i > 0$). This means in general that the free energy barrier is additionally lowered when fluctuations are correlated so as to further increase the variance in contact participations. Note again that all reductions in free energy due to structural and/or energetic heterogeneity are second order effects, and scale extensively with system size.

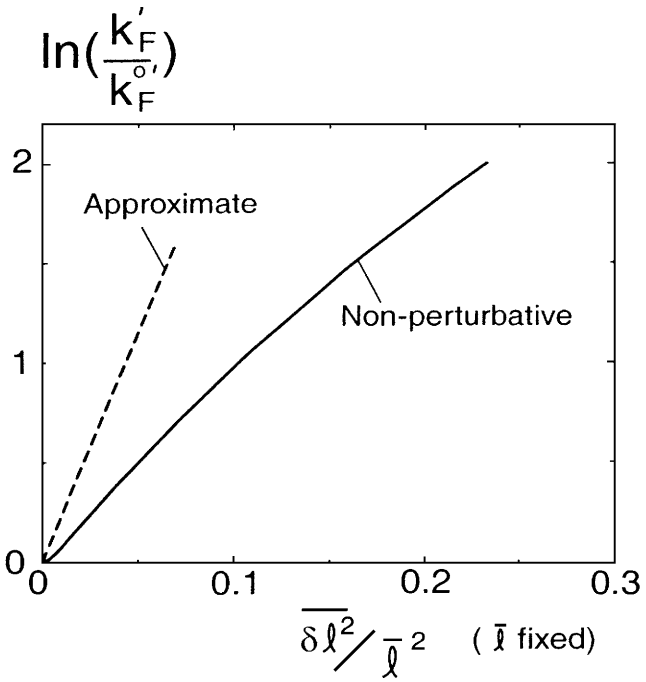

Fig. 30. Log of the ratio of rates (here taken to be equivalent to the difference in barrier heights) as a function of structural variance $\overline{\delta l^2}$ at fixed $\bar{l}$, obtained in the theory by following the recipe in Section 7.4. - - -, Approximate perturbation result using Eq. (7.22). ——, Full non-perturbative result from Eqs. (7.12) and (7.15), which accounts for changes in the unfolded free energy with increasing variance. The barrier is calculated at T_F, where T_F changes only mildly with $\overline{\delta l^2}$ until the barrier height approaches zero at $\overline{\delta l^2}/\bar{l}^2 \approx 0{\cdot}25$.

7.4 Dependence of the barrier height on mean loop length (contact order) and structural variance

Experimental evidence has shown a strong correlation of folding rate with a quantity in our model equal to the mean loop length divided by the total chain length (Plaxco *et al.* 1998, 2000). Since no strong correlation with N is observed experimentally at least for smaller proteins, we are interested in testing if the barrier height in our model correlates with $\bar{l}$, at fixed N.

We seek the change in free energy δF upon a change in the quantity $(1/M)\Sigma_i l_i$. This can be found by utilizing the directional derivative to yield (Plotkin & Onuchic, 2002):

$$\frac{\partial F}{\partial l} = -T\frac{\partial S_{\text{bond}}}{\partial \bar{l}} = \frac{3}{2}\frac{MT}{(\bar{l}-1)^2}\left[\ln(1+(\bar{l}-1)Q) - Q\ln\bar{l}\right] + \tfrac{3}{2}MT\left\langle\frac{\delta Q}{l}\right\rangle. \tag{7.22}$$

The first term in Eq. (7.22) is always positive for $Q > 0$. The second term weights loops with smaller l_i more heavily, and for these loops $\delta Q > 0$, so the second term is always positive when entropic effects are considered alone. Moreover the whole expression is zero when $Q = 0$, so we conclude that the effect of increasing the mean loop length is to increase the barrier height $\Delta F^{\ddagger}$. This effect is illustrated in Fig. 29 for the simple case where $l_i = \bar{l}$, i.e. where the second term in Eq. (7.22) is zero. This is a lower limit to the actual increase in barrier. As Eq. (7.22) implies, the change in barrier height with mean loop length is an

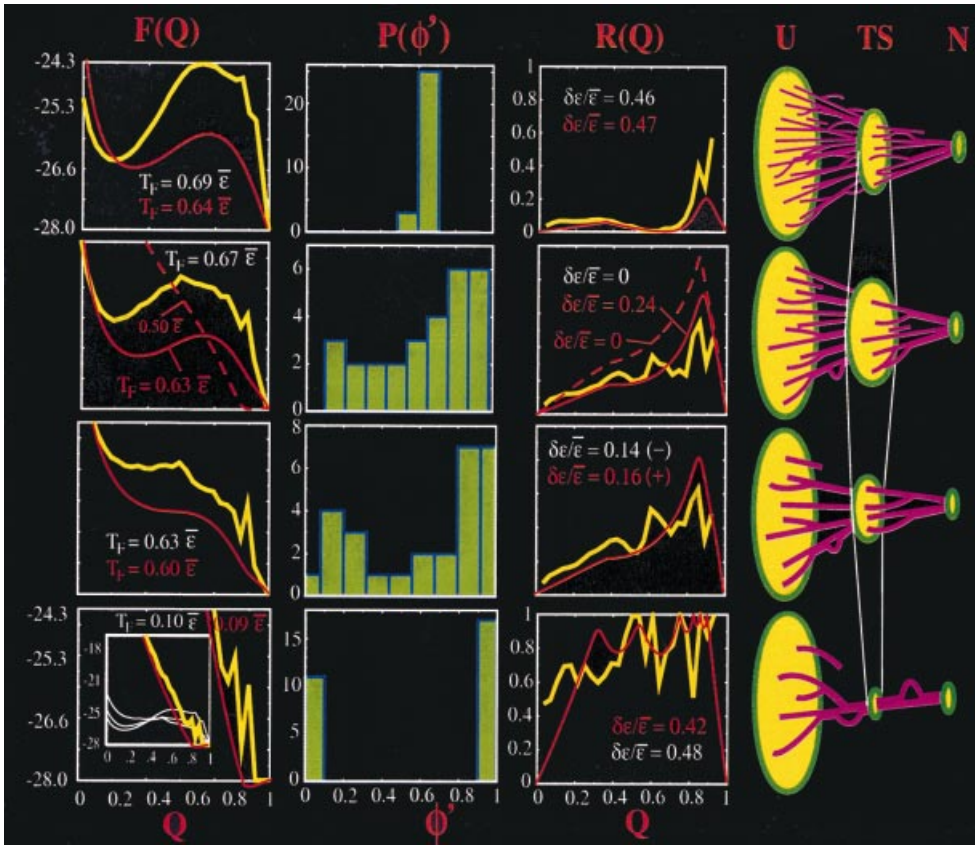

Fig. 31. The effects on folding barriers and mechanism, as heterogeneity in contact participation is increased top to bottom (see text).

entropic effect in the model; proteins with native structures having larger mean loop length have lower entropy near the transition state.

Inspection of the third term on the right-hand side of Eq. (7.21) reveals that the folding barrier is lower for structures with larger variance in loop energies $\overline{\delta l^2}$, given the structures have approximately the same $\bar{l}$. Figure 30 shows the increase on average in folding rate for structures having larger variance in loop lengths. Structural variance is generated here by letting the loop lengths be given by $l_i = \bar{l} + \alpha(l_i^0 - \bar{l})$ where $\bar{l} \cong 9{\cdot}14$ and l_i^0 is taken from the loop length distribution of the structure in Fig. 27*a*, and α is a parameter allowed to vary from zero to one. Following this recipe the mean loop length $\bar{l}$ remains unchanged, but the structural variances $\overline{\delta l^2}$ increases.

7.5 Illustrations using lattice model proteins and functional theory

We illustrate in Figure 31 the general effects of introducing heterogeneity to a model system. Results are shown for a Gō protein, modeled with the free-energy functional theory using the loop-length distribution of the lattice structure of Fig. 27*a*, and also simulated directly on the lattice (Plotkin & Onuchic, 2000). Coupling energies were chosen by first running a simulated annealing algorithm to find the set of native energies $\{\epsilon_i^*\}$ that makes all the contact

probabilities equal at the barrier peak: $Q_i(\{\epsilon_i^*\}) = Q^{\ddagger}$. Energies are always constrained to sum to a fixed total native energy: $\Sigma_i \epsilon_i = M\bar{\epsilon}$, i.e. overall stability is fixed. Here $M = 28$ and $\bar{\epsilon} = 1$. Energies are then relaxed from $\{\epsilon_i^*\}$ by letting $\epsilon_i = \epsilon_i^* + \alpha(\bar{\epsilon} - \epsilon_i^*)$.

Heterogeneity in contact probability is increased from top to bottom in Fig. 31. The effects on barrier height $F^{\ddagger}$, folding temperature T_F, and folding heterogeneity are summarized here. In Fig. 31, simulation results to the *same* native structure (cf. Fig. 27*a*) are in yellow and the analytic theory is shown in red. In the top row of Fig. 31, energies are tuned for both simulation and theory to fully symmetrize the funnel: $Q_i(\epsilon_i^*) = Q$. In the second row, energies are then relaxed – in the simulation results they are all equal: $\epsilon_i = \bar{\epsilon}$; in the theory, energies are relaxed the same way until a comparable T_F is achieved. In the third row, energies are then further tuned to a distribution $\epsilon_i \cong \epsilon_i^0$ that kills the barrier (there are many such distributions – all that is necessary is sufficient contact heterogeneity). The top 3 rows have many routes to the native structure. In the last row, energies are tuned to induce a single or a few specific routes for folding. The energies always sum to E_N.

The free-energy profile $F(Q)$ (in units of $\bar{\epsilon}$) is plotted in the left column at T_F. Curves are red for the theory, yellow for the simulation. The next column shows the distribution of thermodynamic contact probabilities $Q_i(Q^{\ddagger}) = \phi'$ at the barrier peak, taken from the simulations. The next column shows a measure of how single-route-like folding is ($\mathscr{R}(Q) = \langle \delta Q^2 \rangle / Q(1-Q)$) by giving the normalized fluctuations in contact probability. The dispersion in native energies required to induce the scenario of that row is also given. Here the route measure is taken at the T_F; at lower temperatures the route measure tends to increase. The right column shows schematically the different folding routes as heterogeneity is increased, from a maximum number of routes through $Q^{\ddagger}$ to essentially just one route. In the uniform funnel (top row), we can see first that $P(\phi')$ is a delta function (all contacts have the same probability of formation at the barrier peak: $Q_i \approx Q^{\ddagger} \approx 0{\cdot}6$) and $\mathscr{R}(Q^{\ddagger}) = 0$, so ordering at the barrier peak is essentially homogeneous. The number of routes through the bottleneck is maximized, as drawn schematically on the right. The free-energy barrier is maximized [Eq. (7.19)], and T_F at fixed native energy is maximized. T_F in the simulation is defined as the temperature where the native state ($Q = 1$) is occupied 50 % of the time. Thus for this largest barrier scenario, conformational fluctuations around the native state are most dramatically reduced. In the theory, at T_F the probability for $Q \geqslant Q_{cut} = 0{\cdot}8$ is 0·5 (this criterion is only weakly dependent on the value Q_{cut}, at least for the top 3 rows). A very large dispersion in energies is required to induce the scenario in the top row; some contact energies are nearly zero, others are several times stronger than the average.

In the funnel with constant native interaction energies (second row), the barrier height is roughly halved while hardly changing T_F, for the following reason. In a Gō model, as the contact energies are relaxed from $\{\epsilon_i^*\}$ to a uniform value $\epsilon_i = \bar{\epsilon}$, the energy of the transition state is essentially constant: initially the energy is $E(Q^{\ddagger}) = \Sigma_i Q_i^*(Q^{\ddagger})\epsilon_i^* = Q\Sigma_i \epsilon_i^* = QE_N$, and as the contact energies are relaxed to a uniform value, the energy of the transition state approaches $E(Q^{\ddagger}) = \Sigma_i Q_i \bar{\epsilon} = \bar{\epsilon}\Sigma_i Q_i = QE_N$ once again. However the transition-state entropy increases and obtains its maximal value when $\epsilon_i = \bar{\epsilon}$, for the following reason. For a Gō-like model, when $\epsilon_i = \bar{\epsilon}$, the probability of occupying a microstate at $Q^{\ddagger}$ is

$$p_i = \frac{e^{-E_i(Q^{\ddagger})/T}}{Z(Q^{\ddagger})} = \frac{e^{-Q^{\ddagger}E_N/T}}{\sum_i e^{-Q^{\ddagger}E_N/T}} = \frac{1}{\Omega(Q^{\ddagger})}, \tag{7.23}$$

where $\mathbf{\Omega}(\mathcal{Q}^{\ddagger})$ is the total number of conformational states at $\mathcal{Q}^{\ddagger}$. The thermal entropy is then

$$S = -\sum_i p_i \ln p_i = \ln \mathbf{\Omega}(\mathcal{Q}^{\ddagger}) \tag{7.24}$$

which equals the conformational entropy – the largest possible value of the entropy. So the barrier initially decreases because the total entropy of the bottleneck increases (drawn schematically on the right).

The distribution $P(\phi')$ is broad indicating inhomogeneity in the transition state, due solely in this scenario to the topology of the native structure since all contacts are equivalent energetically. Routing is more pronounced: when $\epsilon_i = \bar{\epsilon}$, $\mathcal{R}(\mathcal{Q})$ is measure of the intrinsic fluctuations in order due to the natural inhomogeneity present in the native structure. Different structures will have different profiles and it will be interesting to see how this measure of structure couples with thermodynamics and kinetics of folding. Loops and dead ends in the schematic drawings are used to illustrate local decreases and increases in $\mathcal{R}(\mathcal{Q})$. The solid curves presented for the theory are shown for a reduction in T_{F} comparable to the simulations. There is still some energetic heterogeneity present as indicated. When $\epsilon_i = \bar{\epsilon}$ in the theory (dashed curves), the fluctuations in $\mathcal{Q}_i$ are larger than the simulation values, and the entropic heterogeneity is sufficient to kill the barrier – hence the downhill dashed curve. The free-energy barrier results from a cancellation of large terms and is significantly more sensititve than intensive parameters such as route measure $\mathcal{R}(\mathcal{Q})$. As folding heterogeneity continues to increase, the free-energy barrier continues to decrease until some sets of energies $\{\epsilon_i^0\}$ where the barrier at T_{F} vanishes entirely (third row). All the while the folding transition temperature T_{F} decreases only $\sim 10\,\%$, so that slowing of dynamics (as T_{F} approaches T_{G}) is not a major factor. At this point the ϕ' distribution at the original barrier position $\mathcal{Q}^{\ddagger}(\bar{\epsilon})$ is essentially bi-modal. A relatively small amount of energetic heterogeneity is needed to kill the barrier at T_{F}: for the simulations $\delta\epsilon$ is such that $\alpha > 1$, for the theory $\alpha < 1$. Numbers are shown in the figure of the route measure. There are still many routes to the native state since $\mathcal{R}(\mathcal{Q}^{\ddagger}) \approx 0{\cdot}3$–$0{\cdot}4$, but some contacts are nearly fully formed in the transition state (some $\phi' \cong 1$).

As the energies continue to be perturbed to values that cause folding to occur by a single dominant route (bottom row), folding becomes strongly downhill at the transition temperature, which drops more sharply towards T_{G}. Here, to induce a single pathway T_{F} must be decreased to about $\frac{1}{4}$ the putative estimate to T_{G} [approximately $T_{\mathrm{F}}(\{\bar{\epsilon}\})/1{\cdot}6$]. In this scenario, the actual shape of the free-energy profile depends strongly on which route the system is tuned to. Non-native interactions not included here will become important, and dynamics would become slow. Contact participation at intermediate $\mathcal{Q}$ is essentially one or zero, and the route measure is essentially one. The energetic heterogeneity necessary to achieve this scenario is agian very large – comparable to what is needed to achieve a uniform funnel.

7.6 Connections of functional theory with experiments

Several experiments support these results on folding heterogeneity. Enhancement of folding rates by weighting entropically likely contacts has been observed in *Escherichia coli* Che Y (Viguera *et al.* 1996). Depending on the variance of native interactions and how native interaction strength correlates with the entropic likelihood of contact formation, sequences may be designed to fold both faster or slower to the same structure as a wild-type sequence.

Enhancements or suppressions of folding rate to a given structure due to changes in sequence are modeled in the functional theory through changes in native interactions. A minimally frustrated sequence may fold to a given native structure by a variety of folding mechanisms, including through both on and off pathway intermediates. Thus for example folding in Im7 and Im9 may possibly initiate from different places within the native structure depending on the distribution of native stabilizing interactions (Ferguson *et al*. 1999). Folding in the IgG binding domain of protein L may tend to initiate from a specific region of higher stability, indiscernible from the apparently symmetric native structure (Kim *et al*. 2000); contact formation probability at the transition state depends on both energy and entropy. For a large range of native energy distributions, barrier heights, and corresponding rates, there are many routes to the native structure. Folding rates in mutant proteins that exceed those of the wild type have been studied in several experiments (Viguera *et al*. 1996; Munoz & Serrano, 1996; Hagen *et al*. 1996; Kim *et al*. 1998; Brown & Sauer, 1999). Folding rates often increase due to increased stabilization. Here we see how effects due to a heterogeneous transition state can be important as well, and can be understood by applying general principles of the energy landscape. Folding rates in the theory were seen to increase with the variance in contact formation probability, a thermodynamic quantity closely related to the dispersion in experimental ϕ values. The general trend of reduced rate with larger contact order (Plaxco *et al*. 1998) is captured by the theory fairly well, but the trend is weaker than in the experiments. We found that additionally, for fixed contact order, folding rate is expected to increase with larger variance in the contact lengths which constitute the native structure.

Also recently observed is the intriguing discovery that, at least in some proteins such as S6, native stabilizing interactions are tuned to optimize folding cooperativity and reduce conformational fluctuations in the native state, by maximizing the folding barrier at the expense of the folding rate (Lindberg & Oliveberg, 2002). These observations are fully consistent with the theory. That is, for S6 there is an evolutionary bias in the wild-type protein towards row 1 of Fig. 31, by correlating strong contact energies with longer loop lengths. The loop lengths can be inverted, with long loops becoming short ones, by circular permutating the S6 protein (Lindberg & Oliveberg, 2002). When this is done the strong native interactions have short loop lengths, which polarizes the transition state. The result is a faster folding protein with a less rigid native state, somewhere between rows 2 and 3 of Fig. 31. It is also worth mentioning that the bias towards a uniform folding mechanism bolsters
the use of Q as a reaction coordinate at least for some wild-type proteins.

The experimental results of the Oliveberg group on S6 in fact give a possible explanation for the reduced transition-state drift in wild-type CI2, compared with CI2 mutants (Oliveberg *et al*. 1998). The reduced drift seen in some wild-type proteins may come from an evolutionary tendency for some proteins to fold cooperatively with higher barriers, whose peak positions are thus naturally more robust to environmental perturbations.

The phenomenon that fluctuations in native contact energies contribute extensively to the free-energy landscape indicates that the prediction of numerical values for folding rates and mechanisms from approximate energy functions may be even more difficult than originally suspected, i.e. even if systematic error in the calculation of potentials is eliminated, $\mathcal{O}(\mathcal{N})$ corrections to the folding barrier may still remain.

It is encouraging that such a general theoretical framework can be used to explain the effects of heterogeneity in native stability and structural topology on folding. Quantities such

as folding rates, transition temperatures, and the folding mechanism may all be investigated within this framework. Such a theory should be a useful guide in interpreting and predicting future experimental results on many fast-folding proteins.

8. Conclusions and future prospects

An understanding of protein folding provides a link between the genetic code in the DNA molecule and the structure and function of a living organism. While a description of protein folding is impeded by the complexity of the process, much of this complexity can in fact be exploited by taking a statistical approach to the energetics of protein conformation, that is to the energy landscape. The energy landscape approach explains when and why self-averaging behavior will govern the folding process, and when sequence-specific behavior, such as specific folding pathways or intermediates, should be observed.

Proteins provide a unique system to inspire investigations into deeper theoretical issues. We began by investigating the thermodynamic phases of a RHP, which included a replica-symmetry breaking phase where the entropy vanishes. We constructed the phase diagram, which can include a microphase-separated region and a micro-phase separated glass. We later saw the analog of this in the phase diagram of a model protein, which contained folded and folded-glass phases.

We then studied the theory of polymers under topological constraints, and found that the weakly constrained and strongly constrained regimes demanded different approaches. The polymer theory was then applied towards an in-depth study of the replica-symmetry breaking transition that took into account higher order correlations not included in the REM. The effect of higher order correlations is to round the glass transition in the following sense. While the glass transition temperature is only weakly affected, there is significant residual entropy below the transition temperature, arising from the entropy contained in ergodically localized basins, which shrink in phases-space to one conformational state as the temperature is lowered. Levinthal searches on a correlated landscape are significantly faster than the numbers typically taken from back of the envelope calculations.

The kinetics in a disordered system was investigated by applying the statistics of microscopic escape processes to the diffusion coefficient appearing in a Fokker–Planck equation for the probability distribution of an order parameter. Thus the friction appearing in the prefactor of the folding rate equation was calculated. A new transition temperature, distinct from the thermodynamic glass temperature, appeared from a study of disordered dynamics. At this temperature, reconfigurational barriers for thermally occupied states disappear.

The studies of polymer entropy and many-body interactions came together in a theory for folding thermodynamics. Many-body interactions are believed to be present generically when solvent or side-chain degrees of freedom are integrated out. The effects on folding rate and mechanism as a function of the cooperativity in the interactions were studied. A kind of T_G, where the system folds through only one or a few routes, arose when native heterogeneity was sufficiently large. As we saw in Part I, heterogeneity in the entropies of partially native cores could also contribute towards increasing this temperature. For a given set of allowable interaction energies in the Hamiltonian, the low energy of the native state tends to reduce the variance of the stabilizing interaction energies in that state.

Experimental results on transition-state drift compared favorably with predictions from the theory. The theory gives a framework for interpreting magnitudes of the drift, and why

different measurements can yield different transition-state values and drifts. The functional theory developed later in the review also provides an explanation as to why mutants of a wild-type protein which fold to the same native structure can have larger transition-state drift.

The Kramers theory for folding rates can be tested by applying multi-dimensional TST to the protein folding data taken from lattice simulations. Only small modifications in the rate are observed, but the transition-state region is seen to be significantly spread out in the fraction of native contacts, indicating that transition-state configurations can have large variations in the amount of native structure present.

By generalizing the mean-field theory of folding to include fluctuations in the order parameter, one may deduce universal consequences of the effects of heterogeneity on folding rate and mechanism. Specifically, a protein with its native stabilizing interactions tuned to induce a uniform folding mechanism tends to have the largest folding barrier at a given stability. This reduces conformational fluctuations in the native state, and can be important for function or to prevent aggregation arising from locally unfolded regions. Mutants or permutants which have a more heterogeneous folding mechanism with a more polarized transition state have smaller barriers, are faster folding, and have larger conformational fluctuations in the native state.

Structures having approximately the same contact order but larger variance in native loop lengths should tend to fold faster. Imposing larger random energetic heterogeneity in the native stabilizing interactions, uncorrelated with the native structure, should also lower the folding barrier at fixed stability.

The study of protein folding has undergone a dramatic transformation over approximately the last decade, evolving to include a diverse group of scientists who study equally diverse aspects of this self-organization process. However, it is now apparent that for many parts of the problem, theory, simulation, and experiment are all currently in a process of convergence to make the study of protein folding a truly quantitative branch of science.

9. Acknowledgments

The nucleus for this review was the Ph.D. thesis of S. S. P. under Peter Wolynes. We are grateful to Peter Wolynes and Jin Wang for numerous insightful and enjoyable discussions. This work was funded by NSF Bio-Informatics felllowship DBI9974199 and NSF Grant MCB0084797.

Appendix A. Table of common symbols

Symbol	Definition	Equation
N	Total number of residues in the protein or heteropolymer chain	(2.3)
M	Total number of contacts in a given configuration	(2.29)
$\tilde{\varkappa}$	Average number of contacts per residue	(2.3)
$\bar{\epsilon}$	Average attraction energy per contact (in section 7, mean native contact energy)	(2.4), (7.21)
s_0	Conformational entropy per residue, in units of Boltzmann's constant k_B	(2.3)
ν	Number of conformational states per residue	(2.10), (2.26)
η	Packing fraction of the polymer	(2.22), (2.26)
b	Standard deviation of the energies of contacts	(2.3)
T	Temperature in units of Boltzmann's constant k_B	(2.6*a*)
T_C	Collapse temperature	(2.17)
T_F	Folding temperature	(5.9)
T_G	Glass temperarture	(2.7)
T_A	Temperature above which reconfigurational barriers disappear	(4.27)
$\bar{T}$	Reduced temperature in units of the glass temperature	(4.26)
$\lambda(q)$	Parameter accounting for a reduced number of folding nuclei in a polymer	(2.31*b*)
q	Fraction of contacts in common with a given conformational state	(2.25)
$\underset{\sim}{Q}$	Fraction of contacts in common with the native state	(5.5)
p	Number of contacts in a cluster contributing to a many-body Hamiltonian	(3.4), (5.5)
k_F	Forward folding rate	(4.7*b*)
$\bar{\tau}_F$	Mean first passage time to fold	(4.6)
$\langle\tau\rangle$	Mean reconfiguration time on a rugged landscape	(4.8), (4.25)
τ_0	Rouse–Zimm reconfigurational time scale	(4.24), (4.26)
E_{GS}	Random heteropolymer ground state energy	(2.4)
E_N	Energy in the native conformational state	(5.5)
ϵ_N	Average energy per native contact ($\bar{\epsilon}$ in Section 7)	(5.6*a*)
b_N	Standard deviation of the energies of native contacts	(5.5)
c	Fraction of total possible contacts present in a given conformation	(5.6*a*)
$D(\underset{\sim}{Q}, T)$	Configurational diffusion coefficient	(4.6), (4.8)
$D(\underset{\sim}{Q}, \omega, T)$	Frequency-dependent configurational diffusion coefficient	(4.5), (6.10)
$\zeta(\underset{\sim}{Q})$	Friction kernel for configurational diffusion	(4.7*b*)
$\zeta(\underset{\sim}{Q}, \omega)$	Frequency-dependent friction kernel	(6.9)
$\underset{\sim}{Q}^{\ddagger}$	Fraction of native contacts at the barrier peak	(5.17)
$\beta^{\ddagger}$	Effective experimental transition state position	(5.18)
$\omega^{\ddagger}$	Frequency of barrier peak	(6.16)
$\lambda^{\ddagger}$	Grote–Hynes reactive frequency	(6.16)
ϵ_i	Energy of native contact i	(7.12)
l_i	Sequence length of native contact i ($=\lvert\alpha-\beta\rvert$ when native contact i is made between residues α and β)	(7.12), (7.13)
$\bar{l}$	Mean sequence length between all native contacts	(7.12), (7.22)
$\underset{\sim}{Q}_i(\underset{\sim}{Q})$	Probability of forming native contact i at $\underset{\sim}{Q}$	(7.12), (7.17)

† Equation where the symbol is first defined, or representative equation. Symbols may occasionally have other meanings which should be clear from the context.

Appendix B. GREM construction for the glass transition

In the GREM, one considers the ν^N states of a polymer as the end points of an ultrametric tree of n levels, where n is taken to be large (see Fig. 7). To each level i of the tree one associates three quantities α_i, a_i, and q_i. Two configurations a and b have an overlap $q_{ab} = q_i$, where q_i is the level on the tree where the branches coming from a and b join. q_i is an increasing function of i with $0 = q_1 < q_2, \ldots, < q_{n+1} = 1$. At the ith level one branch divides into a α_i^N branches, so at level i there are $(\alpha_1, \alpha_2, \ldots, \alpha_i)^N$ branches, and $(\alpha_1, \alpha_2, \ldots, \alpha_n)^N = \nu^N$.

On each branch of the tree at level i, one chooses a random variable $\epsilon_i^{(b)}$ according to a distribution $\rho_i(\epsilon_i^{(b)})$ whose width is a_i:

$$\rho_i(\epsilon_i^{(b)}) = \frac{1}{(2\pi a_i N b^2)^{\frac{1}{2}}} \exp\left(-\frac{(\epsilon_i^{(b)})^2}{a_i N b^2} \right). \tag{B 1}$$

The energy of each configuration b is then given by

$$E_b = \sum_{i=1}^{n} \epsilon_1^{(b)}, \tag{B 2}$$

where the $\epsilon_i^{(b)}$ are the energies associated with the n branches that connect each state to the top of the tree. States a and b with overlap $q_{ab} = q_i$ have $\epsilon_j^{(a)} = \epsilon_j^{(b)}$ for $j \leqslant i-1$ and $\epsilon_j^{(a)} \neq \epsilon_j^{(b)}$ for $j \geqslant i$. The model is defined once the two sequences α_i and a_i are given for $1 \leqslant i \leqslant n$. If we choose the normalization

$$\sum_{i=1}^{n} a_i = 1, \tag{B 3}$$

then the energies E_b of the N states are distributed as Gaussian random variables:

$$P_a(E_a) = \frac{1}{(2\pi N b^2)^{\frac{1}{2}}} \exp\left(-\frac{(E_a)^2}{2N b^2} \right). \tag{B 4}$$

The probability distribution $P_{ab}(E_a, E_b)$ that two configurational states a and b have energies E_a and E_b is

$$P_{a,b}(E_a, E_b) = \text{const.} \times \exp\left[-\frac{1}{4Nb^2} \left(\frac{(E_a + E_b)^2}{1 + v_{ab}} + \frac{(E_a - E_b)^2}{1 - v_{ab}} \right) \right] \tag{B 5}$$

where v_{ab} is a measure of the correlation in energy between two configurations with overlap q_i:

$$v_{ab} = v_i = \sum_{j=1}^{i-1} a_j. \tag{B 6}$$

Given a configuration (a), the number of configurations that have an overlap of q_i with (a) is

$$\boldsymbol{\Omega}_i = \mathrm{e}^{N s_i} = (\alpha_i^N - 1)(\alpha_{i+1}, \ldots, \alpha_n)^N. \tag{B 7}$$

This is the number of states to which Eqs. (B 5) and (B 6) apply. In the thermodynamic limit $(N \to \infty)$, the entropy at level i is

$$s_i = \sum_{j=i}^{n} \ln \alpha_j. \tag{B 8}$$

We assume this equation holds approximately for fairly large N. For N fairly large there is almost a continuous range of possible overlaps ($0 \leqslant q \leqslant 1$) which means the number of levels in the ultrametric tree is large. So s_i and v_i may be treated as continuous quantities $s(q)$ and $v(q)$, which means

$$\ln \alpha(q) = -\frac{\mathrm{d}s(q)}{\mathrm{d}q} \tag{B 9}$$

and

$$a(q) = \frac{\mathrm{d}v(q)}{\mathrm{d}q}. \tag{B 10}$$

There are two cases where the GREM has been solved (A third scenario is if $T(q)$ is monotonically increasing or constant – in this case we just retrieve the REM results).

Continuous-type GREM

If the freezing (glass) temperarture as a function of q, defined by

$$\frac{T_{\mathrm{G}}(q)}{b\sqrt{2}} = \left(\frac{a(q)}{\log \alpha(q)} \right)^{\frac{1}{2}} = \left(\frac{\mathrm{d}v(q)/\mathrm{d}q}{-\mathrm{d}s(q)/\mathrm{d}q} \right)^{\frac{1}{2}} \tag{B 11}$$

is a monotonically decreasing function of the overlap q, then the freezing occurs from the top of the ultrametric tree downward (most dissimilar states freeze out first), and the thermodynamic free energy is given by

$$-\frac{F}{N} = Ts_0 + \frac{b^2}{2T} \qquad T > T(0)$$

$$-\frac{F}{N} = Ts(q(T)) + \frac{b^2}{2T}\left[v(1) - v(q(T))\right]$$

$$+ b\sqrt{2}\int_0^{q(T)} \mathrm{d}q \left(-\frac{\mathrm{d}s(q)}{\mathrm{d}q}\frac{\mathrm{d}v(q)}{\mathrm{d}q} \right)^{\frac{1}{2}} \quad T(1) < T = T(q)$$

$$-\frac{F}{N} = b\sqrt{2}\int_0^1 \mathrm{d}q \left(-\frac{\mathrm{d}s(q)}{\mathrm{d}q}\frac{\mathrm{d}v(q)}{\mathrm{d}q} \right)^{\frac{1}{2}} \qquad T < T(1) \tag{B 12}$$

where $q(T)$ is the inverse of $T_{\mathrm{G}}(q)$, $s_0 = \ln \nu$, and $s(q) = S(q)/N$ is the specific entropy (per monomer). At the highest temperatures (i.e. those higher than $T_{\mathrm{G}}(q = 0)$ if $T_{\mathrm{G}}(q = 0) < \infty$) the system can freely explore all of its states regardless of dissimilarity. At lower temperatures there is a continuous freezing which gradually causes states to be more localized. When $T_{\mathrm{G}}(1) < T < T_{\mathrm{G}}(0)$ the system is frozen into basins of size $q(T)$ given by the inverse of $T_{\mathrm{G}}(q)$ in Eq. (B 11).

Discrete-type GREM

The function $T_G(q)$ has a single maximum, say at q^*. There will be a REM transition with a discreet jump in the order parameter q, and then a gradual freezing as in the continuous-type GREM above. Define q_g^0 such that

$$\frac{v(q_g^0)-v(0)}{s(0)-s(q_g^0)} = \frac{(\mathrm{d}v/\mathrm{d}q)(q_g^0)}{-(\mathrm{d}s/\mathrm{d}q)(q_g^0)}. \tag{B 13}$$

q_g^0 is always greater than q^*. For a Hamiltonian with pair interactions as analyzed in Sections 3 and 3.1, $v(q) = q$ and Eq. (B 13) becomes

$$-\frac{\mathrm{d}s}{\mathrm{d}q}(q_g^0) = \frac{s_{\max}-s(q_g^0)}{q_g^0-q_{\min}} \tag{B 14}$$

so that q_g^0 can be interpreted as the point where a line of smallest negative slope drawn from the peak of the entropy curve lies tangent to the entropy curve at $q > q_{\min}$.

Now define what will be a REM-like transition temperature, where the freezing will have a sudden onset at q_g^0:

$$\frac{T_g^0}{b\sqrt{2}} = \left(\frac{(\mathrm{d}v/\mathrm{d}q)(q_g^0)}{-(\mathrm{d}s/\mathrm{d}q)(q_g^0)} \right)^{\frac{1}{2}} = \left(\frac{v(q_g^0)-v(0)}{s(0)-s(q_g^0)} \right)^{\frac{1}{2}}. \tag{B 15}$$

For a Hamiltonian with pair interactions as analyzed in Sections 3 and 3.1, $v(q) = q$ and Eq. B.15 becomes

$$T_G^0/b\sqrt{2} = \left(-\frac{\mathrm{d}s}{\mathrm{d}q}(q_g^0) \right)^{-\frac{1}{2}}. \tag{B 16}$$

The thermodynamic free energy is given by

$$-\frac{F}{N} = Ts_0 + \frac{b^2}{2T} \qquad T > T_G^0$$

$$-\frac{F}{N} = Ts(q(T)) + \frac{b^2}{2T}[v(1)-v(q(T))]$$

$$+ b\sqrt{2}\int_{q_g^0}^{q(T)} \mathrm{d}q \left(-\frac{\mathrm{d}s(q)}{\mathrm{d}q}\frac{\mathrm{d}v(q)}{\mathrm{d}q} \right)^{\frac{1}{2}}$$

$$+ b\sqrt{2}\,[(v(q_g^0)-v(0))(s(0)-s(q_g^0))]^{\frac{1}{2}} \quad T(1) < T < T_G^0$$

$$-\frac{F}{N} = b\sqrt{2}\int_{q_g^0}^{1} \mathrm{d}q \left(-\frac{\mathrm{d}s(q)}{\mathrm{d}q}\frac{\mathrm{d}v(q)}{\mathrm{d}q} \right)^{\frac{1}{2}}$$

$$+ b\sqrt{2}\,[(v(q_g^0)-v(0))(s(0)-s(q_g^0))]^{\frac{1}{2}} \quad T < T(1). \tag{B 17}$$

Appendix C. Effect of a Q-dependent diffusion coefficient

To estimate the effect of $D(Q)$ on folding, note that the static diffusion coefficient may be obtained from Eq. (6.10) by letting $s \to 0$. Then

$$D(Q) = \frac{1}{\langle \tau(Q, \tilde{T}) \rangle} \tag{C 1}$$

and we use either Eqs. (4.26) or (4.28) for the mean escape time, which is a function of $\tilde{T} \equiv T/T_G$. Several folding models give $T_F/T_G(Q)$ as an increasing function of Q, see for example, Fig. 15. We can numerically approximate the function in Fig. 15 along the 'most probable path' of the free-energy surface in Fig. 16, which has a moderate decrease in $T_F/T_G(Q)$, by letting

$$T_F/T_G(Q) \approx 2 - (\tfrac{2}{3})Q \tag{C 2}$$

and substitute this into Eqs. (4.26) or (4.28) to obtain $D(Q, T_F)$. For simplicity we approximate the thermodynamic potential at T_F by a parabolic function with barrier height $\sim 10\, k_B T_F$ and barrier peak position $Q^{\ddagger} = \frac{1}{2}$:

$$F(Q)/T_F \approx 10 - 40(Q - \tfrac{1}{2})^2. \tag{C 3}$$

Taking for illustration the high temperature regime of Eq. (4.28), $G(Q)$ in Eq. (4.7*a*) is

$$G(Q)/T_F = F(Q)/T_F - R = F(Q) - S_0 \left(\frac{1}{(T_F/T_G(Q))^2} - \frac{1}{(T_F/T_G(0))^2} \right). \tag{C 4}$$

Taking S_0 to be about 50 k_B, we find that $G(Q)$ has a maximum at $Q^* \simeq 0{\cdot}7 - 0{\cdot}75$ rather than $Q^{\ddagger} = 0{\cdot}5$. This is a significant shift in the transition state position towards more native states. However the ratio of the rates, accounting for Q-dependent friction and ignoring it, is

$$\frac{\tau(Q^*)}{\tau(Q^{\ddagger})} = e^{\beta[G(Q^*) - G(Q^{\ddagger})]} \simeq 5, \tag{C 5}$$

which is a relatively small effect: the change in barrier height is only $(1-2)k_B T$. This is due to the fact that the change in effective barrier height is a second order effect since we are looking at perturbations about a maximum.

Appendix D. A frequency-dependent Einstein relation

A system governed by a generalized Fokker–Planck equation in Eq. (4.5) shows the same linear response as one governed by an overdamped GLE [Eq. (6.2)]. To see this, we show that the response of the GLE and GFE to a weak external harmonic field gives mobilities such that the friction and diffusion coefficient are related by

$$\hat{\zeta}(Q, \omega, T) = \frac{k_B T}{\hat{D}(Q, \omega, T)}. \tag{D 1}$$

The mobility $\mu(\omega)$ of an overdamped GLE, defined through the response to an external harmonic driving force by

$$\langle \dot{Q}(t) \rangle \equiv \mathscr{RE}(\mu(\omega) F_{\text{ext}}(t)), \tag{D 2}$$

is given by

$$\mu(\omega) = \frac{1}{\hat{\zeta}(\omega)} \tag{D 3}$$

in response to a harmonic driving force (Kubo, 1966). Now we find the response of a system obeying Eq. (4.5) to this same external driving field $\mathscr{RE}(F_0 e^{i\omega t})$. Taking the time transform of Eq. (4.5) gives

$$\frac{\partial \rho(Q, t)}{\partial t} = \frac{\partial}{\partial Q} \int_0^t dt' \, D(t-t') \left[\frac{\partial \rho(Q, t')}{\partial Q} - \frac{F_0}{k_B T} e^{i\omega t'} \rho(Q, t') \right]. \tag{D 4}$$

To this we seek the linear response in the form $\rho(Q, t) = \rho_{\text{eq}}(Q) + \delta\rho(Q, t)$ where $\rho_{\text{eq}}(Q) = \rho_0 \exp(-\omega_0^2 Q^2 / 2k_B T)$ is the equilibrium probability density for a harmonic well potential, and in the end we can let $\omega_0^2 \to 0$ (though it is not necessary for the result). Neglecting higher order corrections due to a position-dependent diffusion constant, and using linear response so only the equilibrium density couples to the weak external field, Eq. (D 4) becomes

$$\frac{\partial \delta\rho(Q, t)}{\partial t} - \int_0^t dt' \, D(t-t') \frac{\partial^2 \delta\rho(Q, t')}{\partial Q^2} = \rho_{\text{eq}}(Q)'' D_o - \rho_{\text{eq}}(Q)' \hat{D}(\omega) \frac{F_0}{k_B T} e^{i\omega t}, \tag{D 5}$$

where $\rho_{\text{eq}}(Q)' = d\rho_{\text{eq}}(Q)/dQ$. To find the response $\langle Q \rangle$ to the field we can multiply Eq. (D 5) by Q and integrate: $\int dQ \, Q \delta\rho(Q, t) \equiv \langle Q \rangle(t)$ to give

$$\frac{\partial}{\partial t} \langle Q \rangle(t) - \int_0^t dt' \, D(t-t') \int_{-\infty}^{\infty} dQ \, Q \frac{\partial^2}{\partial Q^2} \delta\rho(Q, t') = 0 - \hat{D}(\omega) \frac{F_0}{k_B T} e^{i\omega t} \int_{-\infty}^{\infty} dQ \, Q \rho_{\text{eq}}(Q)'.$$

The second term on the left-hand side vanishes by symmetry. Performing the integral on the right-hand side yields:

$$\langle \dot{Q} \rangle (t) = \hat{D}(\omega) \frac{F_0}{k_B T} e^{i\omega t}. \tag{D 6}$$

By Eq. (D 2) the mobility is thus

$$\mu(\omega) = \frac{\hat{D}(\omega)}{k_B T}, \tag{D 7}$$

which, equating with (D 3), generalizes the Einstein relation for response at frequency ω [Eq. (D 1)], and justifies using the reciprocal of Eq. (6.10) in the calculation of the friction $\hat{\zeta}(\omega)$, appearing in the overdamped GLE.

The friction kernel $\hat{\zeta}(\omega)$ is expressed through Eqs. (6.10) and (D 1) by averaging over the distribution of escape times $P_Q(\tau, T)$. We can rewrite Eq. (6.10) as

$$\hat{D}(Q, \omega, T) = \lambda(Q) \frac{\mathscr{L}_t \langle e^{-t/\tau} \rangle}{\mathscr{L}_t(-d/dt) \langle e^{-t/\tau} \rangle}, \tag{D 8}$$

where $\mathscr{L}_t$ is the Laplace transform. Then to evaluate $\hat{D}(Q, \omega, T)$, note that $\langle e^{-t/\tau} \rangle$ is of the form

$$\langle e^{-t/\tau} \rangle \sim \int_{\ln \tau_L}^{\ln \tau_U} d(\ln \tau)\, e^{-S(\ln \tau)^2} \exp\left[-C_1 \frac{t}{\tau_0} e^{-C_2 S(\ln \tau)} \right], \tag{D 9}$$

which is reminiscent of the after-effect function $f(C_1 t/\tau_0, C_2/\sqrt{S})$, which has been used to describe non-exponential decay in glasses (DiMarzio & Sanchez, 1986). For mesoscopic systems relevant to folding ($N \lesssim 100$), a good approximation to evaluate the after-effect function is to linearize the Gaussian term on the range $(\ln \tau_L, \ln \tau_U)$. Carrying out this calculation, a closed form for the friction can be obtained as an accurate approximation for small proteins

$$\hat{D}(Q, \omega, T) = \lambda(Q) \frac{\frac{w_{\mathrm{BL}}}{1+\omega} + \frac{F}{1-c}\left[f^{c-1}\, {}_2F_1(1, 1-c, 2-c, -\omega/f) - {}_2F_1(1, 1-c, 2-c, -\omega)\right]}{\frac{w_{\mathrm{BL}}}{1+\omega} + \frac{F}{c}\left[{}_2F_1(1, -c, 1-c, -\omega) - f^c\, {}_2F_1(1, -c, 1-c, -\omega/f)\right]}, \tag{D 10}$$

where ${}_2F_1$ is the hypergeometric function, ω is in units of $1/\tau_0$ where τ_0 is the timescale for the fastest Rouse–Zimm modes, F, f and c are temperature dependent coefficients, and $\omega_{\mathrm{BL}}(T)$ is the weight of the fast modes in the distribution $P_{\mathrm{Q}}(\tau, T)$. The function $\hat{D}(Q, \omega, T)$ is plotted in Fig. 23.

11. References

Abkevich, V. I., Gutin, A. M. & Shakhnovich, E. I. (1994). Specific nucleus as the transition state for protein folding: evidence from the lattice model. *Biochemistry* **33**, 10026–10036.

Alm, E. & Baker, D. (1999). Prediction of protein-folding mechanisms from free-energy landscapes derived from native structures. *Proc. natn. Acad. Sci. USA* **96**, 11305–11310.

Austin, R. H., Beeson, K. W., Eisenstein, L. & Frauenfelder, H. (1975). Dynamics of ligand binding to myoglobin. *Biochemistry* **14**, 5355–5373.

Bai, Y., Sosnick, T. R., Mayne, L. & Englander, S. W. (1995). Protein folding intermediates: native-state hydrogen exchange. *Science* **269**, 192–197.

Bastolla, U. & Grassberger, P. (2001). Exactness of the annealed and the replica symmetric approximations for random heteropolymers. *Phys. Rev* (*E*) **63**, art. no. 031901.

Becker, R. & Doring, W. (1935). Kinetic treatment of nucleus formation in oversaturated steam [German]. *Ann. Phys.* (*Leipzig*) **24**, 719–752.

Berezhkovskii, A. M., Pollak, E. & Zitserman, V. Y. (1992). Activated rate processes: generalization of the Kramers–Grote–Hynes and Langer theories. *J. chem. Phys.* **97**, 2422–2437.

Berriz, G. F., Gutin, A. M. & Shakhnovich, E. I. (1997). Cooperativity and stability in a langevin model of proteinlike folding. *J. chem. Phys.* **106**, 9276–9285.

Boczko, E. M. & Brooks, C. L. (1995). First principles calculation of the folding free energy for a three helix bundle protein. *Science* **269**, 393–396.

Bohr, H. G. & Wolynes, P. G. (1992). Initial events of protein folding from an information-processing viewpoint. *Phys. Rev.* (*A*) **46**, 5242–5248.

Brown, B. M. & Sauer, R. T. (1999). Tolerance of arc repressor to multiple-alanine substitutions. *Proc. natn. Acad. Sci. USA* **96**, 1983–1988.

Bryngelson, J. D., Onuchic, J. N., Socci, N. D. & Wolynes, P. G. (1995). Funnels, pathways and the energy landscape of protein folding. *Proteins* **21**, 167–195.

Bryngelson, J. D. & Wolynes, P. G. (1987). Spin glasses and the statistical mechanics of protein folding. *Proc. natn. Acad. Sci. USA* **84**, 7524–7528.

Bryngelson, J. D. & Wolynes, P. G. (1989). Intermediates and barrier crossing in a random energy model (with applications to protein folding). *J. phys. Chem.* **93**, 6902–6915.

Bryngelson, J. D. & Wolynes, P. G. (1990). A simple statistical field theory of heteropolymer collapse with applications to protein folding. *Biopolymers* **30**, 177–188.

Buchler, N. E. G. & Goldstein, R. A. (1999). Universal correlation between energy gap and foldability for the random energy model and lattice proteins. *J. chem. Phys.* **111**, 6599–6609.

Bursulaya, B. D. & Brooks, C. L. (1999). Folding free energy surface of a three-stranded β-sheet protein. *J. Am. Chem. Soc.* **121**, 9947–9951.

Bursulaya, B. D. & Brooks, C. L. (2000). Comparative study of the folding free energy landscape of a three-stranded β-sheet protein with explicit and implicit solvent models. *J. phys. Chem.* **104**, 12378–12383.

Burton, R. E., Myers, J. K. & Oas, T. G. (1998). Protein folding dynamics: quantitative comparison between theory and experiment. *Biochemistry* **37**, 5337–5343.

Cahn, J. W. & Hilliard, J. E. (1958). Free energy of a non-uniform system. i. interfacial free energy. *J. chem. Phys.* **28**, 258–267.

Caldeira, A. O. & Leggett, A. J. (1983). Quantum tunneling in a dissipative system. *Ann. Phys.* **149**, 374–456. [Erratum, **153**, 445 (1983).]

Chandler, D. (1978). Statistical mechanics of isomerization dynamics in liquids and the transition state approximation. *J. chem. Phys.* **68**, 2959–2970.

Clementi, C., Jennings, P. A. & Onuchic, J. N. (2000a). How native state topology affects the folding of dihydrofolate reductase and interleukin-1beta. *Proc. natn. Acad. Sci. USA* **97**, 5871–5876.

Clementi, C., Nymeyer, H. & Onuchic, J. N. (2000b). Topological and energetic factors: what determines the structural details of the transition state ensemble and en-route intermediates for protein folding? an investigation for small globular proteins. *J. molec. Biol.* **298**, 937–953.

Crane, J. C., Koepf, E. K., Kelly, J. W. & Gruebele, M. (2000). Mapping the transition state of the ww domain β-sheet. *J. molec. Biol.* **298**, 283–292.

Dalessio, P. M. & Ropson, I. J. (2000). β-sheet proteins with nearly identical structures have different folding intermediates. *Biochemistry* **39**, 860–871.

de Almeida, J. R. L. & Thouless, D. J. (1978). Stability of the sherrington-kirkpatrick solution of a spin glass model. *J. Phys.* (*A*) **11**, 983–990.

De Santis, E., Parisi, G. & Ritort, F. (1995). On the static and dynamical transition in the mean-field potts glass. *J. Phys.* (*A*) **28**, 3025–3041.

Derrida, B. (1981). Random-energy model: an exactly solvable model of disordered systems. *Phys. Rev.* (*B*) **24**, 2613–2626.

Derrida, B. (1985). A generalization of the random energy model which includes correlations between energies. *J. Physique – Lett.* **46**, L401–L407.

Derrida, B. & Gardner, E. (1986a). Magnetic properties and the function $q(x)$ of the generalised random energy model. *J. Phys.* (*C*) *Solid State Phys.* **19**, 5783–5798.

Derrida, B. & Gardner, E. (1986b). Solution of the generalised random energy model. *J. Phys.* (*C*) *Solid State Phys.* **19**, 2253–2274.

Deutsch, J. M. (1980). A simple method for determining the mean passage time for diffusion controlled processes. *J. chem. Phys.* **73**, 4700–4701.

DiMarzio, E. & Sanchez, I. (1986). On the origin of non-exponential decay processes in amorphous systems with application to polymers. In *Transport and Relaxation in Random Materials* (eds. J. Klafter, R. Rubin & M. Shlesinger). Singapore: World Scientific.

Dinner, A. R., Abkevich, V., Shakhnovich, E. & Karplus, M. (1999). Factors that affect the folding ability of proteins. *Proteins* **35**, 34–40.

Dinner, A. R. & Karplus, M. (2001). The roles of stability and contact order in determining protein folding rates. *Nature struct. Biol.* **8**, 21–22.

Dobson, C. M., Sali, A. & Karplus, M. (1998). Protein folding: A perspective from theory and experiment. *Angew. Chem. Int. Ed. Engl.* **37**, 868–893.

Doi, M. & Edwards, S. F. (1986). *The Theory of Polymer Dynamics*. Oxford: Oxford University Press.

Douglas, J. F. & Ishinabe, T. (1995). Self-avoiding-walk contacts and random-walk self-intersections in variable dimensionality. *Phys. Rev.* (*E*) **51**, 1791–1817.

Du, R., Pande, V. S., Grosberg, A. Y., Tanaka, T. & Shakhnovich, E. S. (1998). On the transition coordinate for protein folding. *J. chem. Phys.* **108**, 334–350.

Du, R., Pande, V. S., Grosberg, A. Y., Tanaka, T. & Shakhnovich, E. S. (1999). On the role of conformational geometry in protein folding. *J. chem. Phys.* **111**, 10375–10380.

Eastman, P. & Doniach, S. (1998). Multiple time step diffusive langevin dynamics for proteins. *Proteins* **30**, 215–227.

Eastwood, M. P. & Wolynes, P. G. (2001). Role of explicitly cooperative interactions in protein folding funnels: a simulation study. *Proteins* **30**, 215–227.

Elmer, S. & Pande, V. S. (2001). A new twist on the helix–coil transition: a non-biological helix with protein-like intermediates and traps. *J. phys. Chem.* **105**, 482–485.

Evans, R. (1992). Density functionals in the theory of inhomogeneous fluids. In *Fundamentals of Inhomogeneous Fluids* (ed. D. Henderson). New York: Dekker.

Ferguson, N., Capaldi, A. P., James, R., Kleanthous, C. & Radford, S. E. (1999). Rapid folding with and without populated intermediates in the homologous four-helix proteins im7 and im9. *J. molec. Biol.* **286**, 1597–1608.

Fernández, A., Kostov, K. S. & Berry, R. S. (2000). Coarsely resolved topography along protein folding pathways. *J. chem. Phys.* **112**, 5223–5229.

Fersht, A. R. (2000). Transition-state structure as a unifying basis in protein-folding mechanisms: contact order, chain topology, statbility, and the extended nucleus mechanism. *Proc. natn. Acad. Sci. USA* **97**, 1525–1529.

Fisher, M. E. (1967). The theory of condensation and the critical point. *Physics* **3**, 255–283.

Flory, P. J. (1953). *Principles of Polymer Chemistry*. Cornell University, Ithaca.

Flory, P. J. (1956). Theory of elastic mechanisms in fibrous proteins. *J. Am. Chem. Soc.* **78**, 5222–5235.

Flory, P. J. & Matheson, R. R. (1984). Statistical thermodynamics of semirigid macromolecules: chains with interconvertible rodlike and random-coil sequences in equilibrium. *J. phys. Chem.* **88**, 6606–6612.

Galzitskaya, O. V. & Finkelstein, A. V. (1999). A theoretical search for folding/unfolding nuclei in three dimensional protein structures. *Proc. natn. Acad. Sci. USA* **96**, 11299–11304.

Galzitskaya, O. V., Ivankov, D. N. & Finkelstein, A. V. (2001). Folding nuclei in proteins. *FEBS Lett.* **489**, 113–118.

Garcia, A. E. & Hummer, G. (2000). Water penetration and escape in proteins. *Proteins* **38**, 261–272.

Gardner, E. (1985). Spin glasses with p-spin interactions. *Nucl. Phys.* (*B*) **257**, 747–765.

Grantcharova, V. P., Santiago, J. V., Baker, D. & Riddle, D. S. (1998). Important role of hydrogen bonds in the structurally polarized transition state for folding of the src sh3 domain. *Nature struct. Biol.* **5**, 714–720.

Gross, D. J., Kanter, I. & Sompolinksy, H. (1985). Mean-field theory of the potts glass. *Phys. Rev. Lett.* **55**, 304–307.

Gross, D. J. & Mézard, M. (1984). The simplest spin glass. *Nucl. Phys.* (*B*) **240**, 431–452.

Grote, R. F. & Hynes, J. T. (1980). The stable states picture of chemical reactions. II. Rate constants for condensed and gas phase reaction models. *J. chem. Phys.* **73**, 2715–2732.

Guerois, R. & Serrano, L. (2000). The sh3-fold family: experimental evidence and prediction of variations in the folding pathways. *J. molec. Biol.* **304**, 967–982.

Gunton, J. D., Miguel, M. S. & Sahni, P. S. (1983). The dynamics of first order transitions. In *Phase Transitions and Critical Phenomena* (eds. C. Domb & J. L. Lebowitz), vol. 8, pp. 267–466. New York: Academic Press.

Guo, Z. & Brooks, C. L. (1997). Thermodynamics of protein folding: a statistical mechanical study of a small all-β protein. *Biopolymers* **42**, 745–757.

Guo, Z. & Thirumalai, D. (1995). Kinetics of protein folding: nucleation mechanism, time scales, and pathways. *Biopolymers* **36**, 83–102.

Guo, Z. & Thirumalai, D. (1996). Kinetics and thermodynamics of folding of a *de novo* designed four-helix bundle protein. *J. molec. biol.* **263**, 323–343.

Guo, Z., Thirumalai, D. & Honeycutt, J. D. (1992). Folding kinetics of proteins: a model study. *J. chem. Phys.* **97**, 525–535.

Gutin, A. M., Abkevich, V. I. & Shakhnovich, E. I. (1995). Evolution-like selection of fast-folding model proteins. *Proc. natn. Acad. Sci. USA* **92**, 1282–1286.

Hagen, S. J., Hofrichter, J. A., Szabo, A. & Eaton, W. A. (1996). Diffusion-limited contact formation in unfolded cytochrome c: estimating the maximum rate of protein folding. *Proc. natn. Acad. Sci. USA* **93**, 11615–11617.

Hanggi, P., Talkner, P. & Borkevec, M. (1990). Reaction-rate theory: fifty years after Kramers. *Rev. Mod. Phys.* **62**, 251–341.

Hao, M.-H. & Scheraga, H. (1997). On foldable protein-like models: a statistical-mechanical study with monte carlo simulations. *Physica* (*A*) **244**, 124–146.

Hoang, T. X. & Cieplak, M. (2000). Sequencing of folding events in Gō-type proteins. *J. chem. Phys.* **113**, 8319–8328

Hoeve, C. A. J., DiMarzio, E. A. & Peyser, P. (1965). Adsorption of polymer molecules at low surface coverage. *J. chem. Phys.* **42**, 2558–2563.

Horovitz, A. & Fersht, A. (1992). Co-operative interactions during protein folding. *J. molec. Biol.* **224**, 733–740.

Huang, D. M. & Chandler, D. (2000). Temperature and length scale dependence of hydrophobic effects and their possible implications for protein folding. *Proc. natn. Acad. Sci. USA* **97**, 8324–8327.

Huang, G. S. & Oas, T. G. (1995). Submillisecond folding of monomeric lambda-repressor. *Proc. natn. Acad. Sci. USA* **92**, 6878–6882.

Hummer, G., Garde, S., García, A. E. & Pratt, L. R. (2000). New perspectives on hydrophobic effects. *Chem. Phys.* **258**, 349–370.

Itzhaki, L. S., Otzen, D. E. & Fersht, A. R. (1995). The structure of the transition state for folding of chymotrypsin inhibitor 2 analyzed by protein engineering methods: evidence for a nucleation-condensation mechanism for protein folding. *J. molec. Biol.* **254**, 260–288.

Kenkre, V. M., Montroll, E. W. & Shlesinger, M. F. (1973). Generalized master equations for continuous-time random walks. *J. stat. Phys.* **9**, 45–50.

Kim, D. E., Fisher, C. & Baker, D. (2000). A breakdown of symmetry in the folding transition state of protein 1. *J. molec. Biol.* **298**, 971–984.

Kim, D. E., Gu, H. & Baker, D. (1998). The sequences of small proteins are not extensively optimized for natural selection. *Proc. natn. Acad. Sci. USA* **95**, 4982–4986.

Kirkpatrick, T. R., Thirumalai, D. & Wolynes, P. G. (1989). Scaling concepts for the dynamics of viscous liquids near an ideal glassy state. *Phys. Rev.* (*A*) **40**, 1045–1054.

Kirkpatrick, T. R. & Wolynes, P. G. (1987). Stable and metastable states in mean-field potts and structural glasses. *Phys. Rev.* (*B*) **36**, 8552–8564.

Klimov, D. & Thirumalai, D. (1996). Criterion that determines the foldability of proteins. *Phys. Rev. Lett.* **76**, 4070–4073.

Klimov, D. & Thirumalai, D. (1997). Viscosity dependence of the folding rates of proteins. *Phys. Rev. Lett.* **79**, 317–320.

Klimov, D. K. & Thirumalai, D. (1998a). Cooperativity in protein folding: from lattice models with sidechains to real proteins. *Folding and Design* **3**, 127–139.

Klimov, D. K. & Thirumalai, D. (1998b). Lattice models for proteins reveal multiple folding nuclei for nucleation-collapse mechanism. *J. molec. Biol.* **282**, 471–492.

Kolinski, A., Galazka, W. & Skolnick, J. (1996). On the origin of the cooperativity on protein folding – implications from model simulations. *Proteins: Struct. Funct. Genet.* **26**, 271–287.

Kramers, H. A. (1940). Brownian motion in a field of force and the diffusion model of chemical reactions. *Physica* (*Utrecht*) **7**, 284–304.

Kubo, R. (1966). The fluctuation-dissipation theorem. *Rep. Progr. Phys.* **29**, 255–283.

Landau, L. D. & Lifshitz, E. M. (1980). *Statistical Physics*, 3rd edn. Oxford: Pergamon Press.

Langer, J. S. (1967). Theory of the condensation point. *Ann. Phys.* (*N.Y.*) **41**, 108–157.

Langer, J. S. (1969). Statistical theory of the decay of metastable states. *Ann. Phys.* (*N.Y.*) **54**, 258–275.

Lazaridis, T. & Karplus, M. (1997). New view of protein folding reconciled with the old through multiple unfolding simulations. *Science* **278**, 1928–1931.

Lifshitz, I. M., Grosberg, A. Y. & Khokhlov, A. R. (1978). Some problems of the statistical physics of polymer chains with volume interaction. *Rev. Mod. Phys.* **50**, 683–713.

Lindberg, M. & Oliveberg, M. (2002). Is the folding energy landscape evolved to optimize structural cooperativity? Preprint.

Lothe, J. & Pound, G. M. (1962). Reconsiderations of nucleation theory. *J. chem. Phys.* **36**, 2080.

Lothe, J. & Pound, G. M. (1969). Statistical mechanics of nucleation. In *Nucleation* (ed. A. C. Zettlemoyer), pp. 109–149. New York: Dekker.

Lum, K., Chandler, D. & Weeks, J. D. (1999). Hydrophobicity at small and large length scales. *J. phys. Chem.* **103**, 4570–4577.

Maritan, A., Micheletti, C., Trovato, A. & Banavar, J. R. (2000). Optimal shapes of compact strings. *Nature* **406**, 287–290.

Martinez, J. C., Pisabarro, M. T. & Serrano, L. (1998). Obligatory steps in protein folding and the conformational diversity of the transition state. *Nature Struct. Biol.* **5**, 721–729.

Mélin, R., Li, H., Wingreen, N. S. & Tang, C. (1999). Designability, thermodynamic stability, and dynamics in protein folding: a lattice model study. *J. chem. Phys.* **110**, 1252–1262.

Metzler, R. & Klafter, J. (2000). Subdiffusive transport close to thermal equilibrium: from the langevin equation to fractional diffusion. *Phys. Rev.* (*E*) **61**, 6308–6311.

Mézard, M., Parisi, E. & Virasaro, M. A. (1986). *Spin Glass Theory and Beyond*. Singapore: World Scientific Press.

Mézard, M., Parisi, G., Sourlas, N., Toulouse, G. & Virasoro, M. (1984). Replica symmetry breaking and the nature of the spin glass phase. *J. Physique* **45**, 843–854.

Miller, W. H. (1974). Quantum mechanical transition state theory and a new semiclassical model for reaction rate constants. *J. chem. Phys.* **61**, 1823–1834.

Miyazawa, S. & Jernigan, R. L. (1985). Estimation of effective interresidue contact energies from protein crystal structures: quasi-chemical approximation. *Macromolecules* **218**, 534–552.

Miyazawa, S. & Jernigan, R. L. (1996). Residue-residue potentials with a favorable contact pair term and an unfavorable high packing density term, for simulation and threading. *J. molec. Biol.* **256**, 623–644.

Munoz, V. & Eaton, W. A. (1999). A simple model for calculating the kinetics of protein folding from three-dimensional structures. *Proc. natn. Acad. USA* **96**, 11311–11316.

Munoz, V. & Serrano, L. (1996). Local versus nonlocal interactions in protein folding and stability – an experimentalist's point of view. *Folding and Design* **1**, R71–R77.

Nymeyer, H., Socci, N. D. & Onuchic, J. N. (2001). Folding rates in model proteins. Preprint.

Oliveberg, M., Tan, Y., Silow, M. & Fersht, A. (1998). The changing nature of the protein folding transition state: implications for the shape of the free energy profile for folding. *J. molec. Biol.* **277**, 933–943.

Onuchic, J. N., Socci, N. D., Luthey-Schulten, Z. & Wolynes, P. G. (1996). Protein folding funnels: the nature of the transition state ensemble. *Folding and Design* **1**, 441–450.

Onuchic, J. N., Wolynes, P. G., Luthey-Schulten, Z. & Socci, N. D. (1995). Toward an outline of the topography of a realistic protein-folding funnel. *Proc. natn. Acad. Sci. USA* **92**, 3626–3630.

Otzen, D. E., Kristensen, O., Proctor, M. & Oliveberg, M. (1999). Structural changes in the transition state of protein folding: alternative interpretations of curved chevron plots. *Biochemistry* **38**, 6499–6511.

Pande, V. S., Grosberg, A. Y. & Tanaka, T. (1997). On the theory of folding kinetics for short proteins. *Folding and Design* **2**, 109–114.

Pande, V. S. & Plaxco, K. W. (2001). Testing the applicability of energy landscape theory. Preprint.

Panick, G., Vidugiris, G. J. A., Malessa, R., Rapp, G., Winter, R. & Royer, C. A. (1999). Exploring the temperature-pressure phase diagram of staphylococcal nuclease. *Biochemistry* **38**, 4157–4164.

Parisi, G. (2000). The physics of the glass transition. *Physica* (*A*) **280**, 115–124.

Pechukas, P. (1981). Transition-state theory. *Annu. Rev. phys. Chem.* **32**, 159–177.

Percus, J. K. (1982). Non-uniform fluids. In *The Liquid State of Matter: Fluids, Simple and Complex* (eds. E. Montroll & J. Lebowitz). Amsterdam: North-Holland.

Plaxco, K. W., Simons, K. T. & Baker, D. (1998). Contact order, transition state placement and the refolding rates of single domain proteins. *J. molec. Biol.* **277**, 985–994.

Plaxco, K. W., Simons, K. T., Ruczinski, I. & Baker, D. (2000). Topology, stability, sequence, and length: defining the determinants of two-state protein folding kinetics. *Biochemistry* **39**, 11177–11183.

Plotkin, S. S. & Onuchic, J. N. (2000). Investigation of routes and funnels in protein folding by free energy functional methods. *Proc. natn. Acad. Sci. USA* **97**, 6509–6514.

Plotkin, S. S. & Onuchic, J. N. (2002). Structural and energetic heterogeneity in protein folding. I. Theory. *J. chem. Phys.* **116**, 5263–5283

Plotkin, S. S., Wang, J. & Wolynes, P. G. (1996). Correlated energy landscape model for finite, random heteropolymers. *Phys. Rev.* (*E*) **53**, 6271–6296.

Plotkin, S. S., Wang, J. & Wolynes, P. G. (1997). Statistical mechanics of a correlated energy landscape model for protein folding funnels. *J. chem. Phys.* **106**, 2932–2948.

Plotkin, S. S. & Wolynes, P. G. (1998). Non-markovian configurational diffusion and reaction coordinates for protein folding. *Phys. Rev. Lett.* **80**, 5015–5018.

Poland, D. & Scheraga, H. A. (1970). *Theory of Helix–Coil transitions in Biopolymers*. New York: Academic Press.

Pollak, E. (1991). Variational transition-state theory for a dissipative cubic oscillator. *J. phys. Chem.* **95**, 10235–10240.

Pollak, E. (1992). Variational transition state theory for dissipative systems. In *Activated Barrier Crossing* (eds. P. Hanggi & G. Fleming), pp. 5–41. Singapore: World Scientific.

Pollak, E., Tucker, S. & Berne, B. J. (1990). Variational transition-state theory for reaction rates in dissipative systems. *Phys. Rev. Lett.* **65**, 1399–1402.

Prince, R. B., Saven, J. G., Wolynes, P. G. & Moore, J. S. (1999). Cooperative conformational transitions in phenylene ethynylene oligomers: chain-length dependence. *J. Am. Chem. Soc.* **121**, 3114–3121.

Radford, S. A., Dobson, C. M. & Evans, P. A. (1992). The folding of hen lysozyme involves partially structured intermediates and multiple pathways. *Nature* **358**, 302–307.

Reiss, H., Katz, J. L. & Cohen, E. R. (1967). Translation-rotation paradox in the theory of nucleation. *J. chem. Phys.* **48**, 5553–5560.

Riddle, D. S., Grantcharova, V. P., Santiago, J. V., Alm, E., Ruczinski, I. & Baker, D. (1999). Experiment and theory high-light role of native state topology in sh3 folding. *Nat. Struct. Biol.* **11**, 1016–1024.

Rips, I. (1998). Nonadiabatic reactions in condensed phase in the absence of thermal equilibrium. *Chem. Phys.* **235**, 243–255.

Sadqi, M., Casares, S., Abril, M. A., Lopez-Mayorga, O., Conejero-Lara, F. & Freire, E. (1999). The native state conformational ensemble of the sh3 domain from alpha-spectrin. *Biochemistry* **38**, 8899–8906.

Saven, J. G., Wang, J. & Wolynes, P. G. (1994). Kinetics of protein folding: the dynamics of globally connected rough energy landscapes with biases. *J. chem. Phys.* **101**, 11037–11043.

Sfatos, C. D., Gutin, A. M. & Shakhnovich, E. I. (1994). Phase transitions in a 'many-letter' random heteropolymer. *Phys. Rev.* (*E*) **50**, 2898–2905.

Shakhnovich, E. I. & Gutin, A. M. (1989a). Formation of unique structure in polypeptide chains: theoretical investigation with the aid of a replica approach. *Biophys. Chem.* **34**, 187–199.

Shakhnovich, E. I. & Gutin, A. M. (1989b). The nonergodic ('spin-glass-like') phase of heteropolymer with quenched disordered sequence of links. *EuroPhys. Lett.* **8**, 327–332.

Shakhnovich, E. I. & Gutin, A. M. (1989c). Relaxation to equilibrium in the radom energy model. *EuroPhys. Lett.* **9**, 569.

Shakhnovich, E. I. & Gutin, A. M. (1993). Engineering of stable and fast-folding sequences of model proteins. *Proc. natn. Acad. Sci. USA* **90**, 7195–7199.

Shea, J. E., Onuchic, J. N. & Brooks, C. L. (1999). Exploring the origins of topological frustration: design of a minimally frustrated model of fragment b of protein a. *Proc. natn. Acad. Sci. USA* **96**, 12512–12517.

Sheinerman, F. B. & Brooks, C. L. (1998). Molecular picture of folding of a small α/β protein. *Proc. natn. Acad. Sci. USA* **95**, 1562–1567.

Sherrington, D. & Kirkpatrick, S. (1975). Solvable model of a spin glass. *Phys. Rev. Lett.* **35**, 1792–1796.

Shlesinger, M. G. & Montroll, E. (1984). On the williams-watts function of dielectric relaxation. *Proc. natn. Acad. Sci. USA* **81**, 1280–1283.

Shoemaker, B. A., Wang, J. & Wolynes, P. G. (1997). Structural correlations in protein folding funnels. *Proc. natn. Acad. Sci. USA* **94**, 777–782.

Shoemaker, B. A., Wang, J. & Wolynes, P. G. (1999). Exploring structures in protein folding funnels with free energy functinals: the transition state ensemble. *J. molec. Biol.* **287**, 675–694.

Shoemaker, B. A. & Wolynes, P. G. (1999). Exploring structures in protein folding funnels with free energy functinals: the denatured ensemble. *J. molec. Biol.* **287**, 657–674.

Silberberg, A. (1962). The adsorption of flesible macromolecules. part i. the isolated macromolecule at the plane interface. *J. phys. Chem.* **66**, 1872–1883.

Socci, N. D., Onuchic, J. N. & Wolynes, P. G. (1996). Diffusive dynamics of the reaction coordinate for protein folding funnels. *J. chem. Phys.* **104**, 5860–5868.

Socci, N. D., Onuchic, J. N. & Wolynes, P. G. (1998). Protein folding mechanisms and the multidimensional folding funnel. *Proteins: Struct. Funct. Genet.* **32**, 136–158.

Sorenson, J. M. & Head-Gordon, T. (1998). The importance of hydration for the kinetics and thermodynamics of protein folding: simplified lattice models. *Folding and Design* **3**, 523–534.

Szabo, A., Schulten, K. & Schulten, Z. (1980). First passage time approach to diffusion controlled reactions. *J. chem. Phys.* **72**, 4350–4357.

Takada, S., Luthey-Schulten, Z. & Wolynes, P. G. (1999). Folding dynamics with non-additive forces: a simulation study of a designed helical protein and a random heteropolymer. *J. chem. Phys.* **110**, 11616–11629.

Taverna, D. M. & Goldstein, R. A. (2000). The distribution of structures in evolving protein populations. *Biopolymers* **53**, 1–8.

Thirumalai, D. (1995). From minimal models to real proteins: scaling laws for three stage multipathway mechanism for protein folding. *J. Phys. I France* **5**, 1457–1467.

Ueda, Y., Taketomi, H. & Gō, N. (1975). Studies on protein folding, unfolding, and fluctuations by computer simulation. *Int. J. Peptide Res.* **7**, 445–459.

Unger, C. & Klein, W. (1984). Nucleation theory near the classical spinodal. *Phys. Rev.* (*B*) **29**, 2698–2708.

Viguera, A. R., Villegas, V., Aviles, F. X. & Serrano, L. (1996). Favourable native-like helical local interactions can accelerate protein folding. *Folding and Design* **2**, 23–33.

Wang, J., Plotkin, S. S. & Wolynes, P. G. (1997). Configurational diffusion on a locally connected correlated energy landscape: application to finite, random heteropolymers. *J. Phys. I France* **7**, 395–421.

Wang, J., Saven, J. G. & Wolynes, P. G. (1996). Kinetics in a globally connected, correlated random energy model. *J. chem. Phys.* **105**, 11276–11284.

Zwanzig, R. (1973). Nonlinear generalized langevin equations. *J. Stat. Phys.* **9**, 215.